University of Wollongong

Research Online

2019

Renewable energy and energy storage based hybrid remote area power supply systems

Md Nafiz Musarrat
University of Wollongong

Follow this and additional works at: https://ro.uow.edu.au/theses1

Recommended Citation

RENEWABLE ENERGY AND ENERGY STORAGE BASED HYBRID REMOTE AREA POWER SUPPLY SYSTEMS

A Thesis Submitted in Partial Fulfilment of the Requirements for the Award of the Degree

Master of Philosophy

from

University of Wollongong

by

Md Nafiz Musarrat, B.Sc. (Eng)

School of Electrical, Computer, and Telecommunications Engineering
Faculty of Engineering and Information Sciences
University of Wollongong Australia

March, 2019

Declaration of Authorship

I, Md Nafiz Musarrat, hereby declare that this thesis, submitted in partial fulfilment of the requirements for the award of Master of Philosophy in the University of Wollongong, is entirely my own original work except where clearly acknowledged. I certify that this thesis contains no material that has been or will be submitted for the award of any degree in my name in any other university.

Md Nafiz Musarrat

08 March, 2019

Declaration of Publications

This thesis includes chapters that have been written as the following articles:

Chapter 2

M. N. Musarrat, M. R. Islam, K. M. Muttaqi, and D. Sutanto, "Operation of Renewable Energy and Energy Storage based Hybrid Remote-area Power Supply Systems: Challenges, State-of-the-arts and Case Studies," under preparation for submission to *Renewable and Sustainable Energy Reviews*.

Chapter 3

M. N. Musarrat, M. R. Islam, K. M. Muttaqi, and D. Sutanto, "Enhanced frequency support from a PMSG-based wind energy conversion system integrated with a high temperature SMES in standalone power supply systems," *IEEE Transactions on Applied Superconductivity*, vol. 29, no. 2, p. 3800206, Mar. 2019.

M. N. Musarrat, M. R. Islam, K. M. Muttaqi, D. Suttanto, "Suboptimal power point tracking for frequency response of PMSG based wind turbines in remote area power supply systems," In: Proceedings of the *2018 IEEE International Conference on Applied Superconductivity and Electromagnetic Devices (ASEMD)*, 15–18 April, 2018, Tianjin, China, DOI: 10.1109/ASEMD.2018.8559597, Available in IEEE Xplore, IEEE USA.

Chapter 4

M. N. Musarrat, M. R. Islam, K. M. Muttaqi, D. Suttanto, "Minimization of thermal stress on the rotor side converter of DFIG while operating around synchronous speed," *IEEE Power Electronics, Drives and Energy Systems Conference (PEDES)*, 18–21 Dec., 2018, Chennai, Tamilnadu, India, will be available in IEEE Xplore, IEEE USA.

M. N. Musarrat, M. R. Islam, K. M. Muttaqi, D. Suttanto, M. Ashib Rahman "Improving the Thermal Performance of Rotor-side Converter of Doubly-fed Induction Generator Wind Turbine while Operating around Synchronous Speed," under preparation for submission to *IEEE Transactions on Industry Application*.

Chapter 5

M. N. Musarrat, M. R. Islam, K. M. Muttaqi, and D. Sutanto, "Shunt Active dc Filter to Reduce the dc-Link Ripple Current Caused by Power Converters to Improve the Lifetime of Aluminium Electrolytic Capacitor," submitted to *IEEE Transactions on Power Delivery*.

Acknowledgements

I would like to express my sincere gratitude to my supervisor panel: Prof. Kashem Muttaqi, Dr. Md. Rabiul Islam, and Prof. Danny Sutanto who provided guidance and support throughout my journey towards achieving Master of Philosophy degree in Electrical Power Engineering. I am also grateful to all the staff of Australian Power Quality and Reliability Centre (APQRC) for helping me in the laboratory. Last but not least, nothing would be possible without the support from my loving parents.

Abstract

Remote Area Power Supply (RAPS) systems can play an effective role to supply electric power to the rural and remote communities, since these areas are usually far from the central utility grid. RAPS systems are usually powered by non-renewable sources. Due to growing environmental concern as well as improving infrastructures, renewable sources have become more economic. However, renewable resources are intermittent in nature, and can therefore cause reliability concern in the RAPS system. It imperative to consider ways to increase the reliability of the RAPS system powered by the renewable sources. This research aims to propose innovative strategies to improve the reliability of RAPS systems and to meet up the challenges that come with the higher level of renewable energy penetration.

The contribution of this thesis is to improve the reliability of RAPS system with focus on two aspects: improving dynamic stability with support from wind energy conversion system (WECS) and maintenance of WECS components.

In regard to improving dynamic stability, a strategy has been proposed to extract support from wind generators for frequency regulation. Usually, the frequency regulation is solely supported by the conventional generators, as they have natural inertia and a governor to adjust the generation to match the power demand. In a RAPS system without the conventional generators, the strategy enables the permanent magnet synchronous generator (PMSG) based wind turbines to support the frequency regulation through artificial inertia. A suboptimal power point tracking strategy has been proposed to store the energy, which will be released upon the command from inertia controller when there is a sudden dip in system frequency. The proposed frequency regulation strategy incorporates the superconducting magnetic energy storage (SMES) system with the wind energy conversion system (WECS) to enhance its frequency response capability. The detailed charging and discharging algorithms for the SMES have been developed as well. Since, the SMES has very limited energy storage, it is used to regulate only frequency with a high rate of change and it has been achieved by using a high pass filter with appropriate time constant.

In regard to system reliability, the impact of the low slip operation on the rotor side converter lifetime in a doubly-fed-induction-generator (DFIG) and the thermal stress on an electrolytic capacitor in the converter due to the high ripple current have been explored.

The rotor side converter of a DFIG is subjected to this high thermal cycle when the machine operates near synchronous speed or in a low slip region. The high thermal cycling reduces the lifetime of the power electronic converters exponentially. A thermal network has been developed to measure the converter losses and the semiconductor junction temperatures. Temperature measurements of diodes and semiconductor junctions have been performed and the total power losses have been quantified. A comprehensive algorithm has been proposed incorporating both the switching frequency reduction and the current derating technique to reduce the thermal cycling of the rotor side converter in a DFIG. Appropriate reference points and thresholds have been selected to ensure the consistency of the machine's performance. Another vulnerable component of a power electronic converter based system is the aluminum electrolytic capacitor. The capacitor becomes subject to high thermal stress if the ripple current is high, which can result in the vaporization and diffusion of aluminium electrolytic liquid. Consequently, the 'wet' aluminium capacitor will be dried out. Therefore, continuous operation in high temperature can cause early failure of the capacitor. A comprehensive analysis of the mechanism that can lead to the capacitor stress has been carried out. A dc shunt active filter has been proposed to minimize the capacitor ripple current so that the life expectancy of an electrolytic capacitor remains unharmed. A detailed design principle has been carried and the necessary operating condition has been suggested to offer the maximum efficient and economic operation. The verification of the proposed topologies has been performed for different case scenarios. In-depth simulations have been carried out for a detailed RAPS system model, to verify the proposed strategies. The simulations results affirm the efficacy of the proposed control algorithms.

This thesis has developed concrete contributions towards establishing a renewable energy and energy storage based hybrid RAPS with higher reliability. The innovations demonstrated in this thesis will facilitate the acceptance of renewable sources in the mainstream generations while providing financial and environmental advantages to the rural and remote communities.

Table of Contents

List of Figures

List of Tables

Chapter 1

Introduction

1.1. Motivation

Remote area power supply (RAPS) system is an effective way to supply electric power to remote communities. A significant amount of the world population is outside the access of utility grid and RAPS system is a convenient solution to this. It is even promoted rigorously by different aid organizations. A RAPS system is usually diesel generator/engine (DE) based. The diesel generator based RAPS systems are very robust and the reliability is very high. However, with the increasing concern for environment, renewable energy options have drawn much attention. It seems unwise not to utilize renewable sources since one of the promising benefits of a remote area is abundant accommodation for renewable energy resources. Furthermore, fuel transfer to a remote area alone is extremely costly. Therefore, there is a great need to switch to renewables for the RAPS system. It is more economic to utilize the local renewable resources than importing costly conventional fuel.

Electricity generation is one of the largest sources of carbon emission. Global warming and the carbon emission have been accelerating in an alarming rate which calls for the need of reducing fossil fuels, which are still the main sources of energy. Underdeveloped countries are explicitly dependent on fossil fuels due to the lack of available infrastructure. Fig. 1.1 illustrates the total energy consumption worldwide from different energy sources.

Due to the serious environmental impact, renewable energy has drawn the attention of the world leaders and it has been recognized that the renewable energy source can offer effective solution to this serious challenge. Fig. 1.1 shows that renewable sources are still showing a significant growth in recent years. In the last few decades, the wind energy has

increased rapidly and become the second most popular form of renewable energy next to solar energy [2].
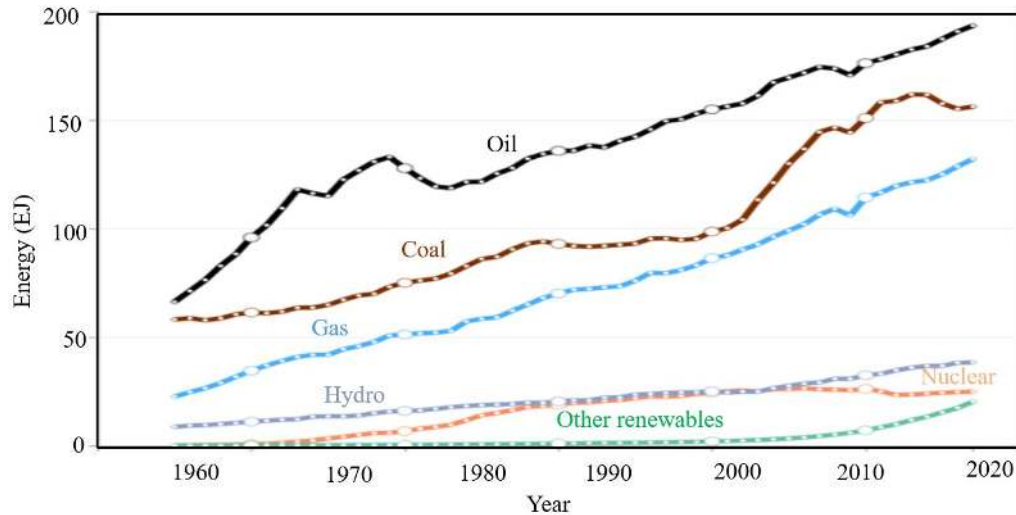
Fig. 1.1. Worldwide energy consumption from different energy sources [1]

In Australia, wind energy is a becoming one of the most significant energy resources; in particular, the Australia Energy Research Agency (ARENA) is playing a leading role in the growth of wind energy in Australia. The Kennedy Energy Park is a hybrid renewable energy facility situated in Hughenden in North Queensland developed in a partnership between Windlab and Eurus. This project will consist of 15MW solar photovoltaic (PV), 43.2MW wind and a 2MW/4MWh lithium ion battery storage facility and supply reliable renewable energy to the local community. It will test the technologies in combination to see if the plant can provide dispatchable power over a 24 hour period. Partnering battery storage with wind and solar energy generation in a single location allows renewable energy to be stored for use at peak usage times and when needed most. With solar producing during the day, wind mainly at night, and the battery available to smooth out any variability, the plant will provide more continuous energy generation.

The Rottnest Island, Western Australia's 5 GWh power demand is currently provided by five conventional diesel engines, two low-load diesel engines and a single 600 kW wind turbine. A large amount of energy is needed to run the desalination plant that produces fresh water for the island. The project will introduce 600 kW of solar energy into the existing power

system to boost and diversify the renewable energy capacity in the system. Hydro Tasmania will deploy an advanced control system, along with a dynamically controlled resistor, to maximize the contribution of renewable energy. The control system will be integrated with the desalination plant and water storage facility to switch on the plant and pumps when renewable generation outpaces demand on the island. The combined contribution of wind and solar generation, working with smart demand-management of the desalination plant, is expected to reduce diesel fuel used for power generation by 45%. This will reduce Rottnest Island's reliance on shipped in diesel, potentially providing cheaper and more reliable power.

So far, Hydro Tasmania has showcased some extraordinary results in the Bass Strait with increased renewable energy penetration. In the King Island project, they have been able to effectively lower down the fossil fuel usage by 45%, largely from the energy converted from the wind turbines. Currently, the wind turbines support the 70% of the energy demand in the island resulting in reduced fuel consumption from around 4.5 million liters to 2.6 million liters per annum.

However, intermittency is an inherent nature of the renewable sources. Control mechanism is required to ensure the efficient operation of the renewable generation systems. The controls in the renewables are usually optimized to extract the maximum power from the renewable sources (wind, solar, etc.). For example, both PV and wind energy conversion system (WECS) are operated by maximum power point tracking. Therefore, these techniques do not facilitate the network event ride through capability. The renewable sources are interfaced with network through power electronic converter. Hence, the system dynamics do not affect their controllability [15].

The grid connected renewable sources have different operation strategy since any large utility grid is very stringent in maintaining the fundamental parameters. But, RAPS system is a small network and it is non-stringent. All the generators are primary power suppliers and failure of any of them will cause generation demand mismatch. To maintain the power quality, load-shedding will be needed which reduces the power system reliability. In a conventional generator, the power generation can be adjusted according to the demand by injecting more fossil fuels. But, for renewable sources, it is not possible to adjust the

generation according to the demand. The maximum available renewable energy is fixed in any area with a given conversion system at its highest efficiency. The current environmental concern calls for increasing the level of renewable energy penetration. But, with the higher renewable penetration, the system reliability may be affected.

Unlike large utility grid, there will be no advanced protection devices or control system. The grid code is not maintained strictly in a RAPS system. Rather, a RAPS system is expected to incorporate cost-effective and efficient protection and control system. The main target of a RAPS system is the end-user satisfaction. Since, the high penetration of renewables produces unpredictable power generation; it also increases the probability of unplanned tripping and power outage. Also, the reliability measurement in a large grid is much rigorous and complex. On the other hand, in a RAPS system, the customer satisfaction and meetings some primary standards are the main priorities.

The renewable energy systems consist of several components that can be vulnerable if they are used for long time. It is also responsible for the reduced RAPS system reliability since failure of one system can lead to the whole system failure. There are the drive trains, power electronic converters, capacitors etc. that can often malfunction. It is imperative that the lifetime of this components are ensured. There should be a comprehensive analysis on these stress mechanism. Also, effective strategies should be proposed to solve any stress problem.

Therefore, the motivation behind this thesis is the rectification of the above mentioned issues by proposing several mitigation strategies that will allow the increase of the renewable energy penetration level in the RAPS system for isolated areas.

1.2. Research Goals

In this research project, the main aims are to develop: (1) control strategies for wind energy based power plant under small and large disturbance events and different loading condition in remote area based power supply (RAPS) systems, which are powered by distributed generation units; (2) models of the RAPS system that can analyze the stress on the different components of renewable generation systems and propose necessary mitigation techniques.

First, the frequency response support from WECS is investigated during frequency dip in a network. Unlike in the large grid, the load fluctuation in a RAPS system is very high and frequent. Conventional generator can support frequency regulation by adjusting the fuel inputs. But, the overall system frequency response is not up to the grid code. Renewable sources such as, wind turbines cannot automatically participate in frequency regulation since they are isolated from the system dynamics through power converters. However, in this thesis, control strategies are proposed to improve the frequency response capability of a permanent-magnet-synchronous-generator (PMSG) based WECS so that the overall system frequency regulation is improved. The impact of having additional power supply from SMES, super capacitor and their performance during frequency event are examined. Means of incorporating different converter control strategy, their feasibility and comparison with external sources are explored as well.

Second, the power electronics converter used in doubly-fed-induction-generator (DFIG) based wind turbines are prone to high thermal cycle and power loss due to fluctuations in rotor speed, due to frequent operation around synchronous speed. The junction temperature and power loss of insulated gate bipolar transistors (IGBT) and diodes, when the wind turbines are operated near synchronous speed, are quantified and analyzed. Also, control strategies are developed to reduce the loss significantly or avoid the operation around the speed. The developed models are used in a RAPS network to simulate the response under different types of loading, small disturbances (capacitor switching, light load switching, load rejection etc.) and large disturbances (islanding, single line to ground fault, symmetrical fault etc.).

Third, the switching in the power electronic devices in the renewable energy generation units can cause a high ripple in the dc-link capacitor current resulting in a high core thermal loss and eventually lead to failure due to electrolytic liquid loss in a 'wet' aluminum electrolytic capacitor. A comprehensive analysis on the capacitor stress has been carried out using different case scenarios. Also, a strategy is proposed to mitigate the core loss problem.

To verify the performance of the developed strategies and models, simulations are performed in MATLAB/Simulink environment. MATLAB is used for data processing,

pattern recognition and parameter tuning. Fig. 1.2 shows the flow chart of the thesis objectives and contributions.
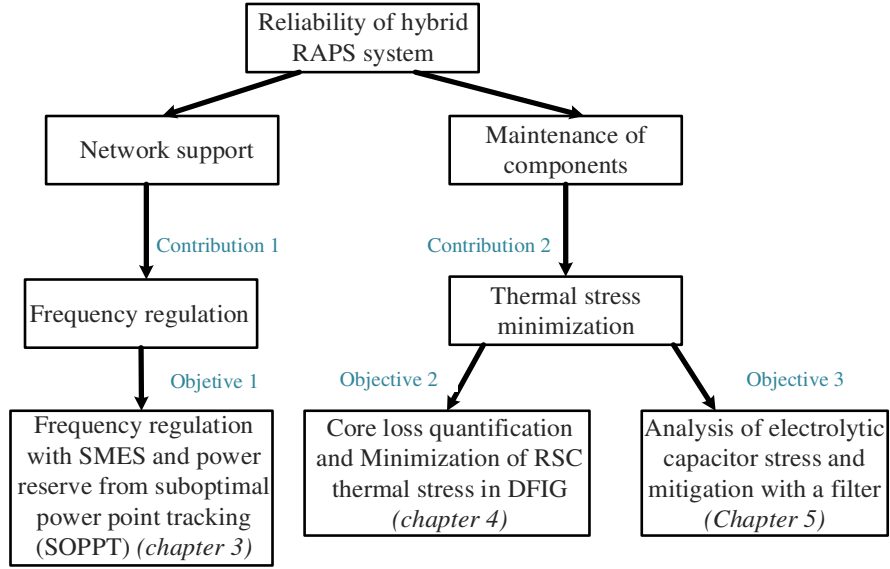
Fig. 1.2. Thesis objectives and contributions

1.3. Thesis Outline

The rest of the thesis is outlined as below.

Chapter 2: This chapter provides a detailed and critical literature review. The review is mainly focused on the available research works on the wind energy conversion system based control and reliability maintenance. Also, associated technical challenges are identified in this chapter.

Chapter 3: This chapter investigates the frequency regulation capability of a PMSG based wind turbine. The prospect of using an artificial inertia control for frequency regulation is studied. A power reserve through suboptimal power point tracking is proposed for efficient frequency response. A frequency response strategy is proposed using an SMES. The proposed topology does not require additional inverter. Also, a comparative study has been

carried out to compare the frequency regulation with artificial inertia, super capacitor and SMES.

Chapter 4: This chapter describes an investigation is performed on the semiconductor thermal stress when a DFIG operates near synchronous speed. The thermal loss and junction temperatures are quantified for each half bridge of the rotor side converter. A switching control technique and a current derating technique are proposed to reduce the thermal loss during low slip operation. A coordinated control algorithm is proposed between the above mentioned techniques so that the thermal stress is minimized without compromising the system performance.

Chapter 5: This chapter describes a comprehensive stress analysis of the electrolytic capacitor due to ripple current. The characteristics of an electrolytic capacitor is discussed in detail. Also, a capacitor ripple harmonic spectral analysis has been carried out to investigate the effect of different slip ratio operation on the dc-link capacitor core loss of a DFIG based WECS. Furthermore, an active filter strategy is proposed to mitigate the ripple current in order to improve the capacitor life time.

Chapter 6: This chapter presents the conclusions of this thesis and some scope for future works is presented.

Chapter 2

Literature Review

2.1. Introduction

This chapter provides an overview of the wind energy based RAPS system. The system parameters, reliability of the system components, and different control strategies of a wind energy based RAPS system are reviewed in this chapter. Section 2.2 gives the current energy consumption scenario. In this section the promising demand of the renewable sources is illustrated. In Section 2.3, a brief introduction about a RAPS system and its architecture is provided. The inherent characteristics of a RAPS system that makes the control and reliability maintenance challenging are discussed in this section. In Section 2.4, there is a detailed background discussion about the widely used wind energy conversion technologies in RAPS systems with focus on DFIG and PMSG. In Section 2.5, the dynamic performance of a PMSG based wind energy conversion systems during frequency regulation is discussed. The existing knowledge and strategies to improve its dynamic performance and their limitations have been reviewed as well. Section 2.6 gives an idea about the thermal behavior of the power electronic converters in a DFIG. Diminished reliability of the power electronic converters in a specific scenario is discussed. In Section 2.7, there is a discussion about the thermal stress on the dc-link electrolytic capacitor. The mechanism of electrolytic capacitor loss is also reviewed along with the existing strategies to reduce the thermal loss. In Section 2.8, there is a background discussion about an algorithm to improve the computational efficiency while analyzing huge number of data from RAPS system network information center.

2.2. Overview of RAPS Systems

Although, the integration of renewable energy sources with the large grid is a popular topic of research, the rural and remote areas which are deprived of the central utility grid are often dependent on the renewable sources. Instead of the large utility grid, the electrical power to the remote communities is usually supplied through remote area power supply (RAPS) system. A RAPS system can be defined as a small electricity network that serves a group of households [8] A RAPS system is never connected to the utility grid, which means it never absorbs from or injects power to the grid. It is becoming increasing popular as a feasible solution for the rural areas to get access to electric power. The RAPS can be a single energy resource based, energy storage based or a hybrid system. A diesel generator-based RAPS system is more reliable; however, the operating cost is very high. A renewable energy-based RAPS system is economically good, but the system can become more unreliable. Also, the load fluctuation in a standalone system is really high. The RAPS systems are supposed to supply power without any interruption to the consumer-end efficiently. In a large utility grid, the level of renewable energy penetration is usually limited. But, in a RAPS system, the system can be as high as hundred percent renewable-based. With the higher penetration of renewable energy, the system resilience will be lower due to intermittency nature of the renewable sources. Also, the load is highly fluctuating in a small network. Since, there are energy sources of different characteristics, the coordination of them can be quite challenging. Non-linear loads are most likely to occupy a large portion of the total load, which can compromise the power quality significantly. Renewable sources do not have inherent inertia, and therefore, they do not have any resilience in case of any emergency event. The RAPS system can be of a common ac-bus, a common dc-bus or a hybrid-bus system. However, this thesis will be based on a common ac-bus hybrid RAPS system, where both diesel generator and renewable sources are present. In a common ac-bus RAPS system, both the dc and ac type sources are connected to the ac-bus. In order to achieve this, the inverters will need to be interfaced with the dc sources. The ac-loads will directly absorb the electrical power from the ac-bus and dc-loads will absorb power from the ac-bus through power converters. If there are energy storage systems in the RAPS, they can be utilized to balance the difference

between the demand and the generation using a bidirectional power conditioning system. Fig. 2.1 shows a basic block diagram of an ac bus hybrid RAPS system
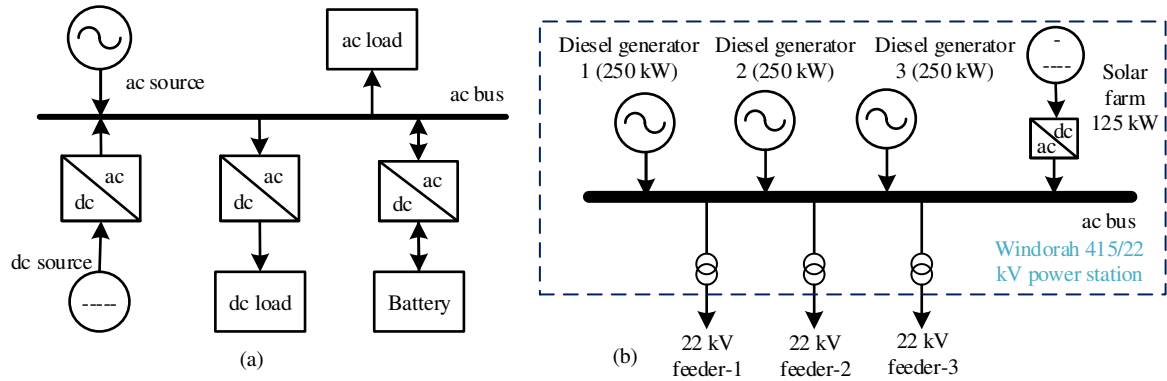
Fig. 2.1. Basic block diagram of an ac bus hybrid RAPS system: (a) an hypothetical RAPS system [8]; (b) Windorah RAPS system from Energy Queensland (Ergon Energy) [102].

2.3. Wind Energy Conversion Systems (WECS) in RAPS Systems

A brief background on the wind energy conversion system (WECS) is discussed in this section. The wind energy conversion system converts the wind energy to electrical energy. The WECS are becoming more sophisticated with the evolution of the power electronics. A wind energy conversion system consists of a wind turbine, an alternator and a power conditioning system. A WECS can be based on a fixed speed or a variable speed turbine operation.

2.3.1. A fixed speed WECS

In this system, the turbine rotates at a constant angular velocity by means of gears. A squirrel cage induction generator (SCIG) is connected to the supply grid through a power conditioning system and a transformer [3]. This system always consumes reactive power. An appropriate compensation arrangement needs to be made. Due to the design simplicity, the robust control and the low cost, the fixed speed WECS have become very popular in the developing countries.

However, a fixed speed system is not suitable in a highly fluctuating wind condition. The fluctuating wind speed will cause huge stress on the gears. During high gust, there is a probability of a total breakdown in the drive train. Fig. 2.3 shows a fixed speed WECS

configuration, showing the wind turbine, the gear box to maintain the output to have a constant angular velocity, the squirrel cage induction motor (SCIG), the ac/ac converter as the power conditioning system, the capacitor bank to provide the required reactive power and a transformer to raise the voltage to the required voltage level to supply power to the ac bus.
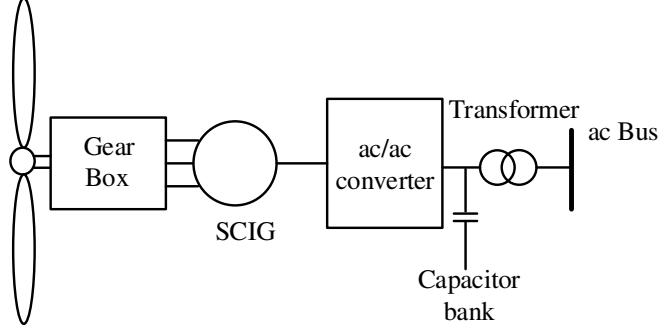
Fig. 2.2. Fixed speed WECS configuration [3]

The mechanical output power is determined by,

$$P_{wind} = \frac{1}{2} \; A v^3 C_p (\; , \;)$$

(2.1)

$$= \frac{_r R}{v}$$

(2.2)

Where, ρ is the air density, A is the wind swept area, υ is the wind speed and ω_r is the rotor speed. $C_p(\lambda, \beta)$ is the power coefficient of the WECS. It is a function of tip speed ratio λ and pitch angle β. A typical curve of Cp with respect to tip-speed ratio, λ with the pitch angle held constant is shown in Fig. 2.3.

For, fixed speed wind turbine, λ cannot be kept at the optimum value to achieve the maximum power coefficient, C_{pmax} with the change in wind velocity since, rotor speed cannot be controlled in a fixed speed wind turbine. Therefore, the efficiency of a fixed-speed wind turbine is constrained by wind velocity.
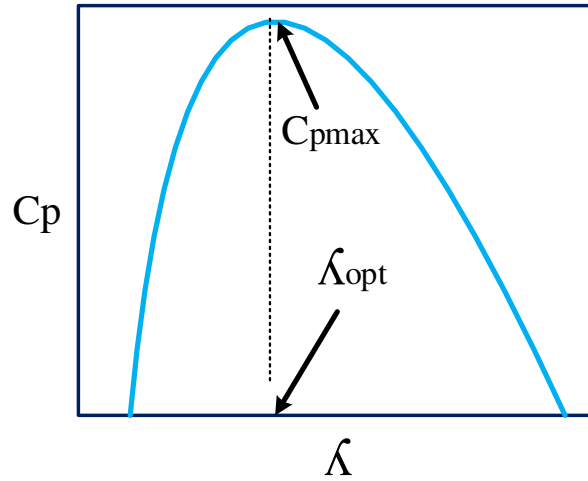
Fig. 2.3. Cp vs TSR curve.

2.3.2 A variable speed WECS

In this system, the wind turbine rotates in a variable angular velocity depending on the available wind velocity. The frequency of the output voltage is dependent on the turbine speed. Therefore, the power conditioning system is responsible to ensure a fixed system frequency despite fluctuating wind condition. However, the variable speed wind turbine is more efficient than the fixed speed wind turbine since it can capture the maximum power by adjusting its rotor speed with the variable wind velocity. Therefore, the power coefficient can be maintained at its maximum value, Cp. The control system is relatively more complex, and the cost is higher in a variable speed wind turbine in comparison to the fixed speed system.

A variable speed WECS can generally be of two types: a fully rated converter based or a partially rated converter based.

2.3.2.1. Fully rated power converter-based WECS

This system comprises a variable speed wind turbine, and an induction/synchronous generator which is connected to the utility grid through a power electronic converter system and a step-up transformer. The full power is transmitted through the power electronic converters. It is often referred to as a fully rated converter-based system.

The power electronic converter system gives the WECS the capability to adapt the output frequency to the fluctuating wind speed. It also provides a wide range of controllability which makes it a very popular solution in offshore wind turbines. The configuration in this system can either be with gearbox or gearless as the system can be designed with multiple poles. The permanent magnet synchronous generator (PMSG) based wind energy conversion system is the most popular WECS in fully rated converter-based configuration [4]. Fig. 2.4 shows a variable speed fully rated converter based WECS configuration, showing the wind turbine, an induction generator, a converter, and a transformer.
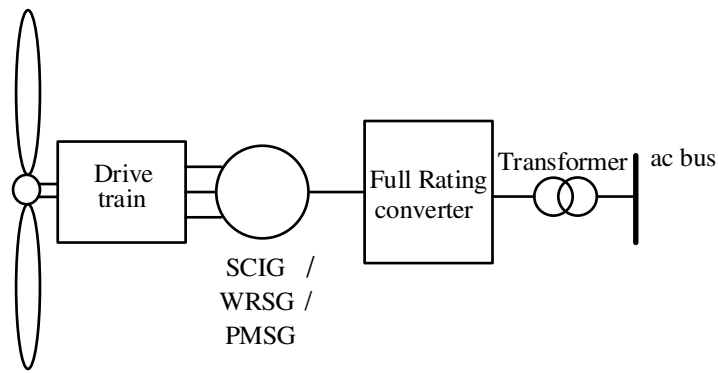
Fig. 2.4. Variable speed fully rated converter based WECS configuration [4]

2.3.2.2. A partially rated converter-based WECS

In this configuration, a variable speed wind turbine with a doubly-fed-induction-generator is used. In this system, the converter is partially rated, because only about 25~30% of the rated power is handled by the power converters. The stator is directly connected to the grid. There are two converters. The grid side converter controls the dc-link voltage and reactive power support. The rotor side converter controls the excitation of the rotor coil and the rotor reactive power support as well. The decoupled control is possible in this configuration, which makes the WECS capable to control the active and reactive power separately [5]. From the operational point of view, a partially rated converter based WECS are quite complex. The control system can be utilized for smooth grid connection. Fig. 2.5 shows a simplified topology of the DFIG based WECS, showing a turbine, drive train, doubly fed induction generator, and a back-to-back converter.
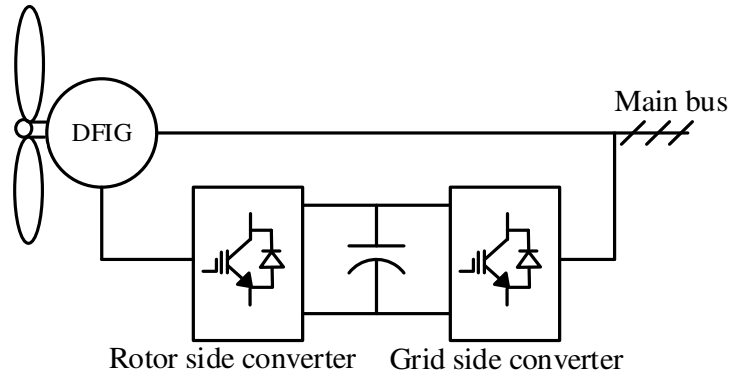
Fig. 2.5. Partially rated converter based WECS configuration [5].

2.3.3. Generators used in WECS

There are two types of generators that are the most popular to be used for the WECS systems: the permanent magnet synchronous generator (PMSG) and the doubly-fed-induction-generator (DFIG).

2.3.3.1 Permanent Magnet Synchronous Generator (PMSG)

Large power companies, like GE (General Electric) Energy, Siemens, Vestas, employ the PMSG-based WECS systems. Usually, the PMSGs used in the wind turbines are salient pole PMSGs. Also, the systems are direct-drive [6]. In the PMSG based WECS system, the efficiency is higher than in the SCIG based WECS system, since it does not need any external excitation. However, the permanent magnet is costly. Besides, the system comprises of full rated power converters which increases the total operation and maintenance cost. The operating temperature of the system is another important concern for the PMSG. The operating temperature must be below the Curie point or the magnetic property will disappear [6].

2.3.2.1. Doubly-fed-induction-generator (DFIG)

The main idea of the DFIG is that the rotor windings are connected to the grid through the slip rings and a converter. Due to the slip ratio, the rotor frequency can vary with the grid frequency. By controlling the converters, it is possible to control the active and reactive

power support from the grid. If the machine rotates faster than the synchronous speed, then the machine is operating in the super-synchronous mode, otherwise the machine will operate at the sub-synchronous mode, if the rotational speed is lower than the synchronous speed [7]. However, in both cases, the DFIG supplies power to the grid. In sub-synchronous mode, the rotor coil consumes electrical power for excitation and the stator supplies power. But, in the super-synchronous mode, both the rotor and stator supplies power to the grid. The DFIG can be controlled using the decoupled dq-axis or using the direct torque control method. It is typically a wound rotor induction machine with the rotor excitation controllability. Apart from the excitation current control, the power electronic converters enable the machine to support the system robustness during network events.

2.4. Dynamic Behavior of RAPS System with Renewable Energy Sources during Frequency Excursion.

In a renewable energy-based RAPS system, it is imperative that the system resilience is ensured. This thesis is focused on the wind turbine-based RAPS systems. Unlike a large grid system, the renewable energy-based RAPS system inherently is not as robust. Also, the intermittent nature of the renewable sources makes the RAPS system more unreliable.

Power system events can occur for various reasons such as the load rejection, load changes, motor starting, fault etc. However, this thesis will focus on the impact of the high rate-of-change-of-frequency (ROCOF) as well as the voltage fluctuation in the dc-link. The sources and the causes of power system events must be known before appropriate mitigating actions are taken. A comparative analysis between two types of distributed generators (DG): (i) diesel generators and (ii) wind turbines has been examined under the steady state and transient operation. Usually, a rapid load variation in a RAPS system causes a high rate-of-change-of-frequency (RoCoF) and causes the system to shut-down [8]. Besides load variations, high wind fluctuations too can cause the frequency event. According to Australia Energy Market Operator (AEMO)-Power System Frequency and Time Deviation Monitoring Report, the NEM mainland (islanded system) standard operating frequency should be limited to 49 Hz to 51 Hz during load event and the RoCoF limit of 0.5 Hz/s would give low-inertia systems like RAPS a reasonable time to recover. Although in a large grid system, the system

frequency does not change much; in a RAPS system, this is a very common cause of system failure. The conventional generators generally have natural inertia and the governors also adjusts the power outputs with respect to the power demands to regulate the system frequency. But the variable speed WECS are isolated from the grid and although the DFIG based WECS has some natural inertia, it is not significant. That is why the use of an artificial inertial response had been investigated by the authors in [9]. To enhance the frequency support by utilizing the kinetic energy, a power reserve was recommended. In [10]–[13], the frequency support from the wind turbines was investigated. Since WECS are electronically controlled, they are faster in their response than those from the conventional generators, which can be exploited to support the frequency regulation. In [10], this feature has been exploited to explore the feasibility of a transient control. The proposed method in [10] utilized a fraction of the kinetic energy stored in the rotational masses to support the frequency regulation. Also, a communication with the conventional diesel generator allowed the power imbalance to be handled efficiently. But, releasing kinetic energy would shift the operating point from the MPP which would cause secondary frequency event. Also, after the operating point is shifted, it would take time to move back to the previous point.

In [14], the authors deliberately operate the turbine away from their maximum power point (MPP) for a power reserve. But a fixed reserve is unreliable, as the wind speed is unpredictable. In [14], an artificial inertial response has been used with power reserve. It can be achieved through controlling the converter current. Regardless of the mechanical torque, the required electromagnetic torque can be induced through the rotor excitation control. For a DFIG, the electromagnetic torque can be controlled through the q-axis rotor converter current.

For a permanent magnet synchronous generator-based wind turbine, the electromagnetic torque can be controlled by controlling the inductor current. However, sudden change in the torque will cause a significant torque stress on the drive train. Therefore, to improve the reliability for frequency regulation and to improve the stress on the drive train, an enhanced frequency response strategy using the ultra-capacitor for a PMSG based wind turbine has been proposed for RAPS system in [15]. In [15], the super-capacitor mitigates the transient power imbalance to support the frequency. The reserved power by the suboptimal operation

16

is utilized to charge the super-capacitor. The artificial inertia controller activates the super-capacitor to support the power imbalance. As super-capacitor can respond very fast, it improves the transient performance of the WECS significantly. However, the RoCoF is still significantly high as observed from the result presented in [15].
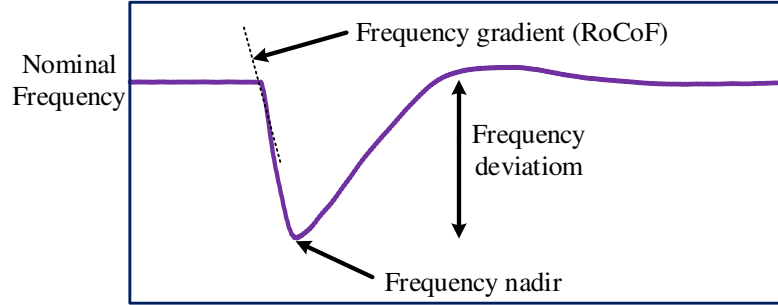
Fig. 2.6. Frequency response parameters.

Another power system event is the occurrence of fault. In case of a fault occurrence, the protection system of power crowbar is activated. The Crowbar protection of the DFIG was explained in [16], [17]. The high rotor current and high dc-link voltage are two factors that trigger the crowbar. Two functions of traditional crowbar are to bypass the converter and limit the converter in rotor windings, making the DFIG uncontrollable during fault. In [18], the authors proposed a strategy to avoid the crowbar-based protection system using a dc super-capacitor in parallel with the dc link as a temporary storage system for controlling the high dc-link voltage during any network fault. This increases the LVRT capability of the wind turbine.

2.5. Thermal Behavior of Power Electronic Converters of DFIG During Low Slip Operation

The main components of a DFIG based WECS are a turbine, a back-to-back voltage source converter (VSC) and an induction machine. The rotor side converter (RSC) enables the wind turbine for variable speed operation while maintaining the grid parameters. But the power electronics converters are prone to high junction temperature and power loss causing significant decrease in life span [36], [37].

2.5.1. Effect of the DFIG power support on the converter thermal loss

In [38], [39], the reactive power capability of a DFIG during operation around synchronous speed has been investigated. In a decoupled control method, the active and reactive power can be controlled separately. The active power can be controlled through adjusting the q-axis current and the reactive power can be controlled by adjusting the d-axis current. Therefore, the rotor current magnitude is dependent on how much support is being provided by the DFIG. It also depends on whether the machine is operating in the sub-synchronous or the super-synchronous region. With the reduced support, the rotor current magnitude will decrease, and it will result in improved thermal performance. The effect of the rotor current on the rotor side converter is because of the conduction loss, which is dependent on the current magnitude. The angular frequency of the rotor voltage and currents is determined by the slip between the angular frequency of the stator voltage and the rotor rotational speed. Therefore, the angular frequency of the rotor current becomes very small when the rotor speed approaches the synchronous speed. The lower frequency causes much longer temperature rises and falls resulting in the larger peak to peak temperature swings. The life-time of the switching devices is proportionally decreased with an increase in the amplitude of junction temperature fluctuation.

2.5.2. Effect of the switching frequency on the converter thermal loss

The converters are regulated using the pulse width modulation (PWM). The performance of the converters with different modulation techniques have also been investigated in [40]. The semiconductors in the RSC are significantly stressed around the synchronous speed. The semiconductor loss consists of two types of loss; the conduction loss and the switching loss. Between them, the switching loss is the more significant. The switching loss is dependent on the switching frequency. With a higher switching frequency, the loss will be higher causing a high temperature swing. However, if the DFIG approaches synchronous speed, despite having switching frequency unchanged, the loss will be higher. If the switching frequency is kept lower, the switching loss and the overall junction temperature fluctuation will be lower.

The converter loss will be higher with the higher thermal impedances in the interfaces. The thermal impedance is a function of the temperature, the time constant and the IGBT "on" time. Therefore, any change of these parameters will result in a change of power loss.

2.5.3. Thermal model development

Fig. 2.6 shows the flowchart for calculating the power loss and the junction temperature. The thermal network can be of Foster or Cauer type [45]. In this thesis, the Cauer thermal network will be used for the calculation. The rotor voltage, the current and the switching frequency data are fed into the loss calculation unit. The calculated junction temperature is fed back into the loss calculation function. Both switching and conduction loss are dependent on the junction temperature which is shown in (4.2) and (4.3). The dependence of the thermal loss on the junction temperature is discussed in detail in Chapter 4. However, since these losses are the function of junction temperature the immediate reading of the junction temperature needs to be fed back into the loss calculation unit. However, it does need to iterate more than once.
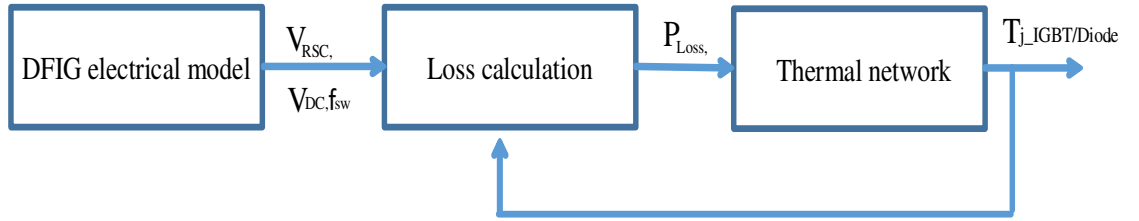
Fig. 2.7. Thermal calculation model

2.5.4. Strategies to reduce thermal losses of switching devices

In [41], [42], the authors proposed a strategy to reduce the switching frequency. As the switching loss constitutes the bigger portion of the total loss, reducing the switching frequency decreases the junction temperatures as well the temperature swings. But the resulting harmonic problem should be mitigated with improved filtering technique. The harmonic design needs to be robust since the switching frequency reduction causes a significant harmonic distortion. The harmonic distortion not only affects the grid power quality but also

causes significant speed ripple causing a stress on the gear. In [43], the rotor speed jumps above the dead band region (a small area around synchronous speed). This was caused by inducing the electromagnetic torque by controlling the converter current. However, the rapid change in the rotor speed and torque causes a severe mechanical stress on the drive train. A suboptimal power point tracking strategy is a feasible solution. In this technique, the DFIG will be operated along a fixed curve away from the dead band. But operating the machine along a fixed curve requires a significant stress on the drive train. It also requires a reliable operation of the anemometer to ensure that it moves to its maximum power point tracking after the wind velocity is large enough such as not making the rotor operate near synchronous speed.

In [44], a strategy was proposed to reduce the thermal loss. However, the only parameter that was controlled to reduce the temperature loss was the switching frequency. Reducing the switching frequency caused a significant harmonic distortion. The authors also proposed a threshold of the harmonic distortion so that the switching frequency reduction keeps the harmonic distortion limited. But in this thesis, the threshold limit was determined when the DFIG is operating at the rated speed. Also, it did not take the maximum junction temperature and the temperature fluctuation while reducing the switching frequency.

Another strategy proposed in [45] is the multimode operation of a DFIG based WECS. The idea was that if the rotor speed approached the dead band, the DFIG would be converted to a simple induction generator (IG) mode by activating the crowbar as proposed. However, this required to have the same electromagnetic torques in the two modes during the transition or there would be a huge torque transient. So, the rotor speed had to shift to an equivalent point between the two modes before the transition. But an accurate and an early prediction to determine the time it takes to reach the dead band needs to be made to allow the controller sufficient time to change the rotor speed. Also, while operating in simple IG mode, the rotor converter is not controllable. This is why the grid parameters might be impossible to control. For a large grid connected system, operating in an IG mode might not be a problem, but in a small remote area power supply system it will make the whole system prone to network imbalance. For moving back to the normal DFIG operation will cause another torque transient if it does not operate in equivalent point.

2.6. Stress Analysis of the DC-Link Electrolytic Capacitor

The renewable energy-based power generation is growing very rapidly. Variable speed wind energy conversion systems and photovoltaic systems incorporate power electronic converters especially, back-to-back converters for their bidirectional power flow capability and high efficiency [46]. The aluminum electrolytic capacitors are always required in the renewable energy systems. The frequency and core temperature severely affect the properties of the electrolyte capacitor.

2.6.1. *Properties of an electrolytic capacitor*

Switching devices have been an indispensable part of modern power electronics. Switching devices cause ripples both in voltage and current which greatly affects the power quality. The electrolytic capacitor is largely used in the power electronics application as well. A high capacitor ripple current, caused by switching, diminishes the capacitor lifetime. The large capacitor and inductor size can reduce the ripple, but it will significantly affect the response time and expense. Renewable energy sources such as WECS or PV incorporate power electronic devices.

The dc-link ripple current can be caused by the switching of the power electronic devices such as, IGBT or MOSFET, the modulation technique and the inductor charging/discharging operation. Different types of modulation schemes affect the harmonic distortion differently. However, there will be harmonics of multiple order of the switching frequency. Usually, a high switching frequency reduces the harmonic distortion and results in fewer ripples current.

Although an aluminium electrolytic capacitor usually provides low impedance path, the aging process diminishes the low-impedance property. The evaporation of electrolytic liquid accelerates the aging process and cause an increase in ESR [47]. If a system consists of a switching device, it will definitely inject the harmonics in a dc-link or a capacitor branch. Harmonic components result in an increase of the ripple current. The elevation of the core temperature is caused by the high core loss which is resulted from the high ESR and high ripple current in the capacitor branch. The high temperature accelerates the evaporation process of the electrolyte and reduces the lifetime of the capacitor [48]. Power electronic

converter performance and reliability are highly dependent on the reliability of the capacitor. Therefore, it is very important to maintain the lifetime of the capacitor.

A converter system with power electronic devices will inject the harmonics in a dc-link or a capacitor branch. The harmonic components will increase the ripple current. The elevation of the core temperature is caused by the high core loss which is caused by the high ESR and the high ripple current in the capacitor branch. The high temperature accelerates the evaporation process of the electrolyte and reduces the lifetime of the capacitor [48]. The power electronic converter performance and reliability are highly dependent on the reliability of the capacitor. Therefore, it is very important to maintain the lifetime of the capacitor.

Also, the ESR is dependent on the ripple frequency. The ESR becomes smaller with the higher frequency. The ESR is very high at lower frequencies (100–300 Hz) whereas, the ESR is relatively much smaller in higher frequency region (above 1 kHz). Thus, the ripple current amplitudes of the lower frequencies are the most serious for the capacitor thermal stress. By reducing the low frequency amplitudes, the effective ESR and consequently the reduction of the volume of liquid can be largely improved.

In [61], authors analyzed the stress on the capacitor during regular voltage ripple. The voltage ripple is caused by usual amplitude modulation. The voltage ripple here is the width of the amplitude envelopes. Effects on the capacitor ripple voltage has been shown with the increase in ripple percentage and modulation frequency. In [62], a strategy was proposed to calculate the online estimation of the capacitance to make sure the capacitor is replaced before failure. A controlled ac current with lower frequency than the system frequency is injected into the input side to deliberately cause a voltage ripple in the output terminal. By calculating voltage and current ripple in the dc-link using digital filters, the capacitance will be determined through the recursive least square method.

2.6.2. Strategies to control capacitor core loss

In [63], a method was presented to prevent the failure of aluminum electrolytic capacitors used in the output filters of step-down dc-dc converters. The equivalent circuit of an electrolytic capacitor consists of the ESR and an inductor. The capacitance and the

inductance change with frequency, temperature and aging. As discussed earlier, the change in ESR is an indication of the change in the volume of the electrolytic liquid. Therefore, an online calculation of the ESR would definitely help to track the possible capacitor failure. The proposed technique in [63] estimated the capacitor ESR value, when the converter is operational on a real time basis. In order to do that, the usual relationship between the input current and the output voltage ripple is used. A new trend in dc-link ripple reduction is to manipulate PWM carrier waveform [56]–[58]. In [56], a method of actively-controlled PWM interleaving for back-to-back converters in order to suppress the dc-link capacitor harmonic current in the second carrier band and reduce the overall harmonic content is proposed. But no comprehensive method to reduce the ripple irrespective of their frequency has been proposed to minimize the thermal stress.

2.7. Data Analysis for Pattern Recognition:

In the RAPS system, an overwhelming number of data is received by the control system. These data need to be analyzed for appropriate decision making. However, analyzing the huge number of data can cause computational burden. For example, the length of a wind profile time series data measured at a 10-minute interval for a week will be 1008. If the number of locations is 200, then the weekly wind velocity database will consist of 200×1008 pieces of data points. Using Symbolic Aggregate Approximation (SAX), this dimensionality can be reduced considerably.

2.7.1. Theory of SAX algorithm

An algorithm was proposed by Keogh to reduce the dimensionality of data and ease the burden of calculation. This is called Symbolic Aggregate Approximation (SAX) [64]. Using the SAX algorithm, a time series is represented by characters significantly reducing the dimensionality. In [65], Keogh, Lin and Fu proposed a technique to find the most unusual time series subsequence. The brute force and the heuristic methods were used to discover the time series discord. In [66], authors used this algorithm for the assessment of the solar PV impacts on low voltage (LV) and medium voltage (MV) networks. The raw time series was

converted to PAA piecewise aggregate approximation (PAA) coefficients. Then, the PAA coefficients were converted to characters according to the level they are in as per Gaussian distribution. The voltage profiles were clustered according to their pattern using K-means algorithm. The cluster, containing unusual time series profile, was separated and subject to the brute force analysis. The voltage profile with the largest non-self-match distance was detected and this was detected as the most anomalous time series. Then it was analyzed, and the load flow analysis was performed on it to detect the problem.

If a time series data is considered, m of length n. $m = m_1, m_2, m_3 \ldots, m_n$. After normalizing the time series, it will be converted to a w-dimensional time series, such that W<<n, using Piecewise Aggregate Approximation (PAA). The formula for calculating PAA i

$$t_i = \frac{w}{n} \sum_{k=\frac{n}{w}(i-1)+1}^{\frac{n}{w}i} S_k$$

(2.1)

If the PAA series is expected to be symbolized using k-alphabet, then the Gaussian distributed curve has to be divided into k-1 breakpoints.

2.7.2. Implementation of SAX on a raw data series

The above-mentioned mathematical operation is applied to a wind profile data of 100 days as shown in Fig. 2.7. It shows that the raw time series is presented by the blue line, and the PAA approximation level is shown by red line. The time series will be presented by the 5 alphabet and the word size will be 8. The larger the value of the word length, the resolution will be higher, but this will increase the computational burden.

The Gaussian curve is divided into 4 break points. The values of them are obtained from the Gaussian distribution table. The symbolization of the PAA series will be carried out in an ascending manner. Any value equal or less than the 1st level will be assigned the character 'a', equal or less than the 2nd level will be assigned character 'b', equal or less than the 3rd level will be assigned character 'c', and so on. The dimensionality reduction of the raw time series using the SAX representation preserves its essential characteristics.
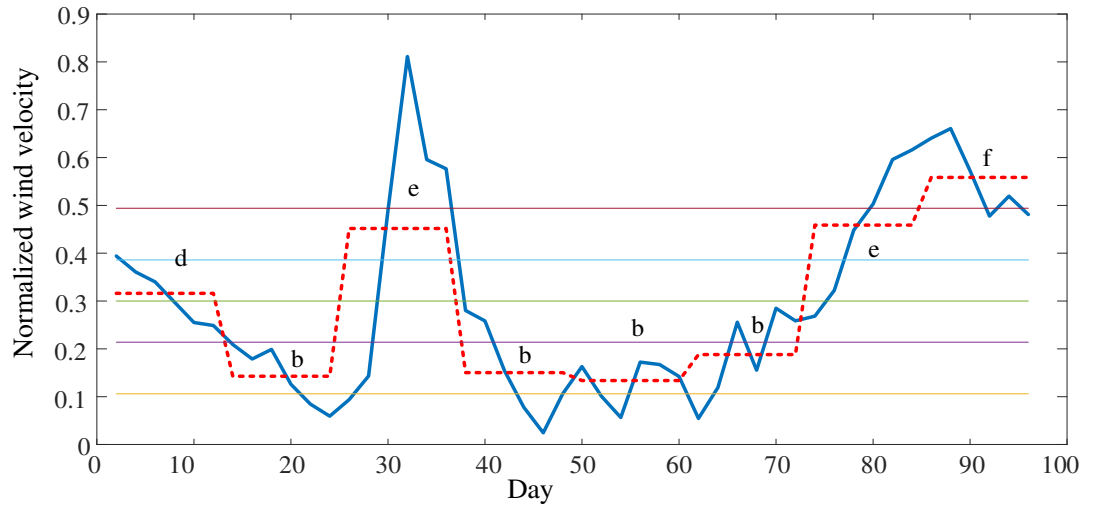
Fig. 2.8. Converting time series into SAX representation
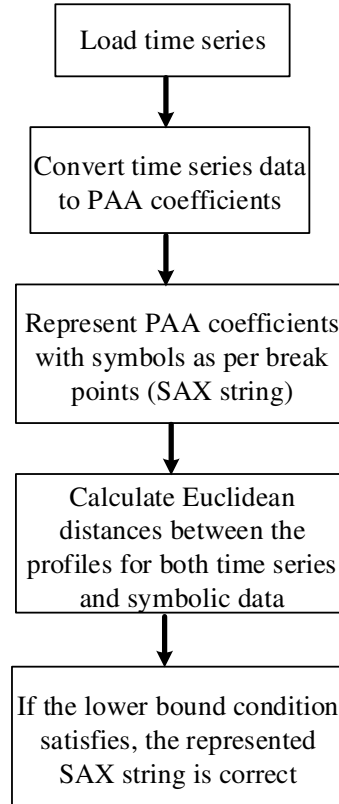
Fig. 2.9. SAX representation process

It is expected that the Euclidean distance between the raw time series is greater or equal to the Euclidean distance of the raw time series. If this condition is fulfilled, it will satisfy the "Lower Bounding" of the distance. The equation is as shown in (2.2):

$$D(m_1, m_2, m_3, ..., m_n) \quad D(l_1, l_2, l_3, ..., l_n)$$

<div align="right">(2.2)</div>

The right hand side of the above equation is the lower bounding distance of the SAX representation. Fig. 2.8 shows the flow chart of the SAX representation process.

2.7.3. Clustering of similar profiles
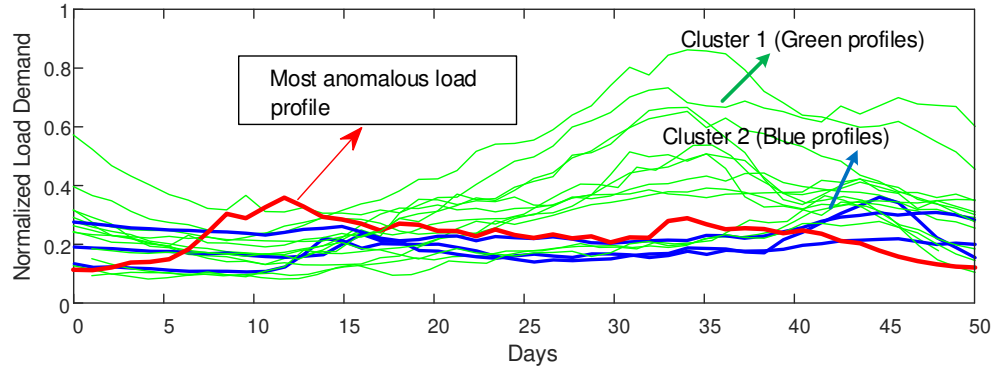
Fig. 2.10. Discriminated wind profile with SAX and clustering algorithm

In previous section, the algorithm for converting data series to SAX strings has been discussed. However, the ulterior goal of dimensionality reduction of raw time series is to increase the efficiency of further data analysis. In this thesis, classifying data into different groups is of interest. For this, a pattern recognition algorithm is used. Fig. 2.9 demonstrates the output of the pattern recognition strategy

The load profiles of 17 houses every hour for 50 days is shown in Fig. 2.9. All 17 load profiles are converted to SAX string. After that the clustering is required. From the many clustering algorithms, the K-means clustering has been used to make 3 clusters of the load profile. After that, the brute force algorithm is applied to each cluster. The profile with the highest Euclidean distance within the cluster is the most anomalous one. Cluster 3 which is the red signal is the most anomalous one. Instead of K-means, support vector machine (SVM) can also be used for clustering data series.

2.8. Summary

This chapter provides the general information about the challenging aspects of wind energy based RAPS systems. A detailed literature review on the control strategies of WECS

in a RAPS system and their performances are discussed. The importance of the improved dynamic performance of a WECS and the lifetime improvement of different WECS components are explored as well. In addition, the importance of efficient data processing and the prospect of an algorithm are inspected. Further, existing knowledge presented in the current literatures have been a subject to the discussion for their relative merits and demerits which provides the background for the following chapters. From the literature review presented in this chapter, it can be concluded that the reliability improvement of RAPS systems has not been given much attention which builds the foundation for this thesis.

Chapter 3

Enhanced Frequency Support from a WECS Integrated with a SMES in a RAPS System

Foreword

In a small standalone power supply system containing renewable energy, the frequency response is usually supported during frequency excursion by the conventional generators only. This may result in a less effective recovery of the system frequency in a wind energy dominant standalone system. The support from the wind turbine in the frequency regulation will significantly improve the recovery performance. However, the natural inertia of the variable speed wind turbine is very small compared to that of the conventional generators. Therefore, a fast responding energy storage can significantly improve the frequency response capability. In this chapter, a control technique has been proposed to utilize the superconducting magnetic energy storage (SMES) to be integrated with the permanent magnet synchronous generator based wind turbine to improve the power system frequency regulation and the results are found to be promising.

3.1. Background

A standalone power supply system provides the electric power to remote communities where the electric power cannot be supplied by the utility grid [68]. In an optimally sized hybrid standalone power supply system, a sudden change of a large load or the occurrence of a fault in the network can cause significant transients causing a frequency deviation in the network [69]. To maintain the frequency, the generators should quickly adjust their power

outputs. Conventional synchronous generator automatically decelerates its rotor speed to increase the power output when the system frequency drops. But, a variable speed WECS has a very limited natural inertia [70] such that it cannot automatically release the kinetic energy as it operates under a maximum power point tracking operation. The frequency regulation support from DFIG based wind turbines has been studied more widely compared to other WECS [71]. In [10], the capability of PMSG based WECS to participate in the frequency recovery was investigated and the kinetic energy is utilized during frequency event using virtual inertia and a droop control technique. However, this is not an efficient solution. A power reserve has been found to be able to significantly improve the frequency response capability of the hybrid standalone power supply system. The reserved power can be obtained either by operating the wind generators away from their maximum power points or by adding an external energy storage.

Superconductors are those materials which show zero electrical resistance, when the temperature is below the critical value (Tc). Fig. 3.1 shows the superconductivity characteristics.
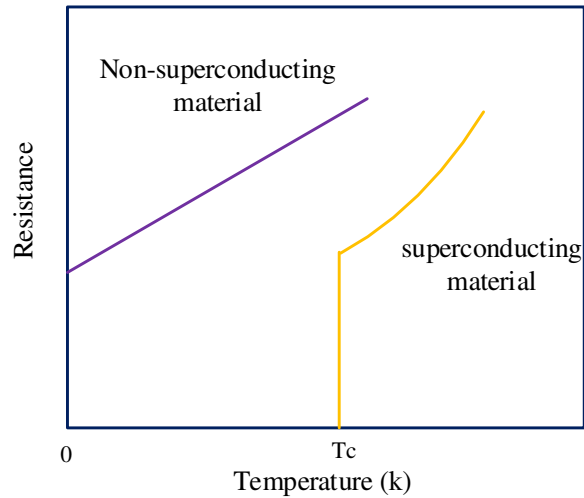
Fig. 3.1. Temperature vs resistance curve

Superconductivity is a quantum-mechanical phenomenon. Superconductors have not been feasible for use in a large-scale operation due to the high cost of the liquid helium-needed for cooling the conductor to below its critical temperature. However, with the availability of the

high temperature superconducting coil (HTS), that only requires the low-cost liquid nitrogen, it is now possible to use it for more practical applications [72],[73]. The high temperature superconducting magnetic energy storage (SMES) is a promising alternative to the conventional energy storage due to its fast response capability and high power density. However, despite the development of HTS material, the relative cost of the SMES is still much higher than other energy storages. The comparison of expense is given below in Table 3.1.

TABLE 3.1
COST COMPARISON OF THE HIGH-POWER STORAGE TECHNOGIES

Storage Technology	Power Cost ($/kW)
Super-capacitor	100–400
SMES	200–500
Flywheel	150–400

Superconductor had been studied as fault current limiters in WECS [74]. In [75], the superconducting fault-current-limiter-magnetic-energy-storage (SFCL-MES) was used both for power smoothing and fault current limiting.

Reference [76] proposes the use of supercapacitors to enhance the frequency response capability for PMSG based wind energy conversion system in remote area power supply systems. However, the SMES has been shown to be superior to the supercapacitors in many aspects. The SMES has longer lifespan than the supercapacitor; the SMES has a potential lifetime of 25 years, and the potential lifetime of the supercapacitor is 15 years [77]. Also, the SMES has very low resistance, and therefore it has lower leakage power than the supercapacitors [78]. As the SMES will only be activated during high frequency fluctuations, the idle time will usually be quite long; with higher leakage power the energy will be reduced more.

The SMES has faster response; 1–5 ms compared to 5–20 ms for the supercapacitor [79], which will help in quickly compensating any high frequency deviations. The slower response of the supercapacitor will increase the burden on the diesel generator. Also, the nominal power of the SMES (10 kW–1 MW) is much higher than that of the supercapacitor (1–10 kW) [80].

In this chapter, the frequency regulation by WECS with the support from the SMES has been explored. A new strategy to improve the frequency response capability of the WECS by the control of the SMES has been proposed. Also, the charging/discharging conditions and the circuit topology to support this will be discussed.

3.2. Inertial Response of Variable Speed PMSG

The swing equation of a synchronous machine is given by (3.1):

$$\frac{2H_s}{\omega_s}\frac{d^2\delta}{dt^2} = P_m - P_e \tag{3.1}$$

where, δ is the angular displacement of the rotor, P_m and P_e are the mechanical and the electrical power respectively, ω_s is the synchronous frequency and H_s is the constant for the system inertia. The higher the value of H_s, the higher is the inertia.

If there is a system consisting a synchronous generator and a variable speed WECS, the H_t for the combined system will be as follows,

$$H_t = \frac{2H_s\frac{J_s\omega_e^2}{2P_s^2} + KE_w}{S_N} \tag{3.2}$$

where, P_s is the synchronous generator pole pair number, S_N is the total MVA generation capacity of the system and J_s is its constant for inertia. KE_w is the kinetic energy of the WECS. Since the variable speed WECS follows MPPT operation, it may not be possible to utilize the kinetic energy for frequency response. If the number of the variable speed WECS in a system is high, the effective inertia decreases as the total kinetic energy is unchanged and the denominator of the equation gets larger.

The turbine characteristic can be derived as follows:

$$P_m - P_e = P_a \tag{3.3a}$$

31

$$P_a = J_w \omega_r \frac{d^2\delta}{p_w^2 dt^2} = J_w \omega_r \frac{d\omega_r}{p_w^2 dt} \tag{3.3b}$$

P_a is the accelerating/decelerating power which accounts for any imbalance between P_m and P_e. The rate of change of δ is the rotor angular frequency, ω_r. P_w is the WECS pole pair number and J_W is its natural inertia

Rearranging the right hand term of (3.3b)

$$J_w \omega_r \frac{d\omega_r}{p_w^2 dt} = \frac{J_w \omega_r d\omega_r}{\omega_s d\omega_s} \cdot \frac{\omega_s d\omega_s}{p_w^2 dt} \tag{3.3c}$$

Comparing (3.3b) and (3.3c),

$$P_a = J_{art} \omega_s \frac{d\omega_s}{p_w^2 dt} \tag{3.3d}$$

where,
$$J_{art} = \frac{J_w \omega_r d\omega_r}{\omega_s d\omega_s} \tag{3.4}$$

J_{art} is the artificial inertia of wind turbine. If the wind turbine provides dynamic support using its stored energy when the frequency drops, the amount of energy released is indicated as (3.5) [81]:

$$\Delta E_w = \int (P_m - P_e) dt = \int (\frac{J_{art} \omega_s}{p_w^2}) d\omega_s \tag{3.5}$$

From (3.5) and (3.2), the system constant H_t is expressed as

$$H_t = \frac{\frac{J_s \omega_e^2}{2 p_s^2} + \frac{1}{2} J_{art} (\frac{\omega_e}{p_w})^2}{S_N} \tag{3.6}$$

32

Equation (3.7) shows that the natural inertia and the pre-disturbance rotor speed determine the inertial response, ω_{r0}.

$$J_{art} = \frac{J_w \omega_r \, d\omega_r}{\omega_s \, d\omega_s} \approx \frac{\Delta \omega_r}{\Delta \omega_e} \cdot \frac{\omega_{r0}}{\omega_e} J_w \tag{3.7}$$

The amount of the released energy depends on the wind velocity, the current rotor speed and the pre-frequency-event rotor speed.

If the system frequency decreases, the inertia control of WECS will reduce the rotor speed in order to increase its active power output by releasing the kinetic energy. But it will also reduce the reference power in the MPPT control which may cause secondary event.

3.3. Frequency Response by Suboptimal Power Point Tracking with Artificial Inertia Strategy

3.3.1. Control mechanism of PMSG based wind turbine

A single-switch three-phase switch-mode rectifier (MSC) converts the ac output voltage of the PMSG to a dc voltage which will be converted again to an ac output by a controlled inverter (GSC). The MSC consists of a three-phase diode bridge rectifier and a boost converter. The rectifier output can be controlled by controlling the duty cycle for the IGBT gate pulse at any wind speed to extract maximum power from the wind turbine or to control the rotor angular speed. In short, the boost converter in the switch mode rectifier works as a maximum power point controller. The three phase inverter in the GSC is vector controlled which is used to regulate the output voltage and frequency during power fluctuations.

To make the analysis easier, the PMSG is modelled in a dq-components based rotor synchronous frame. d-axis is aligned with the rotor flux and q- axis is perpendicular to it. The flux caused by the permanent magnet on the rotor is in the direction of d-axis. A phase locked loop (PLL) ensures the synchronization between dq and three phase reference frames. The voltage equations of PMSG stator are given in (3.8a) and (3.8b):

$$V_{ds} = R_s i_{ds} \quad w_r \quad {}_{qs} + p \quad {}_{ds}$$

<div align="right">(3.8a)</div>

$$V_{qs} = R_s i_{qs} \quad w_r \quad {}_{ds} + p \quad {}_{qs}$$

<div align="right">(3.8b)</div>

Where

$$_{ds} = L_d i_{ds} + \quad {}_r$$

<div align="right">(3.9a)</div>

$$_{qs} = L_q i_{qs}$$

<div align="right">(3.9b)</div>

Where, L_d is the d-axis inductance and L_q is the q-axis inductances in the stator respectively. λ_{ds} and λ_{qs} are dq-stator flux. Rs is the stator resistance. The rotor speed is w_r. λ_r is the rotor flux.

The rotor flux in a permanent magnet synchronous generator is constant. ,

$$\frac{d}{dt}{}_r = 0$$
;

Substitute from equations (3.9a) and (3.9b) in (3.8a) and (3.8b) yield

$$V_{ds} = R_s i_{ds} \quad w_r L_{qs} i_{qs} \quad L_d p i_{ds}$$

<div align="right">(3.10a)</div>

$$V_{qs} = R_s i_{qs} \quad w_r L_d i_{ds} \quad L_q p i_{qs} + w_r \quad {}_r$$

<div align="right">(3.10b)</div>

The electromagnetic torque generated in the machine is calculated from (3.11).

$$T_e = \frac{3p}{2}(i_{qs} \quad {}_{ds} \quad i_{ds} \quad {}_{qs}) = \frac{3p}{2}\{i_{qs} \quad {}_r \quad (L_d \quad L_q)i_{ds}i_{qs}\}$$

<div align="right">(3.11)</div>

The formula for rotor speed is given in (3.12).

$$w_r = \frac{p}{Js}(T_e \quad T_m)$$

<div align="right">(3.12)</div>

The PMSG equations are manipulated to be expresses as below:

$$i_{ds} = (\quad V_{ds} \quad R_s i_{ds} + w_r L_q i_{qs})/ sL_d$$

<div align="right">(3.13a)</div>

$$i_{qs} = (\ V_{qs} \quad R_s i_{qs} \quad w_r L_d i_{ds} + w_r \ _r)\,/\,sL_q \tag{3.13b}$$

The control objective of the switch mode rectifier is to control the duty cycle of the switch in Fig. 3.2 so that the machine follows the maximum power point. For different wind velocity, the rotor angular frequency has to be different in order to follow the maximum power point operation. Also, controlling the angular velocity means controlling the torque. Although, mechanical torque is resulted from the wind velocity but controlling the inductor current through changing the duty cycle of the IGBT gate pulse, electromagnetic torque can be changed. This process includes the following steps:

1) Measure reference rotor angular frequency, ω_r,

2) Determine the reference torque, τ_{ref} ,

3) Calculate the dc current reference by PI controller,

4) The PI controller is fed the error between reference and measured dc-current and it produces the appropriate duty cycle for switching to control the generator torque.
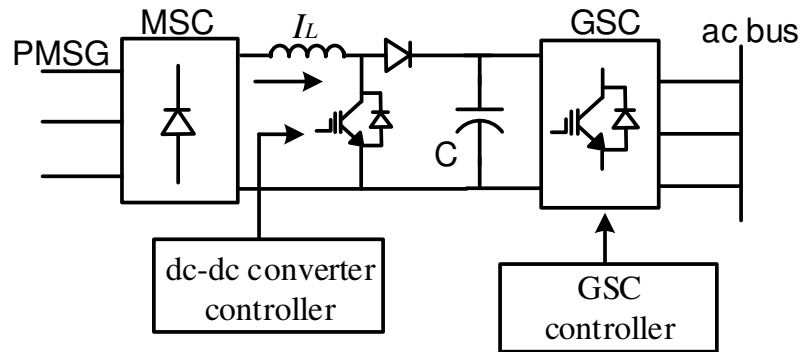
Fig. 3.2. PMSG based wind turbine

The electromagnetic torque is controlled along the maximum power point curve which depends on the wind velocity and rotor angular frequency. Whether the rotor needs acceleration or deceleration, depends on the difference between the turbine mechanical torque and the reference generator electromagnetic torque. If the rotor angular speed is less than the reference speed, the mechanical torque is larger than the electromagnetic torque, and the generator will be accelerated. The generator will be decelerated if the rotor speed is higher

than the reference speed. This is how, the mechanical and electromagnetic torque need to settle down to the reference operating point at any wind speed and need to follow the maximum power point curve.

3.3.2. Suboptimal power point tracking strategy

The frequency response capability of the PMSG based wind turbine can be improved by using an artificial inertial response which is achieved through the control of a boost converter. By controlling the boost converter duty cycle, the power output and the torque can be controlled resulting in a frequency support. The control equations for the inductor current are shown in (3.14)–(3.15). The output power of the PMSG wind generator depends on the current, I_L flowing through the inductor L. The rotor speed reference, ω_r* is generated by tracking the operating curve according to the output power demand. The reference power is intended to be captured with a PI controller which is fed with the difference between the reference and the measured rotor speed. The output of the PI controller will be the reference inductor current according to (3.14). The reference inductor current will be compared with the actual inductor current and the difference will be passed through another PI controller which will produce the appropriate duty cycle of the boost converter pulse as the conditions given in (3.15).

$$\Delta\omega_r = \omega_r^* - \omega_r \tag{3.14a}$$

$$I_L^* = K_p\Delta\omega_r + K_i\int\Delta\omega_r d\omega_r \tag{3.14b}$$

$$\Delta I_L = I_L^* - I_L \tag{3.15a}$$

$$D = K_p\Delta I_L + K_i\int\Delta I_L dI_L \tag{3.15b}$$

The artificial inertial response can be emulated by adding a decelerating term to the reference electromagnetic torque, from which the appropriate value of the boost converter duty cycle needs to be generated. In a stable condition, the electromagnetic torque and the mechanical torque should be equal. The change in reference torque reduces the rotor speed to

emulate the inertia which improves the frequency response. The artificial inertia will only be operational during frequency event through a supplementary controller. The supplementary inertia controller will sense the change in system frequency and will be activated. This will reduce the rotor speed to release the energy. From (3.3) we obtain the additional power associated with inertial response which will be used during the frequency regulation. By releasing the kinetic energy system operating point will be moved from the reference operating point.

Furthermore, to retrieve the previous operating point, the turbine will have to absorb an additional mechanical power. This may cause a secondary frequency event. However, Fig. 3.3 shows that when the WECS operates along the right suboptimal power point (SOPPT) curve (corresponds to a higher rotor speed than that of the MPPT curve), reducing the rotor speed will release the reserved power.
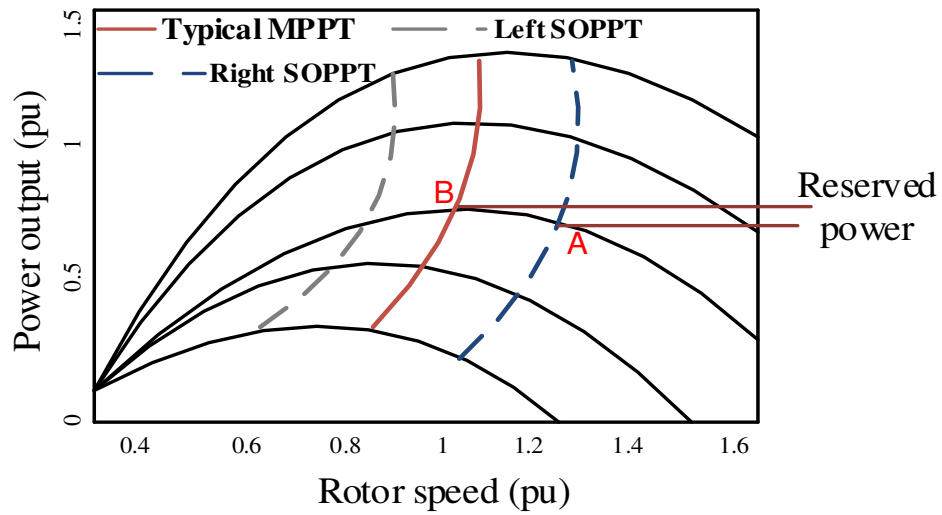
Fig. 3.3. Wind turbine power curves

If it is required from the wind generators to support frequency response for a long term, mere kinetic energy reserve will not be sufficient. A power reserve will improve the frequency support and power can be reserved by operating the machine away from MPP.

In regard to wind turbine, mechanical output power is determined by,

$$P_{wind} = \frac{1}{2} \rho A v^3 C_p(\lambda, \beta)$$

(3.16)

$$\lambda = \frac{\omega_r R}{v}$$

(3.17)

Where, ρ is the air density, A is the wind swept area, υ is the wind speed and ω_r is the rotor speed. $C_p(\lambda, \beta)$ is the power efficiency of the WECS. It is a function of tip speed ratio λ and pitch angle β. The maximum power point tracking (MPPT) strategy is implemented by tuning λ and β. For SOPPT control, the reserved power P_{res} is determined by

$$P_{res} = \frac{1}{2} \rho A v^3 [C_p(\lambda_1, \beta_1) - C_p(\lambda_2, \beta_2)]$$

(3.18)

Where, $C_p(\lambda_1, \beta_1)$ and $C_p(\lambda_2, \beta_2)$ are the wind turbine power efficiency coefficient, respectively for MPPT and SOPPT. In order to maintain a constant power reserve as in delta control, turbine will be operated at higher than optimum speed (the optimum speed is tracked at maximum power point).

3.3.3. Artificial inertia controller

During frequency dip, the rotor speed will decrease resulting in the release of stored energy and increase in power output. The output power of the PMSG wind generator depends on the current I_L flowing through inductor L. The PMSG based WECS can operate under wide speed range due to fully rated converters [82]. The new operating point clearly corresponds to a higher output power thus the retrieval of the initial operating point of the system will not be necessary. Also, the additional mechanical power demand for the retrieval will not be needed as well. If the system frequency becomes stable, the supplementary controller will be deactivated.

The control system for the boost converter to implement the supplementary inertia controller is shown in Fig. 3.4. During the frequency dip, this supplementary inertia controller

will be activated to increase the power reference as given in (3.3) which will generate the appropriate boost converter duty cycle to emulate a decelerating torque. Consequently, the operating point is shifted to B from A, as shown in Fig. 3.3, releasing the reserved power.
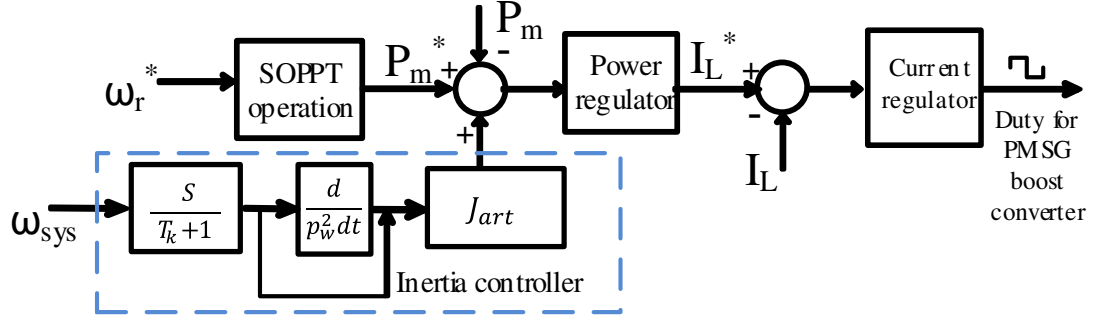
Fig. 3.4. Frequency response control with artificial inertia

A low pass filter with a time constant, T_k has been added to filter out the high frequency distortions so that they do not compromise the supplementary controller performance. The value of T_k is dependent on the cut-off frequency of the low pass filter. In this example, the short term frequency disturbances due to harmonics above 50 Hz are filtered out. Therefore, the constant will be 0.02. The value of J_{art} is derived from (3.8). It is calculated from the pre-disturbance rotor and electric angular frequency, and also the change in rotor speed and electric angular frequency. The change is rotor angular frequency is dependent on the difference between the SOPPT and MPPT along the power curve.

TABLE 3.2

SMES PARAMETERS

Parameter	Value
Coil inductance	0.8 H
No of coil turns	415
Max coil current, I_s^{max}	100 A
Min coil current, I_s^{min}	25 A
Rated power	80 kW
DC-link voltage	800 V

3.4. Proposed Frequency Response Strategy

3.4.1. PMSG based WECS with SMES configuration

The discovery of the high-temperature superconducting (HTS) materials aroused promising opportunity for large scale operation, because they carry significant current above the boiling point of liquid nitrogen at 77.4 K (-196 ^{0}c). Also, from point of cost efficiency, a liter of helium costs \$25 as opposed to 60C for a liter of nitrogen. The University of Wollongong is in possession of an iron cored HTS built with BSCCO-2223/Ag as shown in Fig. 3.5. The Bi–Sr–Ca–Cu–O system has three superconducting phases forming a homologous series i.e. Bi-2201, Bi-2212 and Bi-2223. Among them, Bi-2223 has a transition temperature of 110K which is a lot higher than the low-temperature superconductor operating at the temperature of liquid helium. The BSCCO-2223/Ag HTS can be of two types of configurations i.e. warm core and cold core. Cold core design requires the cryostat volume over 10 times that of warm core design. This HTS inductor is designed for research purpose only and will not be operated continuously. Also, due to budget limitation for liquid nitrogen cooling and space constraint for testing, we opted for warm core configuration for SMES operation. The specifications are in Table 3.2.
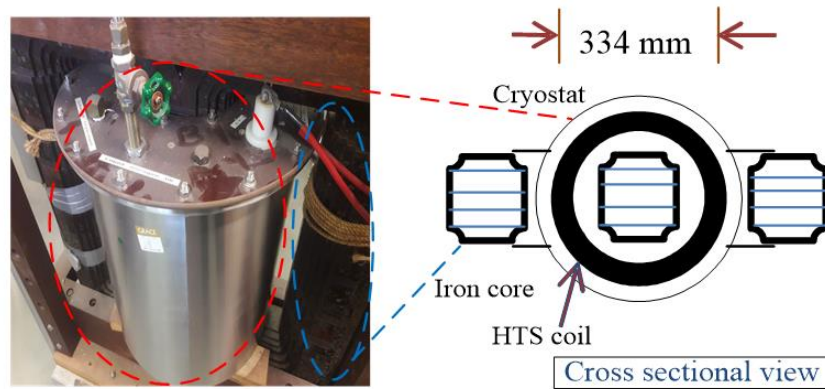
Fig. 3.5. The iron-cored HTS coil at the University of Wollongong and its cross-sectional view from the top.

The SMES will be used for frequency regulation and it is coupled to the dc-link through a two-quadrant dc–dc chopper as shown in Fig. 3.6. The merit of this configuration is that it

does not require any additional inverter to be connected to the ac grid. The SMES will be in operation when the demand power abruptly crosses the limit. The chopper is responsible for the control of charging and discharging control. The bypass switch enables the inductor current to circulate in a perpetual loop during standby (using a thyristor).
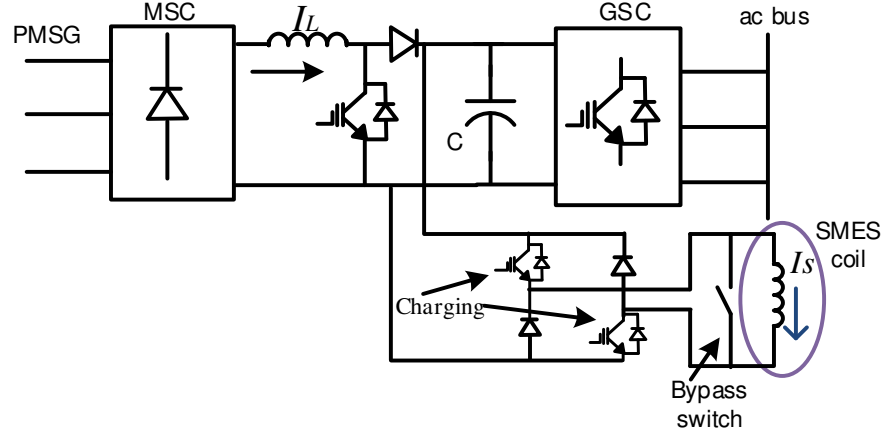
Fig. 3.6. Simplified topology of PMSG based wind turbine with SMES

3.4.2. SMES charging and discharging control

P_{ch} is the auxiliary SMES charging power demand. This term comes in operation when the reserved power is utilized to charge the SMES coil. In the case of the charging of the SMES, it is assumed that the machine is operating along the SOPPT curve (left or right) maintaining a constant power reserve. So, an auxiliary controller will increase the wind turbine power demand shifting the operating point to utilize the reserved power for charging. Fig. 3.7 shows the boost converter control for charging the SMES. After the charging is completed, the corresponding IGBTs in the chopper will be blocked. The machine can then move back to the SOPPT operation.
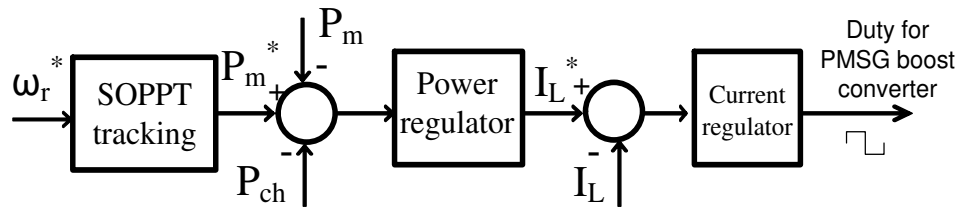
Fig. 3.7. PMSG boost converter control for charging

During frequency excursion, the system frequency, f_{ref} is different than the reference frequency, f_{ref}^*. The frequency fluctuation can either be slow or fast. For slow variation, the support from WECS is not necessary since the governor of the diesel generator will have sufficient time to cover the demand generation mismatch. Also, since energy density of SMES is very low, it can only mitigate the fluctuations with high ramp. A high pass filter with appropriate time constant will filter out the slow fluctuations and the frequency regulation will control the SMES current to support the system frequency regulation as shown in Fig 3.8.
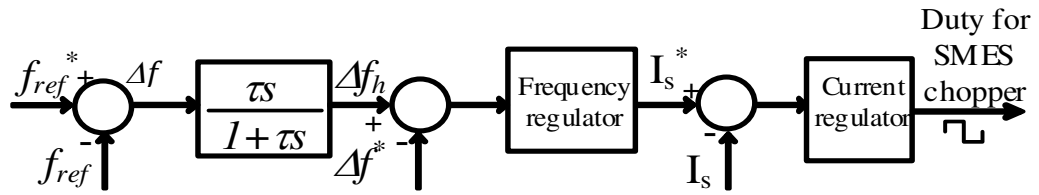
Fig. 3.8. dc chopper control for SMES during frequency regulation

The charging power of the SMES should not be more than the reserved power due to suboptimal power point tracking. If the charging power becomes more than the reserved power, there might be a secondary frequency event due to sudden additional power demand. Fig 3.9 shows the control to deal with the issue. However, the SMES power storage should be enough to be able to handle the connection or disconnection of the highest load in the system.
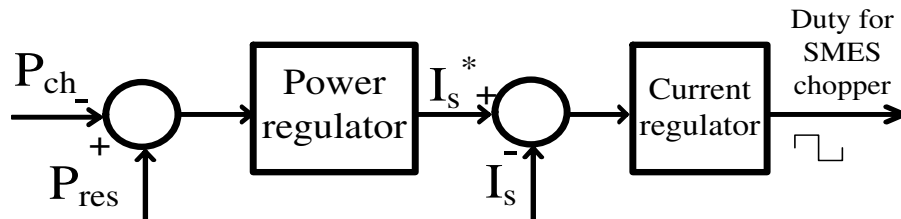
Fig. 3.9. dc chopper control with SMES charging topology
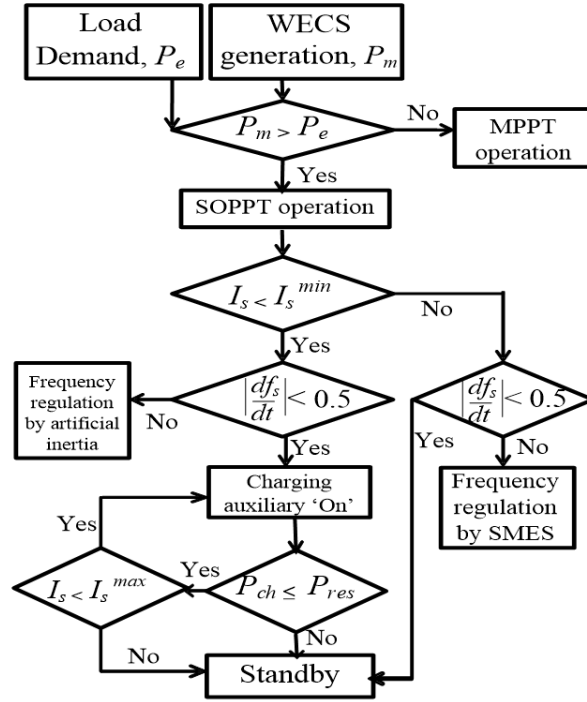
Fig. 3.10. Algorithm for proposed frequency regulation by SMES

3.4.3. Proposed algorithm for frequency regulation through SMES supported WECS

During the frequency event, the SMES coil will discharge to support the primary frequency response. The SMES will support frequency deviations with ROCOF of more than 0.5 Hz/s. Although, there is no rigid limitation for RoCoF in Australian grid code, the AEMO report [100] referred detailed technical studies undertaken by SONI and EirGrid. The studies indicated that, during times of high wind generation following the loss of the single largest credible contingency, RoCoF values between 0.5 Hz/s and 1.0Hz/s could be experienced on the island power system [101]. Therefore, the lower limit 0.5 Hz/s has been chosen as the reference in this thesis.

It is high power density makes it capable of compensating a high ramp. The high frequency component of the fluctuations Δf_h is extracted using a high pass filter which will then be mitigated through SMES charging/discharging.

Some constraints should be maintained for the smooth operation of WECS with the SMES module. The SMES coil cannot be charged more than the available reserved power as per the SOPPT curve. Also, the charging cannot be activated during frequency event. If the SMES coil current, I_s is below the minimum value, I_s^{min}, wind turbine will participate in frequency regulation using the SOPPT algorithm supported by artificial inertial response. Fig. 3.10 shows the flowchart of the proposed algorithm.

3.5. Simulation and Verification of Proposed Algorithm in a Test RAPS Network
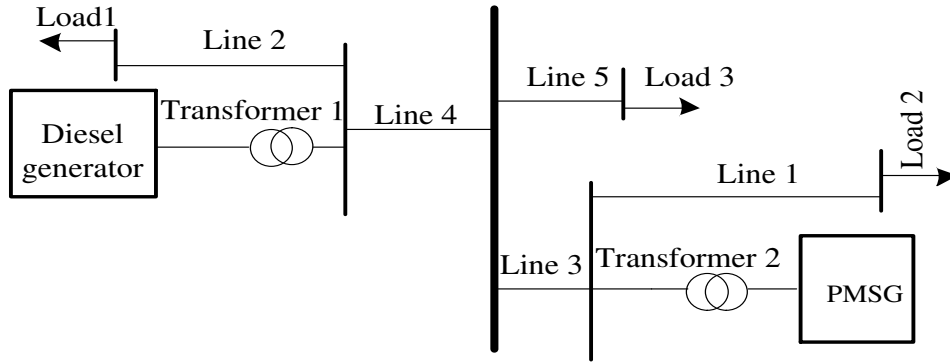
Fig. 3.11. Hybrid standalone power supply test system.

TABLE 3.2
RAPS PARAMETERS

PARAMETERS	VALUES
Load 1 impedance	0.085+j0.004
Load 2 impedance	0.085+j0.004
Load 3 impedance	4.01+j0.27
Line 1 impedance	2.56+j0.332
Line 2 impedance	0.104+j0.135
Line 3 impedance	3.564+j2.661
Line 4 impedance	3.976+j5.127

Line 5 impedance	6.141+j3.006
Transformer 1 rating	11 kV/2.4 kV, 1.5 MVA
Transformer 2 rating	11 kV/0.4 kV, 1.5 MVA
Diesel generator rating	500 kVA, 2.4 kV
PMSG rating	500 kW, 0.4 kV

The remote area standalone system used for the simulation is illustrated in Fig. 3.11, which will be used to test the proposed frequency control strategy in a PMSG-based wind turbine. The system consists of a 500 kVA diesel generator and a 500 kW PMSG based wind turbine. The frequency regulation with the SMES is simulated.

At 14 second from the start of the simulation, a frequency event is staged by a sudden increase in the load. An abrupt increase in the load demand causes the frequency to drop to 49.4 Hz within 0.25 s which is much higher than the allowable ROCOF of 0.5 Hz/s. The system frequency is recovered at about 15.25 s. As the wind turbine cannot participate in the frequency regulation, the additional power demand for the system frequency recovery is supported by the diesel generator only. The diesel generator has droop controller.

As discussed in Section 3.3, the artificial inertial response is supported by the SOPPT operation. This can be utilized to improve the system frequency regulation. But the frequent excursion leading to output power adjustment and the sudden torque variation which will cause a significant stress on the drive train which may deteriorate the life span of the machine. Also, this process to regulate frequency may not be fast enough for quick restoration of the frequency. On the other hand, the SMES has high power density and very fast response capability. It will also relieve the stress on the drive train and help avoid the fluctuating torque as shown in Fig. 3.12, making it more reliable for frequency support.
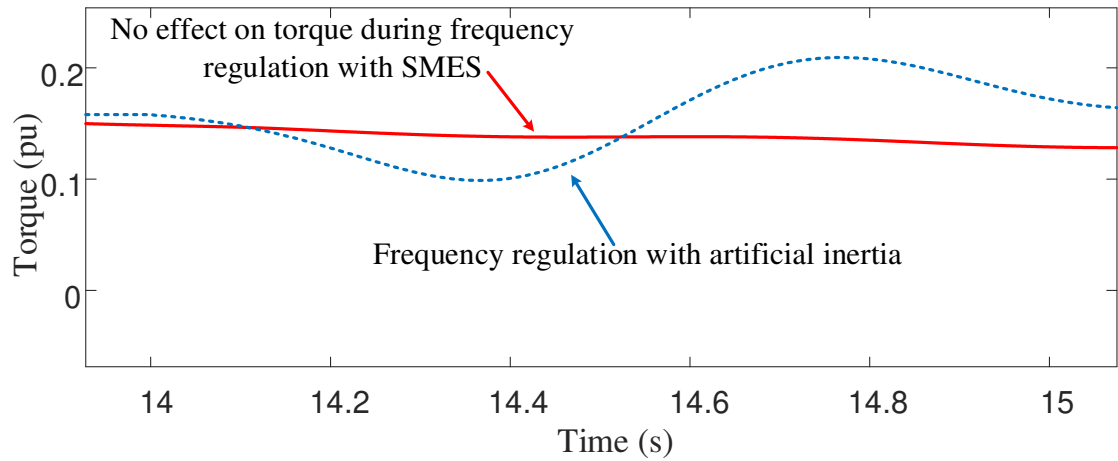
Fig. 3.12. Torque variation during frequency excursion event

With the integration of the SMES, the frequency recovery is met by the SMES and the diesel generator. Fig. 3.12 shows the SMES power support to regulate the frequency deviation started at 14th second. When the SMES is carrying out the frequency regulation, the supplementary controller for artificial inertia with the SOPPT will be kept deactivated.
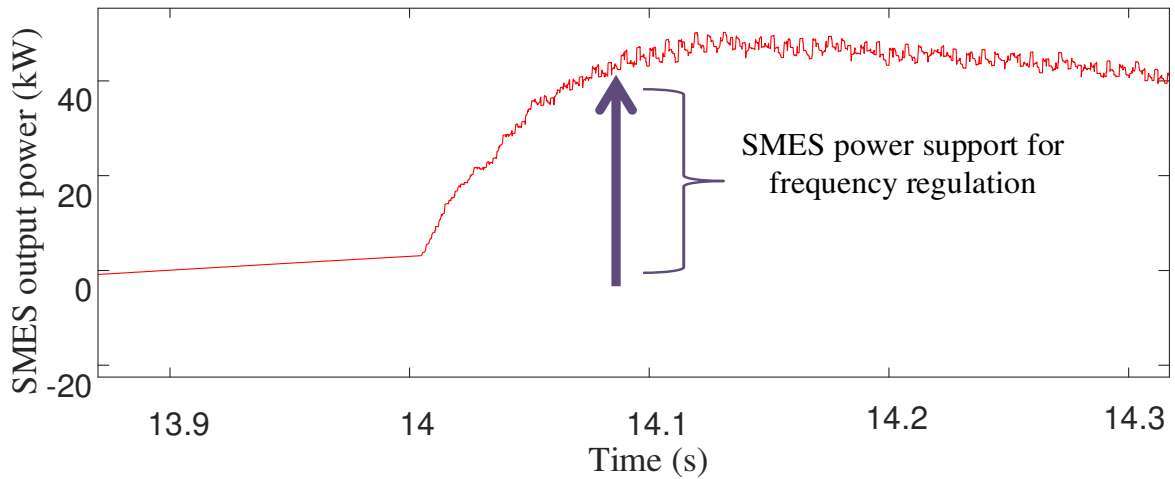
Fig. 3.13. SMES power support during frequency event
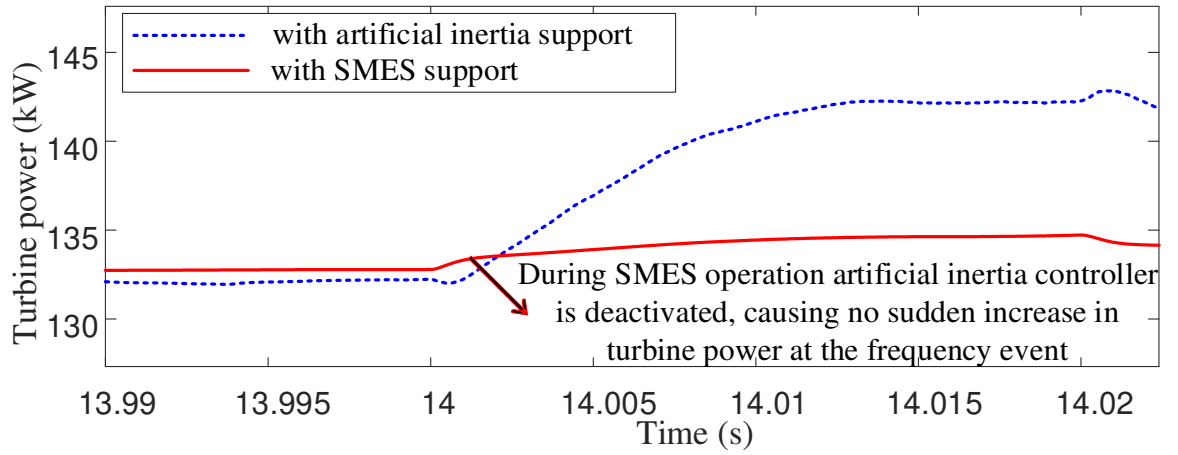
Fig. 3.14. Wind turbine power output

As shown in Fig. 3.14, during the support from the SMES, the turbine power is almost unchanged, whereas for frequency regulation by using the artificial inertia, the turbine power increases rapidly at 14th second, and this causes significant stress on the drive train.

To demonstrate that the SMES is superior to the supercapacitor for frequency control, the supercapacitor has been used as an alternate supplementary source. The charging and the operating algorithms have to be modified because the SMES is a current source and the supercapacitor is a voltage source.

If the power support from the SMES is fast enough, it would cause the power support from the diesel engine less significant. The burden to support the frequency regulation will be significantly low. From Fig. 3.15 it is evident that the diesel support is significantly low when the SMES is supporting. Even the diesel support is much lower than the diesel output during super-capacitor support since the SMES has faster response than the super-capacitor.
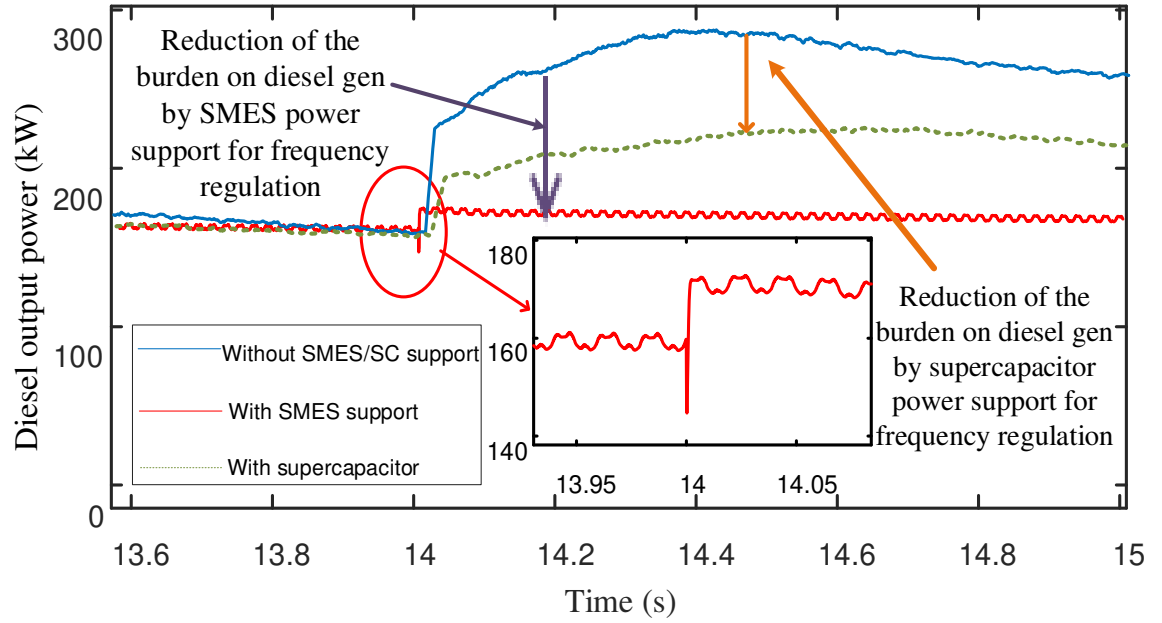
Fig. 3.15. Burden on the diesel generator with SMES and supercapacitor
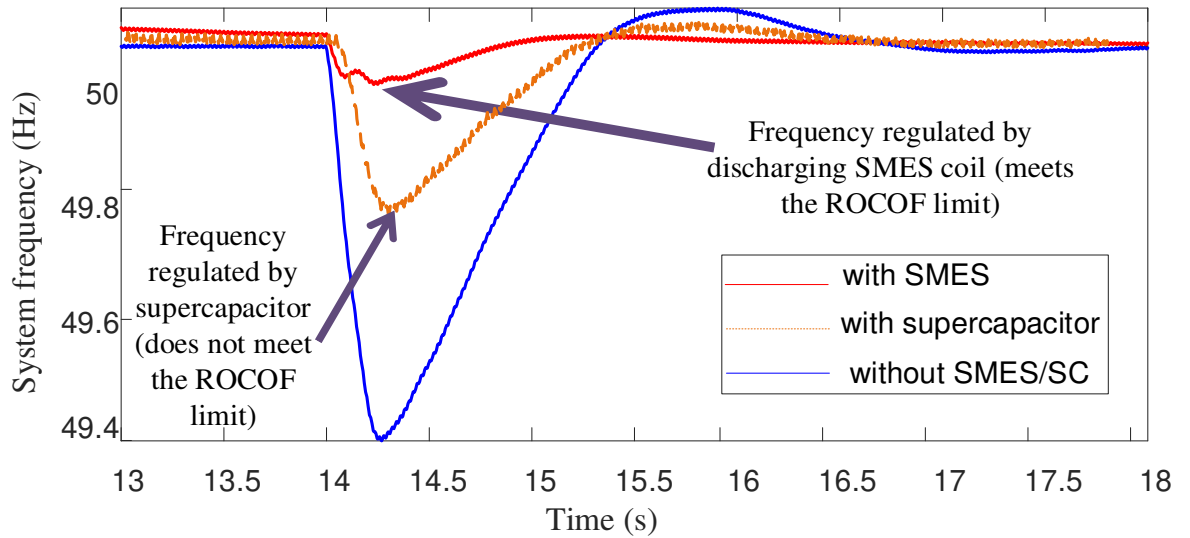
Fig. 3.16. System frequency improvement using SMES and supercapacitor.

Finally, Fig. 3.16 exhibits the significantly improved system frequency with the proposed frequency regulation by the SMES compared to that using the super-capacitor. With the SMES, the system frequency drops to 49.95 Hz in 0.25 s, which is well below the allowable ROCOF limit, but with supercapacitor, the system frequency drops to 49.8 Hz in 0.25 s,

which is above the allowable ROCOF limit, showing the superior performance of the SMES in the frequency regulation when compared with that from the supercapacitor.

3.6. Determination of the Required Reserved Power

In Section 3.3, the suboptimal power point tracking strategy with artificial inertia support has been discussed to reserve a power to charge the SMES. A SMES has the capability to support significant power. However, in a small RAPS system, the full power capacity is not required. But, the power reserve should be enough to support the worst load fluctuation.

However, due to the intermittent nature of the wind velocity and the resulting unreliable power reserve, this SOPPT strategy is not the best solution to meet the sudden change in power demand. Also, the mechanical stress caused by the sudden torque increase is extremely detrimental to the drive train.

The frequent mechanical stress will increase the maintenance expenses of the mechanical counterparts. The frequency excursions are very common in a RAPS system since the system resilience is low in a small system, unlike that in a large grid. Therefore, it is mandatory to design a resilient frequency regulation control system to ensure the system reliability. A high temperature SMES based frequency regulation strategy has been proposed in this chapter. In this strategy, the SMES charging power, P_{ch} is supplied from the reserved power, P_{res} due to suboptimal power point tracking. But, continuously operating the wind turbine away from the MPP will cause significant stress as mentioned earlier. Also, a continuous operation in the suboptimal point might cause secondary frequency event. Therefore, it is necessary to predict how much reserved power in the SMES might be sufficient and when it would be needed. It can be predicted from the previously recorded load profiles of different households in a RAPS system, which could be a large number of data. Classifying load patterns and find the relevant load profile could be very burdensome and inefficient. To solve this, a dimensionality reduction is required and SAX is a good solution for this problem.

In the RAPS system shown in Fig. 3.11, there are three loads which three different households. To choose the appropriate amount of reserved power, the load profiles of those household need to be analyzed. The time series of a 24 hour load profile with a 5 min interval

for three consecutive days have been taken for analysis. They are collected from the Amy Close suburb of NSW state of Australia. These time series are converted to the PAA (piecewise aggregate approximation) coefficients. As per Gaussian distribution, the PAA coefficients will be converted to characters which will significantly reduce the dimensionality while preserving the essential features of the time series.

If we consider each time series data, t of length n = 2880 (30 sec interval data for 24 hours); t = t_1, t_2, t_3…... t_n. After normalizing the time series, it will be converted to a w-dimensional time series, l such that W<<n, using Piecewise Aggregate Approximation (PAA). The value of W is dependent on the word size. With the high value of word size the W will be higher. Although the resolution will be better, it will cause more computational burden. In this case, we consider the word size of 8. The formula for calculating PAA is as below:

$$t_i = \frac{w}{n} \sum_{k=\frac{n}{w}(i-1)+1}^{\frac{n}{w}i} S_k$$

(3.19)

If the PAA series is expected to be symbolized using k-alphabet, then the Gaussian distributed curve has to be divided into k-1 breakpoints. In this case, the alphabet size is considered to be 6. Therefore, there will be 5 levels of Gaussian distribution.

Any value equal or less than the 1st level will be assigned 'a', equal or less than the 2nd level will be assigned 'b', equal or less than the 3rd level will be assigned 'c', and so on. There is a detailed discussion on this with illustration in Section 2.5 The SAX strings of the time series for the three days are shown in Table 3.4. Instead of 2880 data, the time series has been interpreted with only 8 data string.

Table 3.4

SAX character strings

Day	Load 1					Load 2					Load 3				
1	'b'	'a'	'd'	'c'	'b'	'a'	'e'	'e'	'd'	'c'	'c'	'a'	'a'	'b'	'e'
	'c'	'f'	'f'			'e'	'd'	'a'			'f'	'e'	'f'		
2	'b'	'a'	'b'	'c'	'd'	'a'	'e'	'e'	'd'	'c'	'b'	'a'	'b'	'e'	'e'
	'd'	'f'	'f'			'e'	'd'	'a'			'f'	'e'	'd'		
3	'a'	'a'	'd'	'c'	'c'	'a'	'e'	'e'	'd'	'c'	'b'	'b'	'c'	'b'	'e'
	'e'	'f'	'e'			'e'	'd'	'a'			'f'	'd'	'c'		
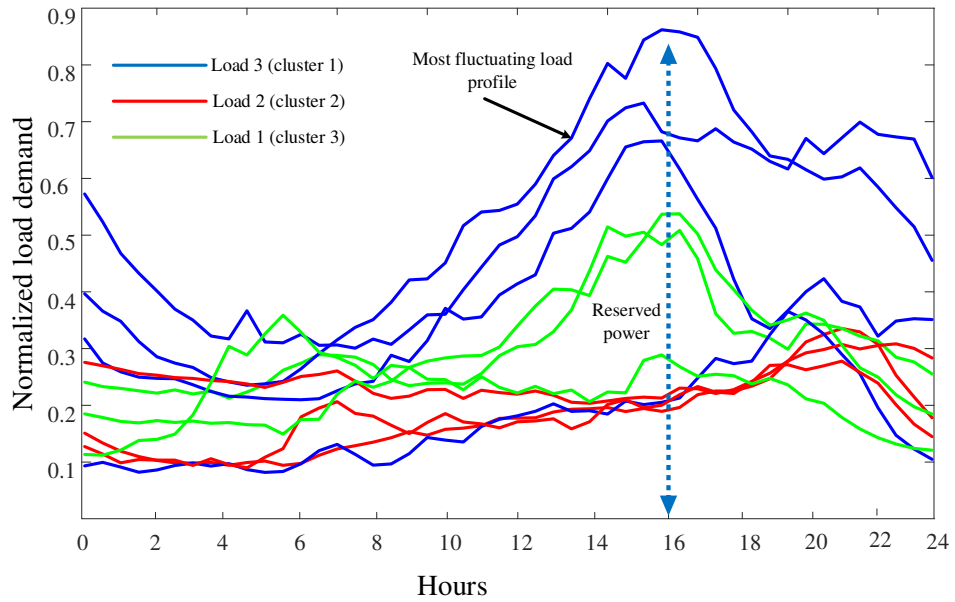
Fig. 3.17. Discriminated wind profile with SAX and clustering algorithm

Now the load profiles represented by SAX strings will be classified according to their characteristics in order to identify the most fluctuating load profile using clustering algorithm. The K-means clustering has been used in this experiment to classify the load profiles. It has been observed that the cluster 1, which are shown in blue, shows the most

fluctuating characteristic and a significant increase in demand from 2 to 6 PM. The cluster 1 belongs to load 3. After that, brute force algorithm has been implemented for the load 3 cluster to find the most anomalous load profile among load 3 profiles. The profile with the highest Euclidean distance within the cluster is the most anomalous one and its peak demand will be the amount of the required reserved power.

The peak demand of this profile will be taken as a reference for the power reserve in the wind turbine. It also shows that, the peak demand continues from 2 pm to 6 pm, which means during that time period, the PMSG based WECS will operate along a SOPPT curve so that there is a power reserve of the same amount. Therefore, in the worst case scenario, if there is a sudden demand of the peak load, the WECS will be able to meet the generation demand gap through SMES.

3.7. Summary

In this chapter, the frequency response of a PMSG based wind turbine in an optimally designed standalone power system has been investigated, and a control strategy has been proposed to improve the frequency response capability of WECS using an integrated SMES module. The SMES has provided better performance for frequency recovery due to its very fast response capability and its ability to relieve torque stress.

There are however some limitations with the SMES. Since the energy density in the SMES is very small, it can only operate for a short time. This has been solved by including a high pass filter in the dc chopper control for the SMES to make sure that the SMES is only activated for fast variations. Also, a SAX algorithm based strategy has been proposed to find the optimum amount of power storage in SMES. One of the major drawbacks of the SMES is that it is very expensive. However, with the evolvement of technology it is expected that the cost will become reasonable.

Chapter 4

Improving the Thermal Performance of Rotor-side Converter of Doubly-fed Induction Generator Wind Turbine while Operating around Synchronous Speed

Foreword

For power electronic converter-based variable speed DFIG, the operation near the synchronous speed (usually at a very low slip) can cause the rotor side converter to become significantly stressed due to the increased temperature fluctuation, which can lead to a reduced reliability over time. This chapter shows how the semiconductor junction temperatures and power losses of a DFIG can be calculated when operated near the synchronous speed. While the thermal stress can be reduced by decreasing the switching frequency and the converter current, this paper proposes a current derating technique based on the reactive support sharing strategy to reduce the thermal stress on the rotor side converter. This chapter also proposes a switching control technique to deal with the tradeoff between the pulse width modulation (PWM) harmonics and the semiconductor junction temperature. A low switching frequency can cause harmonics and torsional vibration, whereas a higher switching frequency can cause elevated thermal cycling. A reference point is determined so that the parameters e.g. the junction temperature and the total harmonic distortion (THD) follows this reference point. Also, a coordinated switching control scheme with rotor current derating is presented to effectively reduce the conductor thermal stress without compromising the performance reliability.

4.1. Background

Wind energy has become one of the major renewable sources of power with the advancement of power electronics technology. However, the variable nature of the wind

energy sources (in terms of the real power, reactive power, output voltage, and frequency) is a major challenge. A power conditioning circuit using power converters is generally used in a wind turbine generator system to adjust the fundamental parameters. The doubly-fed induction generator (DFIG) is currently the most popular wind energy conversion system using back-to-back power electronic converters. One of the converters is the rotor side converter (RSC) and the other is the grid side converter (GSC) as shown in the simplified DFIG topology shown in Fig. 4.1.
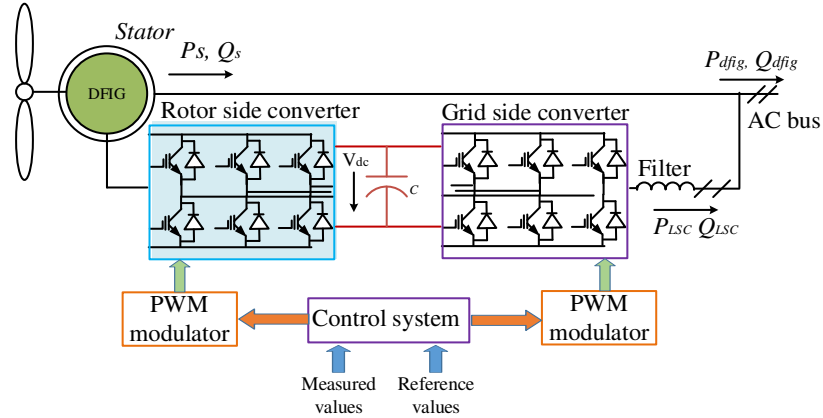
Fig. 4.1. DFIG based wind energy conversion system (simplified topology).

Although, the lifetime of a DFIG-based (wind energy conversion system (WECS) is generally quite high, the poor reliability of the power electronic converters is one of the factors that might result in frequent maintenance. Several reliability tests have been performed by power converter manufacturers and the results show that the most common factors that can affect the lifetime of the converters are the fluctuations in the junction temperature, the mean junction temperature, and the semiconductor "ON" time [37]. When the wind generator is operated near the synchronous speed (usually at a very low slip), the RSC experiences a significant fluctuation in the junction temperature that can cause increased power loss, resulting in a significantly reduced lifespan. The focus of this paper is how to mitigate the poor reliability of the rotor side converter due to the fluctuation in the junction temperature.

Several research papers have been reported this issue and proposed mitigation techniques. Most cases, the authors focused on the steady-state small thermal cycles and proposed the use of reduction of switching frequency as a mitigation technique. Because the switching loss constitutes the bigger portion of the total loss, reducing the switching frequency decreases the mean junction temperature as well as the temperature swings. But this can result

in increasing the harmonic problem that will need to be mitigated by improved filtering technique. References [92], [96] focus on the high thermal cycling due to the low-slip operation of the DFIG. In [3], a strategy is proposed to avoid the rotor speed operating in the low slip region with a rapid change in the rotor speed, but this can cause a mechanical stress on the drive train. The paper in [92] also proposes the use of a suboptimal power point tracking strategy as another feasible solution. In this technique, the DFIG is operated along a fixed curve away from the synchronous speed. But this will require a reliable operation of the anemometer to ensure that it moves back to its maximum power point tracking operation in time. In [45], it is proposed that the DFIG is converted to simple induction generator mode by activating the crowbar, if the rotor speed approaches the low-slip region. However, this requires the same electromagnetic torque between the two modes during the transition or there would be a huge torque transient. So, the rotor speed needs to shift to the equivalent point between the two modes before transition. However, an accurate and an early prediction to determine the time it takes to reach the low-slip region needs to be performed in order to allow the controller sufficient time to change the rotor speed.

In this chapter, the thermal characteristics of the rotor side converter during the low-slip operation are studied and an effort is made to improve its thermal performance. A current derating technique based on an optimized reactive current sharing strategy is proposed to reduce the conduction loss of the semiconductors. Also, a switching frequency control technique is proposed, which can significantly reduce the switching loss without compromising the power quality or producing torsional stress in the drive-train.

The layout of this chapter is organized as follows. The thermal behavior of the power electronic converters around the synchronous speed are analyzed and evaluated in Section 4.2. The reactive current sharing strategy is discussed in Section 4.3. In Section 4.4, the switching frequency control scheme is described. An algorithm based on the coordinated approach of the converter current derating and the switching frequency control is presented with detailed simulation results in Section 4.5. An experimental validation of the proposed coordinated technique with reactive current sharing and switching frequency control scheme is carried out in Section 4.6 for a low-scale DFIG. Finally some conclusions are drawn in Section 4.7

4.2. Thermal Behavior at Synchronous Speed

4.2.1. Losses in Power Electronic Converters

There are typically two types of power loss in a power electronic semiconductor: (i) the switching loss and (ii) the conduction loss. The switching loss is incurred due to the frequent switching of the power electronic switches, which is dependent on the carrier frequency. On the other hand, the conduction loss is dependent on the current magnitude. If the converter handles higher current, the conduction loss becomes higher.

In the case of the switching energy loss of an IGBT and a diode, the formulas are given by (4.2) and (4.3) [85].

$$E_{swIGBT}(i, V_{DC}, T_j) = (E_{on} + E_{off}) \frac{i}{i_{ref}\left(\dfrac{V_{DC}}{V_{ref}}\right)^{Kv}\left[1 + c_{sw}(T_j - T_{ref})\right]} \tag{4.2}$$

$$E_{swDiode}(i, V_{DC}, T_j) = Err\left(\frac{i}{i_{ref}}\right)^{Ki}\left(\frac{V_{DC}}{V_{ref}}\right)^{Kv}\left[1 + c_{rr}(T_j - T_{ref})\right] \tag{4.3}$$

Equation (4.4) and (4.5) are the expressions for determining the conduction energy loss of the IGBT and freewheeling diode.

$$E_{condIGBT}(I_T, T_j) = \int_o^T (i_T(t)(V_{ceo}(T_j) + r_{ce}(T_j)i_T(t))dt \tag{4.4}$$

$$E_{condDiode}(I_D, T_j) = \int_o^T (i_D(t)(V_{fo}(T_j) + r_f(T_j)i_D(t))dt \tag{4.5}$$

Equations (4.2)–(4.5) show that the energy losses are a function of the junction temperature. Hence, with an increasing junction temperature, the conduction and switching loss increase even if the switching frequency and current magnitudes are kept unchanged.

4.2.2. Thermal model of rotor side converter

The thermal network of a half bridge of RSC is shown in Fig. 4.2. Each IGBT and diode are represented by the heat source given by the energy losses and the thermal impedance,

Z_{thjc}. The thermal impedance from the IGBT and the diode to the heatsink and are assumed to be equal and represented by Z_{thca}. This two-cell thermal network is based on the thermal capacitances (case and heat sink) and resistances (case-to-sink and sink-to-ambient).
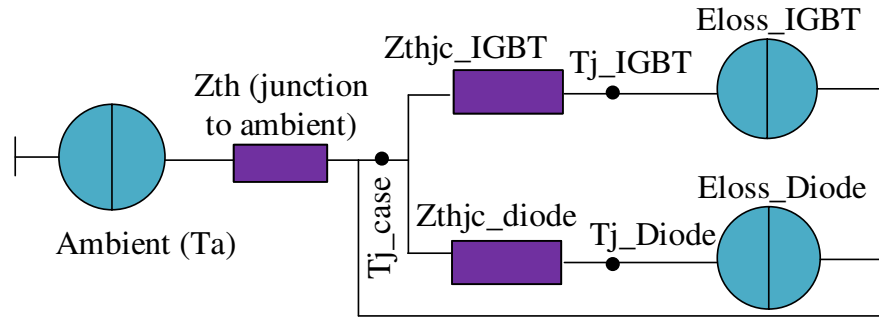
Fig. 4.2. A two cell thermal network model of a half-bridge IGBT and diode module.

4.2.3. Power Loss and Junction Temperature Measurement Model

For the quantification of the thermal characteristics, i.e. different power losses, case temperature and junction temperature, the model shown in Fig. 3 is used. There are separate power loss calculation blocks for the IGBT and the diode. The current and voltage measurements of the IGBT and diode, and the respective junction temperature are fed into respective blocks, which calculate the switching and conduction losses according to (4.2)–(4.5).

There is another block that receives the power loss information for the IGBT and diode and calculates the total thermal output and the junction temperatures for the IGBT and diode respectively. These are dependent on the efficiency of the heat sink and ambient temperature. This is actually the thermal network as shown in a simplified form in Fig. 4.2. The state space models are used in this block. The coefficients of the state space models are dependent on the thermal resistances and capacitances of the thermal network. If the thermal output is high, the case temperature will be lower. This will affect the junction temperature of the IGBT and diode as well. This junction temperature is again fed back into the diode and IGBT loss calculation modules.

57
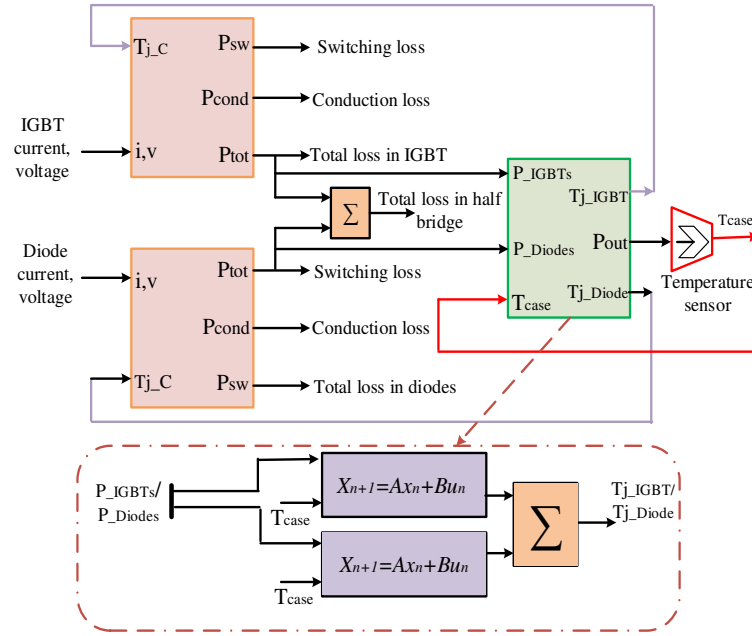
Fig. 4.3. Junction temperature and power loss calculation module

4.2.4. *Thermal cycling of power electronic converter*

For verification purposes, a 2-level PWM generator is used to generate the gate pulses for the inverters. The PWM signals vary the duty cycle to generate the appropriate gate pulses using the SPWM technique. In this modulation technique, for a fundamental half cycle, the switch on time, t_{on} is supposed to be higher. Whereas, for the next half cycle, it should be lower. Therefore, even with the same switching frequency, the duty cycle changes. Now, if the rotor current frequency becomes very small, the period of every half cycle becomes very high. It means there will be more "ON" time per unit time as the half cycles are getting longer, assuming the carrier frequency is kept unchanged. Fig. 4 shows the relationship between T_{on} and the thermal impedance. The thermal impedance increases very fast with the increasing t_{on} time [7]. The higher thermal impedance leads to a higher junction temperature.

$$Z_{thjc} = \sum_{k=1}^{n} R_{thk} \frac{1-\exp\left(\dfrac{-t_{on}}{\tau_{thk}}\right)}{1+\exp\left(\dfrac{-T_s}{\tau_{thk}}\right)}$$
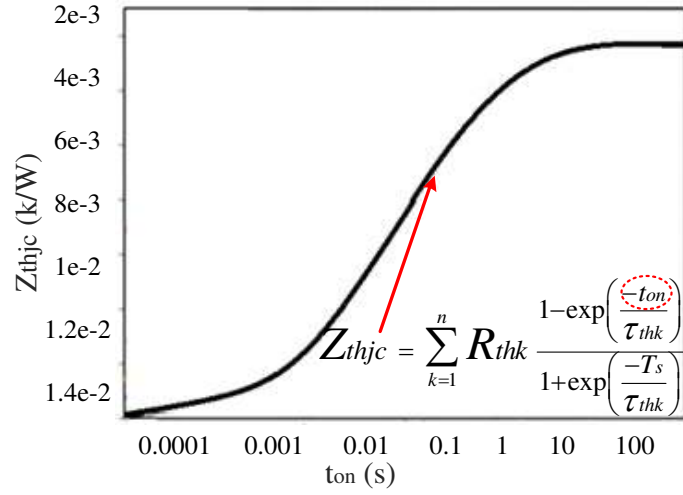
Fig. 4.4. Relation between thermal impedance and t_{on}.

As mentioned earlier, larger half cycles with longer "ON" time will increase the thermal impedance and consequently, will increase the junction temperature. On top of that, the increasing energy loss exacerbates the junction temperature as the thermal impedance between the junction becomes higher with the increased "ON" time.

4.2.5. *Observation of the thermal behavior of the rotor side converter*

In this section the thermal behavior of the RSC is observed. In a DFIG, the RSC enables the wind turbine to have a specified magnitude and a constant frequency voltage at the stator terminal by inducing a rotor voltage with a slip frequency ($f_r = sf_e$) even when the turbine is operating at variable speeds. Therefore, the angular frequency of the rotor current becomes very small when the rotor speed approaches the synchronous speed.

A lower frequency causes much longer temperature rises and falls resulting in a larger peak-to-peak temperature swings in the semiconductor junctions. The life-time of the switching devices is proportionally decreased with an increase in the amplitude of junction temperature (T_j) fluctuation [8]. The semiconductors in the RSC of a DFIG become significantly stressed around the synchronous speed, and it is important to investigate and propose strategies to overcome this issue so that the reliability of the system is not compromised.

The simulation of a DFIG with the thermal model of the RSC has been carried out using the MATLAB/Simulink simulation software and the results are shown in Fig. 4.5. Table 4.1

shows the thermal network parameter values, Table 4.2 shows the machine parameters, and Table III shows the typical current ratings of the test DFIG.
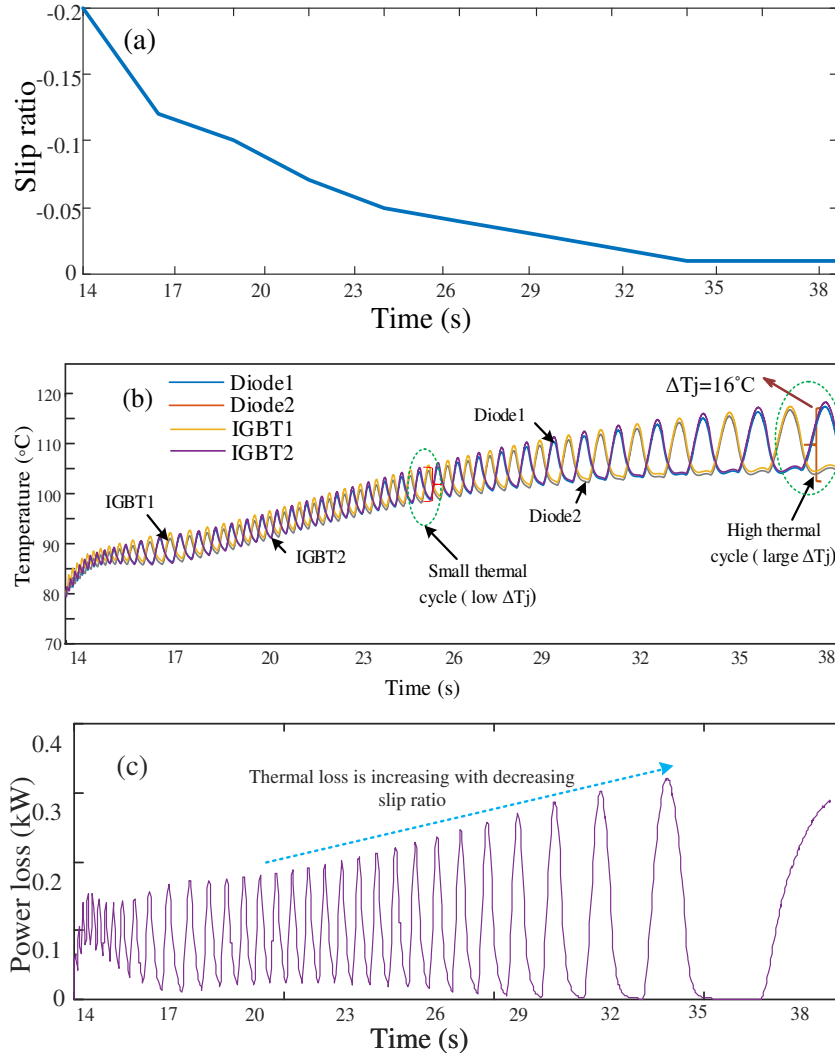
Fig. 4.5. (a) Rotor speed reaching synchronous speed; (b) Semiconductors junction temperatures with increasing magnitude; and (c) Increasing converter power loss.

Fig. 4.5(a) shows the turbine operates initially with a 20% slip ratio and the slip is slowly reduced until it approaches the dead band (the low slip range). Fig. 5(b) shows that the frequency of the rotor current becomes significantly small as the rotor speed approaches the synchronous speed. In this study, the SEMIKRON IGBT module SKiiP 2013 GB172-4DW V3 is used for thermal analysis. The Cauer network is used in this paper to estimate the

junction temperature as previously described in Fig. 4.2. The case-to-sink and case-to-ambient thermal resistance is 0.02 and 0.072 K/W, respectively.

As mentioned earlier, with the decreasing rotor current frequency, a larger peak-to-peak temperature swing occurs along with a significant increase in its maximum temperature. In Fig. 5(c), the envelope of the temperature curve is increasing as the frequency drops which implies larger thermal cycles. Fig. 5(d) shows that the total power loss increases as the rotor speed drops.

TABLE 4.1

PARAMETER VALUES

Parameter	Value
Ambient temperature	40∘C
Case-to-sink thermal resistance	0.02 k/W
Case-to-ambient thermal resistance	0.072 k/W
Rated switching frequency	1.5 kHz
System frequency	50 Hz

(Over excitation mode with Q=0.4 pu)

TABLE 4.2

DFIG PARAMETER VALUES (SIMULINK MODEL)

Parameter	Value
Turbine inertia constant	4.32 s
Stator terminal voltage	400 V
DC bus voltage	800 V
X_m	2.3Ω
R_s	0.023Ω
X_s	0.18 Ω
R_r	0.016 Ω
X_r	0.16 Ω

TABLE 4.3

TYPICAL CURRENT RATINGS

Parameter	Value
Stator current	0.96 pu
RSC current	1.11 pu
GSC current	0.21u

4.3. Proposed Reactive Power Flow Control for Deratng the Rotor Current Magnitude

The conduction loss of a power electronic converter can be deduced from (4) and (5). Fig. 1 shows the direction of the power flow from the grid side converter, the stator and the rotor. The steady state equivalent circuit of the DFIG is shown in Fig. 4.6. The reactive current support is provided by both the stator and grid side converter.
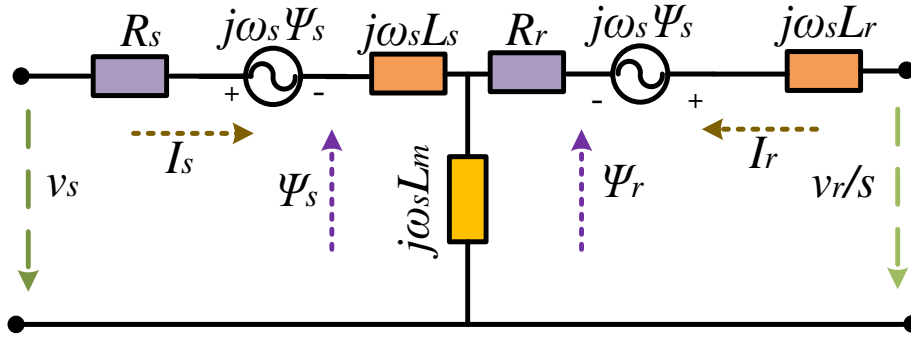
Fig. 4.6. Equivalent circuit of DFIG

4.3.1. Reactive current support breakdown for DFIG

The formulae for the total active and reactive power support from the DFIG are shown in (4.6)–(4.7).

$$P_{dfig} = \text{Re}\left\{\overline{v_s}\,conj(\overline{I_s})\right\} + \text{Re}\left\{\overline{v_{gsc}}\,conj(\overline{I_{gsc}})\right\} \tag{4.6}$$

$$q_{dfig} = \text{Im}\left\{\overline{v_s}\,conj(\overline{I_s})\right\} + \text{Im}\left\{\overline{v_{gsc}}\,conj(\overline{I_{gsc}})\right\} \tag{4.7}$$

Fig. 4.7 shows the phasor diagram of the stator voltage and current in the sub-synchronous and super-synchronous mode. It shows that in the super-synchronous mode, the rotor voltage is almost in the opposite direction to the stator voltage. Also, the rotor current is lagging the rotor voltage indicating that the rotor is supplying an active current to the stator. But, in the sub-synchronous mode, the rotor current is lagging the rotor voltage by less than 90 degree which means it absorbs both the active and reactive current.
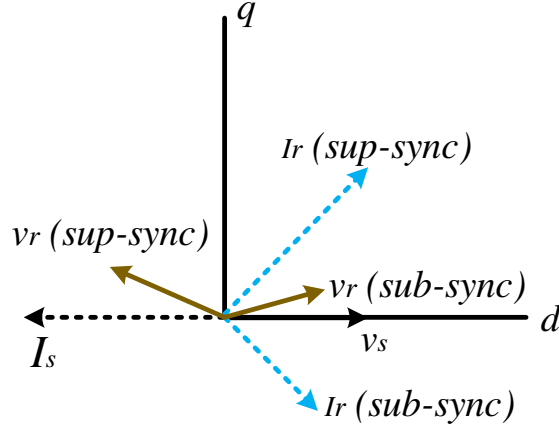
Fig. 4.7. Phasor diagram of the rotor and stator voltage and current.

If the direction of the stator voltage is taken as the reference, then the expression for the stator current in terms of the rotor current is given in (4.8). Decomposing (4.8), the imaginary part of the rotor current can be expressed in terms of the stator voltage and the stator reactive current as shown in (4.9).

$$\overline{I'_r} = \frac{L_s}{L_m} I_{ds} + j\,\text{sgn}(s).\left(-\frac{v_{ds}}{L_m} - \frac{L_s}{L_m} I_{qs} \right)$$
(4.8)

$$\overline{I'_{qr}} = \text{sgn}(s).\left(-\frac{v_{ds}}{L_m} - \frac{L_s}{L_m} I_{qs} \right)$$
(4.9)

4.3.2. *Proposed reactive current control scheme for improving the conduction loss in the RSC*

The grid power is supplied both by the stator and the grid side converter. However, usually the GSC is controlled to be operated with unity power factor mode, which means mainly the stator is responsible for the reactive power support. The stator active and reactive power support is maintained by controlling the RSC current. Since, the RSC becomes significantly stressed when operated near the synchronous speed, it is proposed to ease the burden on the

64

RSC by reducing the reactive power support from stator. However, the modern grid codes are quite stringent with the reactive power support capability. To comply with the grid code and reducing the burden on the RSC at the same time, the reactive power support can be shared by the GSC and the stator.

Fig. 4.8 represents the Irish grid code which is used as the reference grid code in this paper. Since, it is expected that the DFIG will fulfill the minimum requirement of the reactive current grid code, the rotor current needs to be controlled so that the grid code is satisfied. However, the reactive current support from the stator needs to be derated to reduce the thermal stress on the RSC.
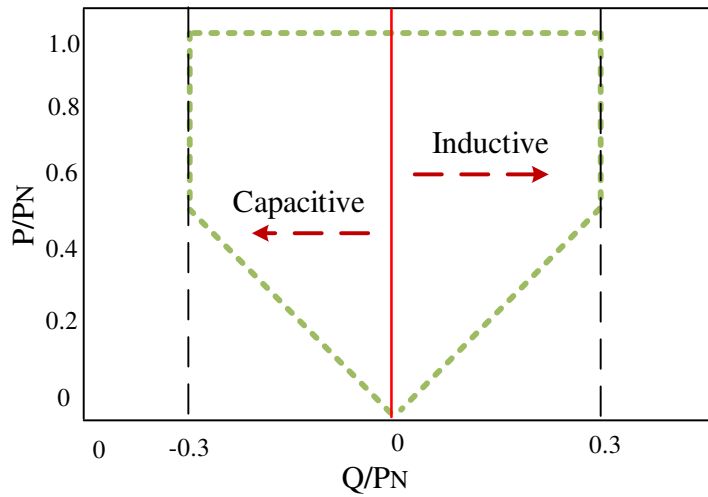
Fig. 4.8. Irish grid code. [9]

The active and reactive current capability curve of the DFIG is shown in Fig. 9. This curve makes sure that converter operation must not cross the maximum limit which can be damaging.
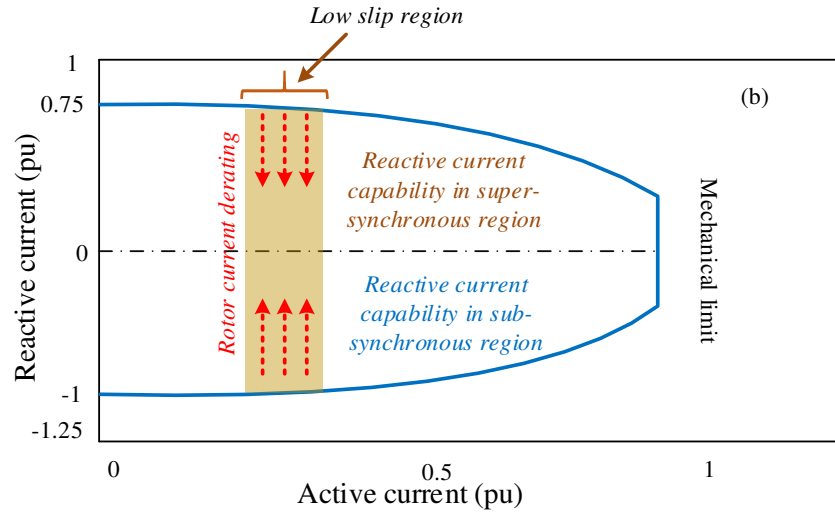
Fig. 4.9. Active and reactive current capability of DFIG.
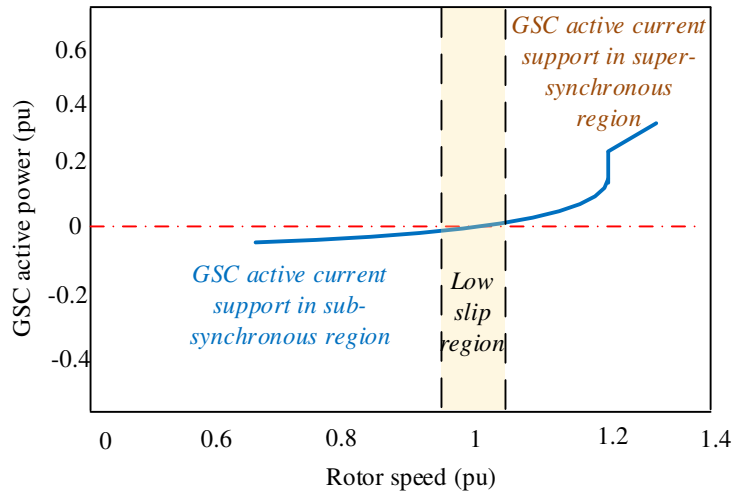
Fig. 4.10. GSC active power capablity with slip ratio.

Fig. 4.10 shows the active power capability curve of the grid side converter (GSC) with respect to rotor speed. Since the GSC supplies the slip power to the rotor, the GSC always needs to operate in active current priority. During a high speed condition, the reactive current capability of GSC is very low, since the active current is very high. Fig. 10 shows that the GSC active power capability is nearly zero during the sycnhronous operation whereas, its maximum active power capability is 0.2 pu at rated speed. This 0.2 p.u capability can be used for reactive current support without affecting the slip power.

For the given DFIG whose parameters are shown in Table 4.1, the maximum active current support from the DFIG is 0.25 pu. From the Irish grid code in Fig. 4.8, it can be concluded that at 0.25 pu active power capacity, the minimum reactive current support capability should be 0.3 pu, and 0.2 pu of which can be supported by the GSC alone. The stator can support the rest of the reactive power by controlling the rotor q-current, but this should be enough to drag the junction temperature below its threshold. Even if it does not, it will significantly improve the thermal performance of the rotor side converter without compromising the grid codes or the DFIG regular performance.

4.3.3. Reactive current controller to implement the proposed scheme

Since at sysnchronous speed, the GSC can avail its fully rated current for reactive current capability, the initial reactive current reference in the GSC is taken as the requirement at the point-of-common-coupling. However, it becomes limited by the minimum grid code. A 2-D look up table is utilized for this. However, its magnitude is also limited by the maximum rated current of the GSC. If the GSC cannot support the full grid requirement, the rest of the reactive current requirrement is expected to be supported by the stator and this is taken as the reference for the staor current support. This stator reactive current reference is then converted to the rotor current reference. The error signal with respect to both the GSC and RSC q-current reference is fed into PI controller to generate the reference voltage signal that would be generated by the PWM modulator as shown in Fig. 4.11.

(a)

(b)
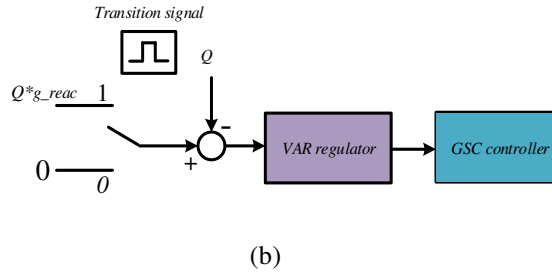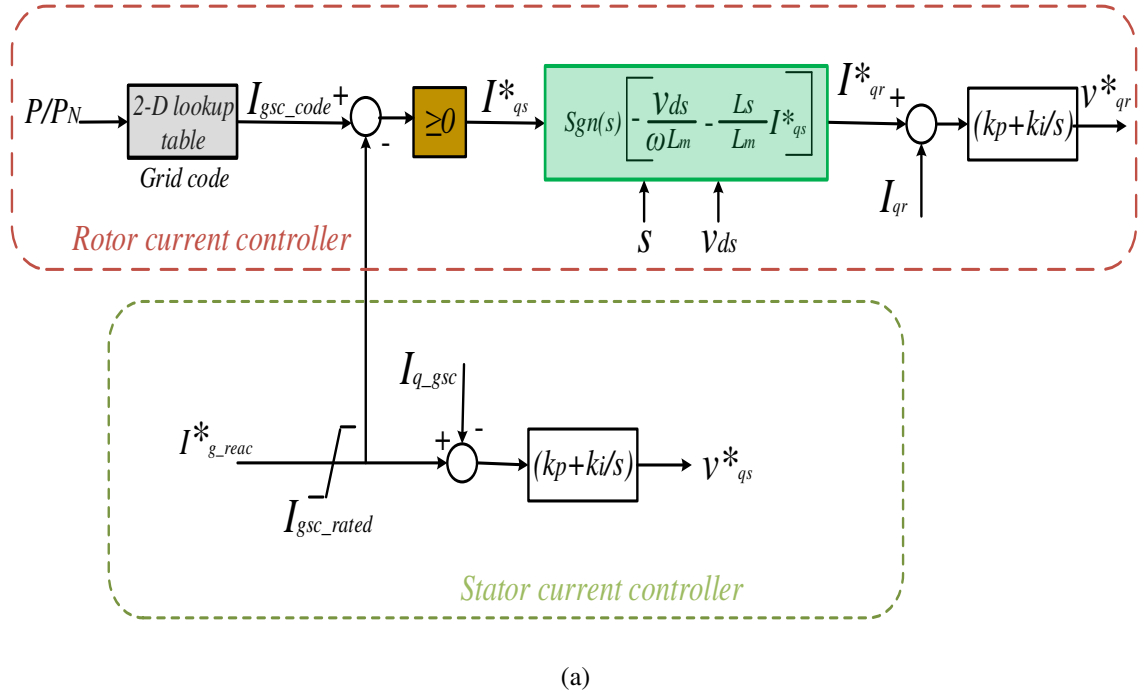
Fig. 4.11. Proposed reactive current controller: (a) shared control; (b) moving to shared mode from unity power factor mode.

It is to be noted that the DFIG is always operating in active current priority. Therefore, the active current is kept unchanged and only the reactive current is controlled. Generally, the GSC operates with unity power factor and the RSC controls the stator reactive current. However, if the DFIG reaches the synchronous speed operation, the controller shifts to the proposed control scheme as shown in Fig. 4.11(b). In this strategy the GSC does not operate with unity power factor anymore.

4.4. Proposed Switching Frequency Control Scheme

4.4.1. Relationship between the slip ratio and the THD with switching frequency

From the discussion in Section II, it is clear that the switching frequency or carrier frequency plays a vital role in the semiconductor losses. Reducing the switching frequency would reduce the junction temperature very quickly, however, it also can cause an increase in the current harmonics, the speed ripple and the pulsating torque, which significantly reduce the machine reliability [97], [98]. To comply with the IEC standard of power quality, the stator current harmonics must be strictly maintained.

With the reduced switching frequency, the dead-time harmonics reduce, but the higher order PWM harmonics increase very rapidly. The analytical expression for the harmonic current generated by one phase leg of the converter current is given below [97].

$$
\frac{I_{ac}}{2}\left\{
\begin{array}{l}
K_{0,1}\{\cos(4\pi f_0 t + \theta_0 + \beta) + \cos(\theta_0 - \beta)\} \\
+ \sum_{m=1}^{\infty}\sum_{n=-\infty}^{\infty} K_{m,n}\left\{
\begin{array}{l}
\cos(2\pi[mf_{cr} + (n+1) \\
f_0]t + m\theta_c + n\theta_0 + \beta) \\
+\cos(2\pi[mf_c + (n-1) \\
f_0]t + m\theta_c + n\theta_0 - \beta)
\end{array}
\right\}
\end{array}
\right\}
\tag{4.10}
$$

$$
M = \frac{\sqrt{\left(V_{ac} - 2\pi f_0 LI_{ac} \sin\beta\right)^2 + \left(2\pi f_0 LI_{ac}\cos\beta\right)^2}}{V_{dc}/2}
\tag{4.11}
$$

Where, I_{ac} is the amplitude of the fundamental components of the rotor current, f_c is the carrier frequency, θ_c is the carrier phase angle, f_0 is the fundamental frequency. $K_{m,n}$ is the amplitude of the harmonic component which is calculated from the Bessel function of the first kind J, which is shown in (4.14). From (4.14), it is evident that the value of this function is exponentially proportional to the value of q and M. M is the modulation depth and the definition of q is given in (15).

$$J_n(qM) = \sum_{m=0}^{\infty} \frac{(-1)^m}{m! \; (m+n+1)} \left(\frac{qM}{2}\right)^{2m+n}$$

(4.14)

$$q = \left(m + \frac{nf_0}{f_c}\right)\frac{2}{}$$

(4.15)

As mentioned earlier, the rotor current frequency, f_0, drops with the decreasing slip ratio. Therefore, it will make the f_0/f_c ratio smaller resulting in a significant reduction in the harmonic components amplitude according to (4.10), (4.14), and (4.15). Table 4.4 shows the effect the reduction of both the switching frequency and the slip ratio on the harmonic distortion of the stator current.

Table 4.4

Stator voltage THD with change in slip ratio and switching frequency

THD (%)	$S=-0.2$	$S=-0.1$	$S=-0.05$	$S=-0.01$
$f_s = 1.5\ kHz$	3.3	1.5	0.91	0.5
$f_s = 0.7\ kHz$	6.5	3.1	1.63	0.67
$f_s = 0.35\ kHz$	13.02	7.12	3.62	0.73

As shown in Table 4.4, the switching frequency at 350 Hz causes a very large harmonic distortion when the DFIG is operated in its rated speed, but the same switching frequency causes very minimal harmonic when it is operated around the synchronous speed. Fig.4.12 shows the variation of the THD with the slip ratio.
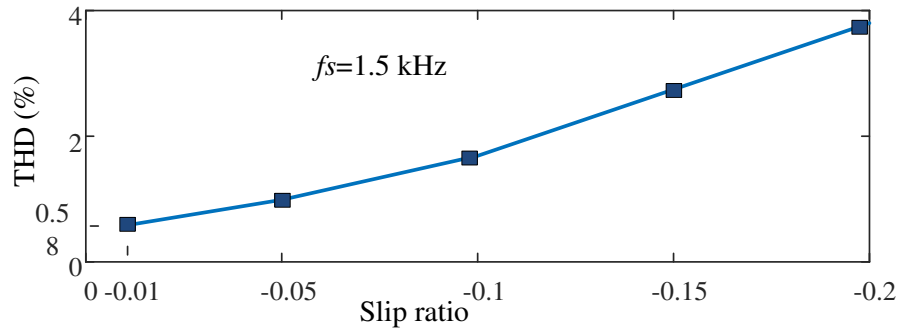
Fig. 4.12. Relation between slip ratio and THD

Table 4.4 and Fig. 4.12 show that with the same switching frequency, as the DFIG approaches the synchronous speed, the current harmonics reduce significantly. The rotor voltage frequency reduces as the slip ratio reduces. With the same carrier frequency, the number of the carrier pulse per reference voltage cycle significantly increases resulting in power quality improvement with the reduced slip ratio. It also provides the window of opportunity to reduce the switching frequency near the synchronous speed. This means that the switching frequency can be reduced till the THD of the stator current reaches the borderline of the IEC standard. However, this is not ideal as the power quality can be compromised along with the reduced reliability of the drive train due to the increased torque ripple. To minimize this, a new threshold is proposed in next section.

4.4.2. Determining thresholds for ensuring satisfactory operation

If the switching frequency is reduced in proportion to the rotor current frequency, the harmonic distortion does not increase significantly. If the harmonic distortion keeps getting higher, the reliability of both the converter and the drive train diminishes along with the power quality. However, if the switching frequency is reduced till the harmonic distortion reaches the value corresponding to the most available (or close to) wind velocity and with the rated PWM carrier frequency; the distortion can be restricted to a tolerable limit without compromising its normal performance. It is presumed that the wind profile of the test area follows the Weibull distribution and belongs to the IEC Class-I wind speed profile, which represents the high wind speed variation. Although, the wind profile can belong to other

71

classes, the Class-I wind profile is taken as the reference in this paper where the average wind speed is 10 m/s. Fig. 4.13 shows the probability distribution for the Class-I wind profile.
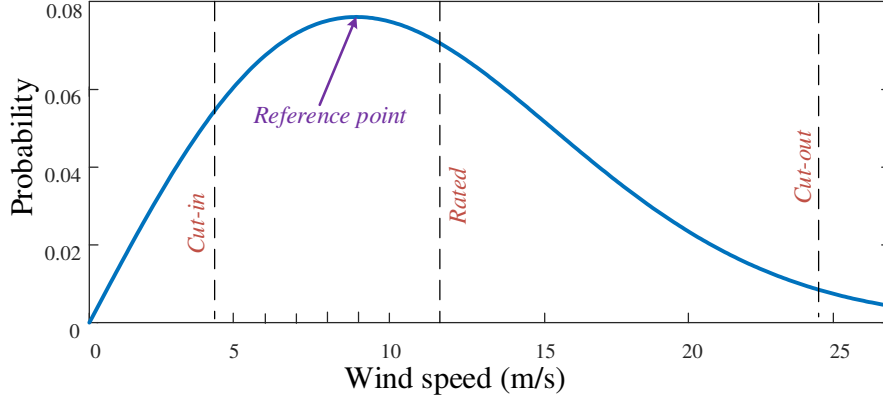
Fig. 4.13. Probability distribution of Class-I IEC wind speed profile [92].

The DFIG rotor rotates near the synchronous speed when the wind velocity reduces to 6 m/s. The cut-in wind velocity is 4 m/s and the cut-out wind velocity is 24 m/s. From the wind speed probability distribution in Fig. 13, the highest probable wind speed is 8.5 m/s. Also, the rotor speed with the MPPT control at this wind velocity is observed to be 1.08 pu. Therefore, this wind speed and consequently, 0.08 slip ratio is taken as the reference point. The stator voltage THD and the thermal cycles are measured at this point and considered as the threshold values. The THD and the junction temperature fluctuation of semiconductor are controlled so that they do not become higher than the threshold values. An algorithm is proposed in section V to limit those parameters within the specified limit.

4.5. Coordinated Control Algorithm with Switching Frequency and Rotor Current Derating

The flowchart of the algorithm is shown in Fig. 4.14. When the machine reaches the low-slip region ($0.98 < \omega_r < 1.02$), the DFIG moves to the optimized reactive current sharing control mode. After that, the junction temperature fluctuation, ΔT_j is compared with the threshold value. If ΔT_j is still higher than the reference, the switching frequency is reduced until ΔT_j reaches the reference threshold point. The threshold values are tabulated in Table V. While reducing the switching frequency, if the stator voltage THD rises to the threshold

value (1.9%), the process stops. The references for the THD and minimum grid reactive current requirement are given priority in this strategy. Although the aim of this algorithm is to control the junction temperature fluctuation below the reference value, the process stops if the THD reaches the maximum reference limit. Also, the minimum grid requirement of the reactive current is strictly maintained.
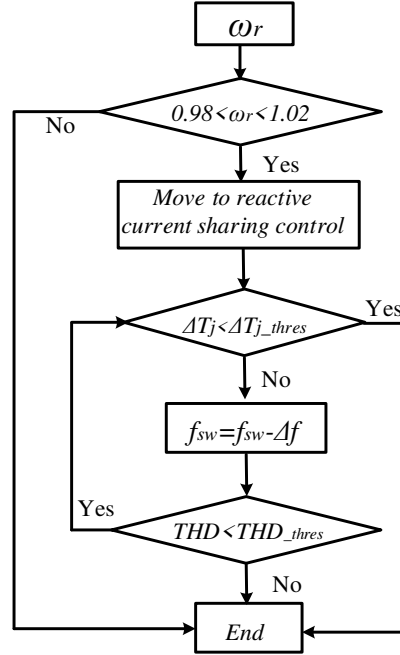
Fig. 4.14. Algorithm of proposed technique.

Fig 4.15(a) shows the change in the slip ratio with time and Fig. 4.15(b) shows the improvement in semiconductor junction temperature with the proposed strategy. As the DFIG approaches the synchronous frequency, the thermal cycle and the maximum temperature increases. In 38 sec, the rotor speed reaches 1.02 pu, which is considered to be the upper limit of the low-slip region. At that point, the DFIG is moved to the shared reactive current control mode. At 44 sec, the switching frequency is gradually reduced until the THD of the stator current, the maximum junction temperature and the temperature fluctuation is equal or below the threshold. By 50 sec, the THD reaches the threshold limit and the junction temperature fluctuation also reaches the lower value of the threshold. In this example, the slip ratio is maintained at constant 2% during the application of the proposed strategy. Practically,

however, the rotor speed may move out of the low-slip region due to the high fluctuating wind speed.

Fig. 4.16(b) shows that at the 38th sec, the junction temperature fluctuation was about 16°C. With the proposed method the junction temperature fluctuation, ΔT_j drops to 7°C. Also, the average temperature drops from 110°C to 104°C.
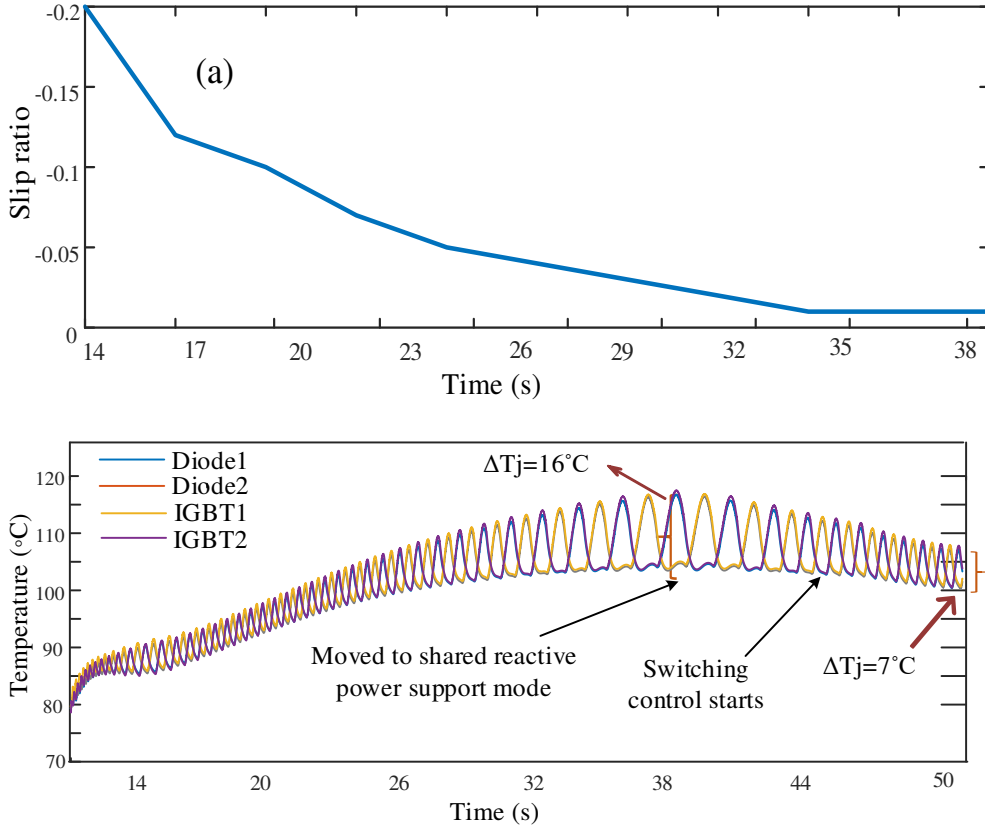
Fig. 4.15. Temperature reduction with proposed technique

TABLE 4.5

THRESHOLD VALUES

Reference wind velocity	8.5 m/s
THD_thres (at 8.5 m/s and MPPT)	1.9%
Junction temp fluctuation, ΔT_{j_thres} (at 8.5 m/s and MPPT)	7°C

Fig. 4.16 shows, the THD gradually reduces with the decreasing slip. However, at 44th second, as the switching frequency starts to reduce, the THD increases and it keeps increasing until it reaches the reference value.
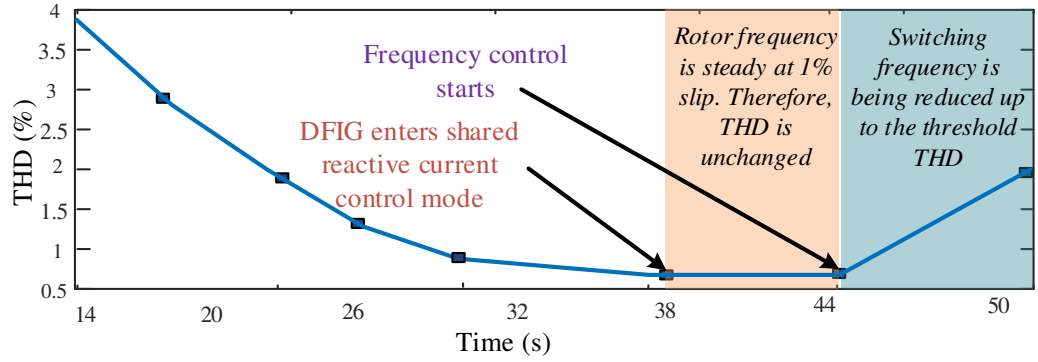
Fig. 4.16. Effect on stator current THD with the proposed technique

4.6. Experimental Validation of the Proposed Approach

The effectiveness of the proposed strategy has been demonstrated in the previous section through a detailed simulation. The proper quantification of the junction temperature, the associated power loss and the thermal analysis are not practically possible. However, some experimental results are provided in this section to prove the effectiveness of the proposed technique with a low-powered DFIG test rig. Fig. 4.17 shows the experimental setup (machine side) for validation of the proposed approach. The machine is a four-pole and doubly-fed induction generator (asynchronous generator). The RSC and the GSC are controlled with dSpace Microlab box. Two SEMITEACH IGBT blocks are used for the back-to-back converters.

(a)

(b)
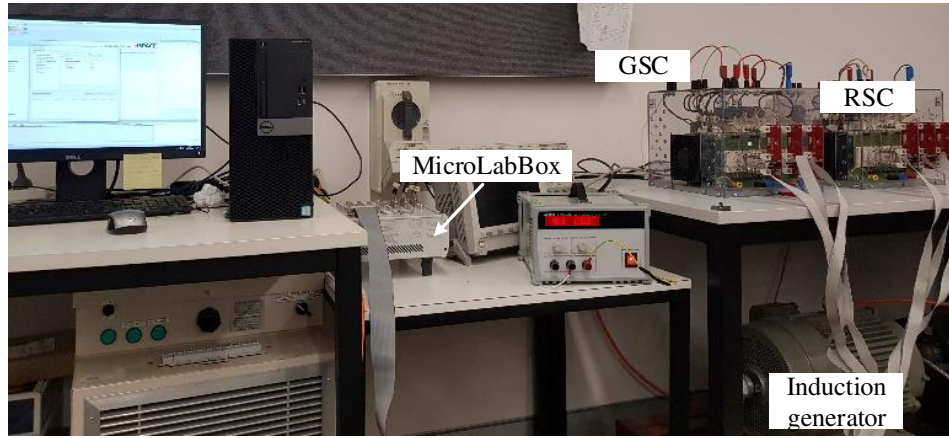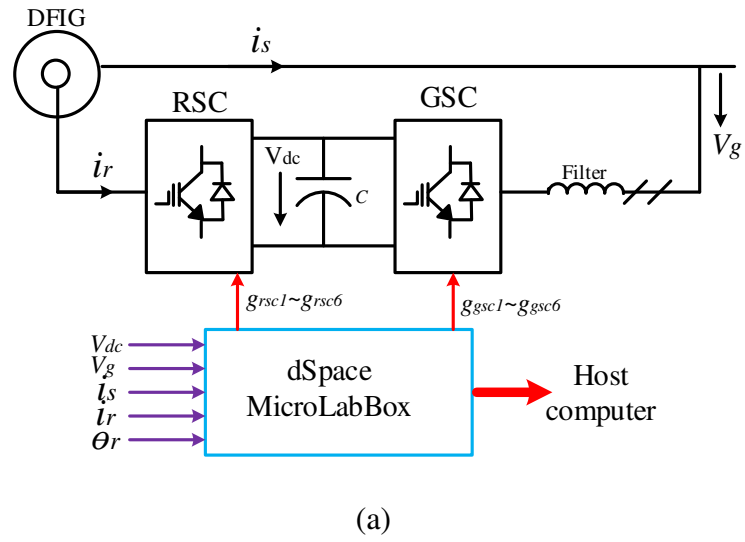
Fig. 4.17. Experimental setup (machine side) for validation of the proposed approach: (a) schematic diagram; (b) picture of the setup.

Table 4.6 shows the parameters for the experimental setup.

TABLE 4.6

TEST DFIG PARAMETER VALUES

Parameter	Value
Nominal voltage	415 V
Rated capacity	15 kW
Rated current	24.9 A
Nominal frequency	50 Hz
Slip range	-0.2–0.2
Semiteach module maximum switching frequency	10 kHz

As explained in Section 4.3, the GSC operates with unity power factor. However, when the machine enters the low-slip region, the GSC operation now moves to the reactive current sharing mode from the unity power factor mode as per Irish grid code (shown in Fig. 4.8), which effectively reduces the rotor current magnitude. Fig. 4.18 shows the reduction of the rotor current frequency with the decreased slip ratio.

(a)   (b)
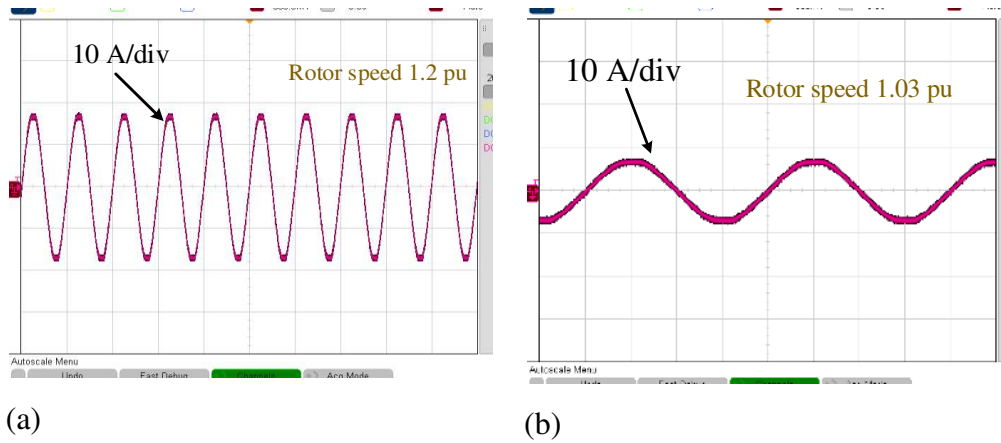
Fig. 4.18. The frequency of rotor current is changed with different rotor speed.

Since, the junction temperature fluctuation is not possible to be measured with thermal camera, instead the junction temperature fluctuation (which is more appropriate) and the mean junction temperature are considered here for measurement. In this study, 1700 rpm is chosen to be the reference speed. Therefore, the THD and the mean junction temperature at this reference speed are taken as the threshold. The switching frequency is reduced until the mean junction temperature goes below the threshold temperature. Fig. 4.19 shows the effect on the IGBT temperature with the proposed strategy. The thermal images are captured using the TESTO 885 IR Camera.

(a)

(b)

(c)
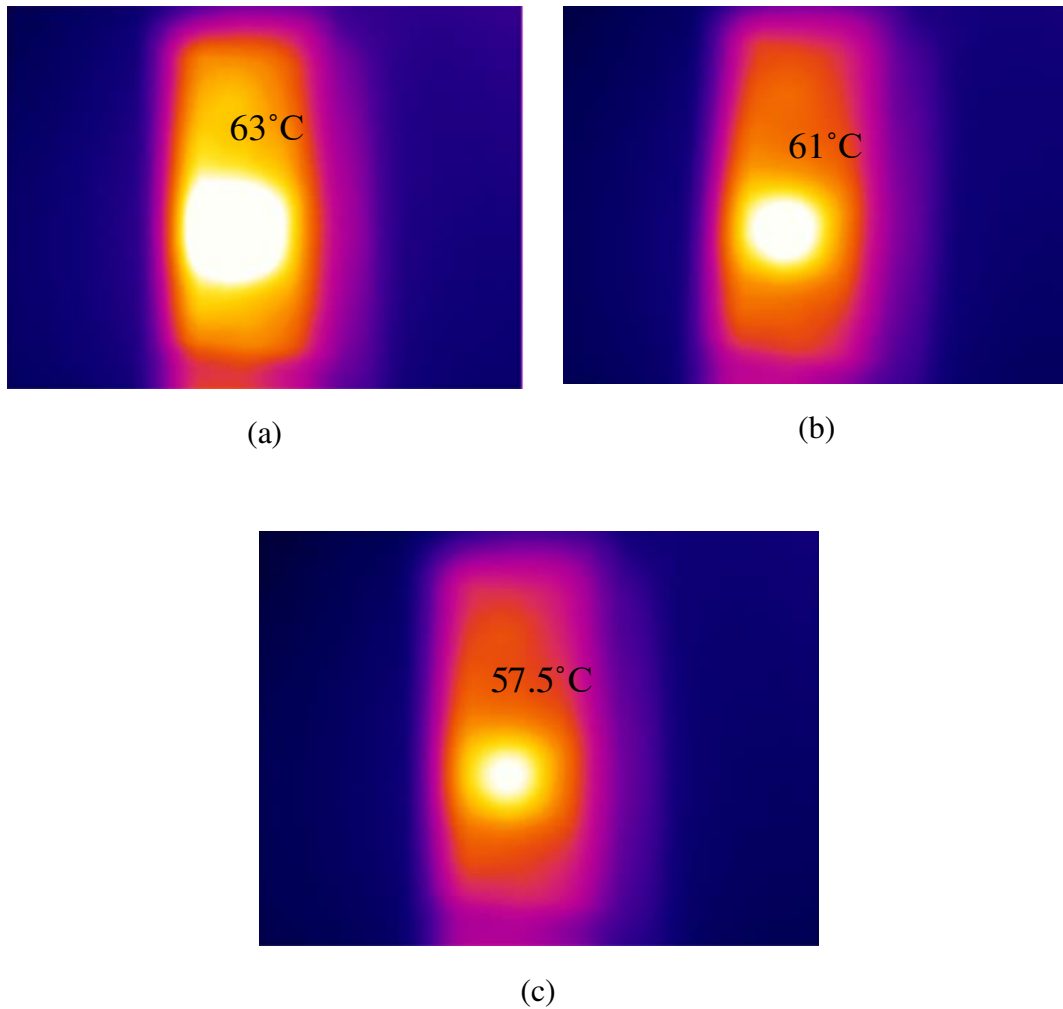
Fig. 4.19. The effect on IGBT temperature observed with "TESTO 885 Thermal Imager": (a) at synchronous speed at unchanged switching frequency and stator power support; (b) IGBT temperature with shared reactive current mode; (c) IGBT temperature with both reduced switching frequency and reactive current sharing.

Fig. 4.19(a) shows the temperature when the rotor operates at synchronous speed with the rated switching frequency and the same power (active and reactive) support from the stator side. Fig. 4.19(b) shows the reduced temperature after the GSC shares the reactive current. Finally, the switching frequency control technique shows more reduction in the temperature of the IGBT, which is below the threshold temperature as shown in Fig. 4.19(c).

4.7. SUMMARY

The elevated junction temperature fluctuation can greatly diminish the life time of the converters. In this paper, the junction temperature and all power losses have been quantified and their response to the rotor speed fluctuation has been observed. Also, a coordinated control strategy based on the switching control and the derating of the converter current has been verified, and shown to significantly reduce the maximum junction temperature during the low slip operation without imposing more harmonic distortion or compromising the system performance. The strategy improves the life cycle of the rotor side converter by several times.

Chapter 5

Shunt Active dc Filter to Reduce the dc-Link Ripple Current Caused by Power Converters to Improve the Lifetime of Aluminium Electrolytic Capacitor

Foreword

Electrolytic capacitors are very popular for use in the dc-link of the power electronics converters, particularly in applications in renewable energy systems. However, the life expectancy and reliability of the electrolytic capacitors can be severely affected by the ripple in their dc current causing an increase in thermal stresses. Further, the switching of power electronics and the presence of harmonic components in the capacitor dc current can increase the ripple current worsening the life expectancy of the electrolytic capacitor. This paper proposes the use of a novel shunt active filter to maintain the dc current in the capacitor to be almost constant and hence the life of the electrolytic capacitor can be prolonged. The proposed novel filter can reduce the ripple current irrespective of the frequency spectrum. The paper presents and discusses the design and the operating principle of the proposed active filter. The paper also presents the results from extensive simulation studies using a model developed in MATLAB/Simulink and from laboratory experiments that demonstrate and validate the effectiveness of the proposed filtering technique.

5.1. Background

Renewable energy-based energy conversion systems especially, wind and solar systems widely utilize power electronic converters for controlling their ac power outputs. They are also utilized to achieve unity power factor and high efficiency [93]. The aluminium

electrolytic capacitors are the most popular choice for use in the dc-link to support the power electronic converters. The performance of an aluminium electrolytic capacitor is highly dependent on the voltage level, frequency and core temperature. However, the equivalent series resistance (ESR) of the electrolytic capacitor increases due to the aging process caused by the evaporation of electrolytic liquid resulting in the rise in ESR [47]. The power electronic converter connected to the electrolytic capacitor may further inject harmonics and current ripple in the dc-link. The harmonics and ripple current accompanied by the increasing ESR cause further increase in core losses, which further elevate the core temperature. The increasing temperature accelerates the evaporation process of the electrolytic liquid and reduces the lifetime of the electrolytic capacitor. However, the performance and reliability of the power electronic converter are highly dependent on the reliability of the electrolytic capacitor. Therefore, it is very important to prolong the lifetime of the aging electrolytic capacitor.

Switching devices in the power electronic converters can cause both voltage and current ripples, which can greatly affect the voltage and current experienced by the electrolytic capacitor at the dc link supplying the power electronic converter. Increasing the size of the capacitor in the power electronic converter can reduce the ripple handled by the dc-link electrolytic capacitor, but it will significantly affect the response time and increase the cost.

Renewable energy sources, such as the wind or solar energy, incorporate power electronic converters to produce the required ac output voltage with the required frequency. The dc-link voltage and current ripple and the harmonics are generated by the switching operation of the power electronic switches and/or the modulation technique of the power electronic converter to produce the required power output at a specific frequency.

Fig. 1(a) shows a typical topology of an ac-dc-dc conversion circuit. The ac input is rectified through an ac-dc rectifier; the capacitor is used to maintain the dc voltage in the dc link relatively constant; and finally, the dc voltage output can be raised or lowered using the dc-dc converter supplying a dc load. For solar PV application, the rectifier can be replaced by the PV modules. Fig. 1(b) shows a typical topology of an ac-dc-ac conversion circuit, such as the wind energy conversion system, where the variable ac output of the wind generator is rectified using the ac-dc rectifier, and the capacitor is used to maintain the dc voltage in the

dc link relatively constant, and finally, a dc-ac inverter is used to produce the required ac output with the required frequency to supply an ac load..
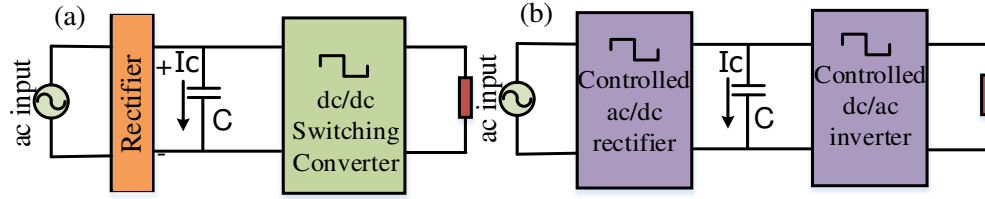
Fig. 5.1. (a) A simplified topology of an ac-dc-dc conversion; (b) A simplified topology of an ac-dc-ac conversion

In [48]–[50], the increased thermal stresses in the electrolytic capacitors are discussed and a generalized theory for the thermal stresses was presented. To address the current ripple problem in the electrolytic converter, a number of methods [51]-[54] were proposed to address the ripple problem. But these methods can mitigate only the low frequency ripples. A new trend in the dc-link ripple reduction is to manipulate the PWM carrier waveform [55]–[57]. In [11], a strategy was proposed to eliminate the lower order harmonics with selective harmonic elimination PWM. In [55], a ripple analysis in the back-to-back converter has been presented. The author proposed selective harmonic filter to omit the second harmonic component from the ripple. This technique mitigates only higher order harmonic components.

As far as the authors are aware, no method has been proposed to minimize the ripple current magnitudes in both the high and the low frequency spectrum of the electrolytic capacitor in the dc-link. This paper proposes the use of a novel shunt active filter to minimize the ripple current in the electrolytic capacitor irrespective of the frequency spectrum. The use of the shunt active filter is very popular and has been used for numerous applications. In most applications, it is used for harmonic elimination [58], [94] in an ac circuit. This paper proposes the use of a novel shunt active dc filter to filter out the ripple in the dc current of the electrolytic capacitor in a dc-link. This helps to prolong the lifetime of the electrolytic capacitor. Its performance, design principle and operating condition are also discussed.

In section 5.2, the characteristics of an electrolytic capacitor is discussed. The principle of the proposed shunt active filter is presented in section 5.3. The design principle of the shunt active filter is analysed in section 5.4. In section 5.5, the proposed strategy is verified with comprehensive simulation. Also, operating condition is derived in this section.

5.2. Electrolytic Capacitor Characteristic

The switching operation of the power electronic switches in the switch mode power converters connected to the dc link electrolytic causes current ripples in the capacitor. The input rectifier also causes further current ripples in the dc link capacitor.

Fig. 5.2 shows the equivalent circuit of an electrolytic capacitor [15], which consist of four components, the capacitance, a high resistance dc path (R_L) in parallel with capacitance, an equivalent series resistance (ESR), which represents all the resistance in the capacitor, and an equivalent series inductance (ESL), which represents all the inductance in the capacitor including leads, The ESR of the capacitor is primarily responsible for the thermal loss in the capacitor.
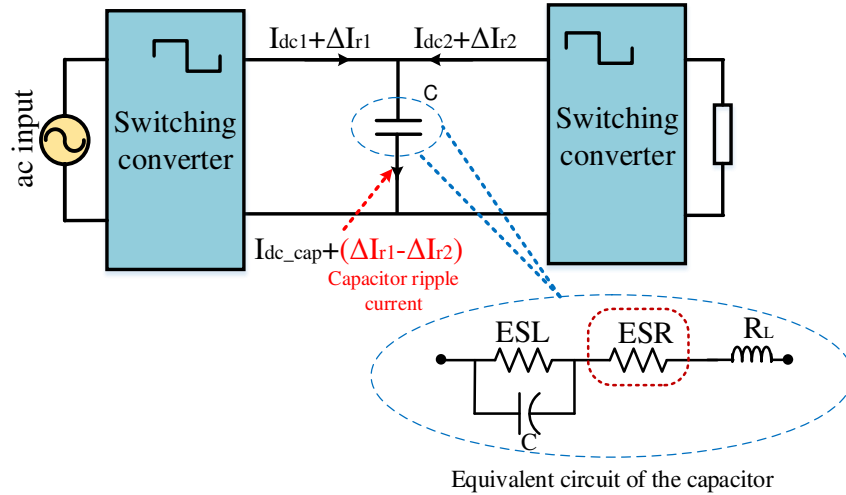
Fig. 2. Capacitor ripple current in a back-to-back converter topology and the equivalent circuit.

The evaporation of the electrolyte fluid increases the ESR. Consequently, there is a direct relation between the ESR and the liquid volume. However, it is not possible to measure the volume directly [60]. The change in volume can be determined from the change in ESR which is shown in (5.1). When the electrolyte volume is reduced by 40%, the capacitor failure occurs. From the equation it has been derived that when the liquid volume is down to 40%, the ESR increases by 2.8 times [95] and this is when the capacitor fails. where:

$$\frac{ESR}{ESR_0} = \left(\frac{V_0}{V}\right)^2 \tag{5.1}$$

The formula for calculating ESR is as below [60]

$$ESR = \frac{R_2}{1 + (2\pi f)^2 C_2{}^2 R_2{}^2} + R_1 + R_0 \tag{5.2}$$

where, R_0 is the resistance of foil, tabs, and terminals; R_1 is the resistance of electrolyte; R_2 is the dielectric loss resistance; C_2 is the dielectric loss capacitance.

From (5.2), it is evident that the ESR is dependent on the ripple frequency and the temperature. The thermal loss of the electrolytic capacitor is therefore frequency dependent The lower the frequency of the ripple current, the higher the thermal loss will be.

The formula for the thermal loss is shown in (5.3) [59]

$$P_{loss} = \sum_{n=1}^{N} \Delta I_r{}^2 (f_n).ESR(f_n) \tag{5.3}$$

where ESR (f_n) is the value of the ESR and I_{rn} is the amplitude of current ripple at a particular frequency f_n.

The formula for calculating the lifetime, L of the capacitor is given in (5.4) [59].

$$L = A.2^{\frac{T_m - T_h}{C}} \tag{5.4}$$

where, T_m is the maximum category temperature specified in the capacitor data sheet, C is the constant, and T_h is the operating temperature, and:

$$T_h = T_A + P_{loss}.R_{th} \tag{5.5}$$

where R_{th} is the thermal impedance from case-to-ambient.

If the ripple current magnitude is high, the thermal loss in the capacitor will be high causing a high core temperature. The elevated core temperature results in the evaporation of electrolytic liquid and causes further increase in ESR.

This thesis proposes a method using the shunt active filter to reduce the amplitude of the ripple current in the capacitor, resulting in the reduction of the thermal loss as shown in (5.3) and an increase the lifetime of the capacitor as shown in (5.4).

5.3. Shunt Active Filter

The magnitude of the ripple current in the dc current of the capacitor can be minimized by deliberately injecting an appropriate current, at the node where the capacitor is connected, to produce the required ripple by the input and the output switching converters. This current injection is done by an appropriately designed current source inverter (CSI). However, the reference of this inverter has to be carefully determined. Otherwise, it would worsen the ripple condition. The principle of the proposed shunt active filter with two topologies is described in this section where the strategy for determining appropriate reference current is explained.

Topology: I: Topology I is used where the input side of the capacitor injects pure dc current but the output side produces a ripple current. This can occur, for example, in the case where a DC source has been connected at the input of the capacitor for some time and a dc-dc converter is connected at the output of the capacitor. In this case, I_3 current is pure dc current whereas; I_1 is a dc current with a superimposed ac-ripple. If I_1 and I_3 were both dc, there would be no ripple in the capacitor current. Fig. 5.3(a) shows that the capacitor current, I_2, which is the difference between I_3 and I_1, will now contain dc and ac ripple. Now, by injecting a current, I_4, in the B node, as shown in Fig. 5.3(b), where I_4 is exactly equal to the ac-ripple component of I_5 current, I_1 is made to be pure dc *($I_5 = I_1 + I_4$)*. I_5 was equal to I_1 before the current injection, as it is not desirable to change the performance of the power converter supplied by the capacitor in the dc link. Since, the capacitor current I_2 is the difference of I_3 and I_1, the capacitor current becomes a relatively pure dc current with a small high frequency ripple due to the switching needed to obtain I_4.
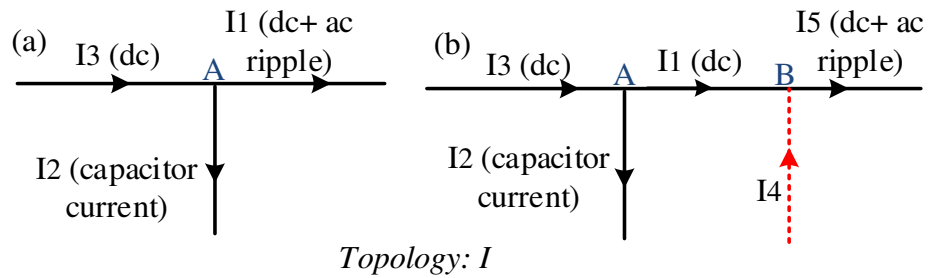

Fig. 5.3. Topology I from shunt active dc filter

Topology: II: Topology II is used where both sides of the capacitor inject ripple currents. This can occur, for example, in the case where a rectifier has been connected at the input of the capacitor and an inverter is connected at the output of the capacitor. Fig. 5.4 shows Topology 2. In this case, I_1 and I_3 both contains ac-ripple component. Therefore, unlike topology I, I_1 and I_3 both would be needed to be dc in order to make capacitor current ripple free and it would require two separate shunt active filter. Therefore, a different strategy is needed here. From node A the capacitor current is flowing in an outward direction, which contains a dc current with some ac ripple. The ripple component of the capacitor current, I_2, is the difference between the ripple components of current I_3 and I_1. Similarly, the dc component of I_2 is the difference between the dc components of I_3 and I_1. Now, if a current, I_4 is injected in node A in an outward direction such that I_4 is exactly equal to the ac-ripple difference of I_3 and I_1 ($I_4 = I_3^{ac} - I_1^{ac}$), according to circuit theory, I_2 will only have the dc component. The resulting new capacitor current becomes a relatively pure dc current with a small high frequency ripple due to the switching needed to obtain I_4.

I_3 (dc+ ac ripple)   A I_1 (dc+ ac ripple)

I_4 I_2 (capacitor current)
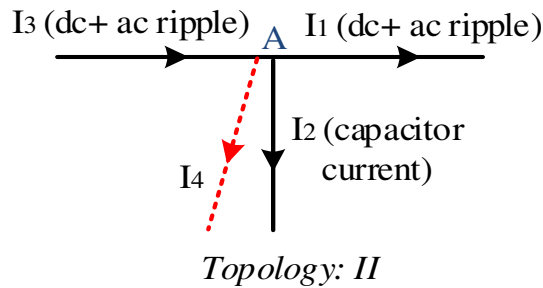
Topology: II

Fig. 5.4. Topology II for shunt active dc filter

The above topologies will reduce the ripple current magnitude in the electrolytic capacitor in the dc link, resulting in the reduction of the thermal loss and an increase the lifetime of the capacitor.

5.4. Shunt Active Filter Design principle

Fig. 5.5 shows the two topologies described in Section III for the proposed shunt active filter. One of the design challenges is to choose the appropriate value of the inductor. To deal

with the high frequency ripple it is imperative that the response of the active filter current is fast enough to follow the fluctuating reference input, which is the ac-ripple signal of the load current for Topology I and the difference between the input and the output ripple signals for Topology II. The response time is dependent on the inductor value. The following analysis is needed to be performed before choosing the inductor size.
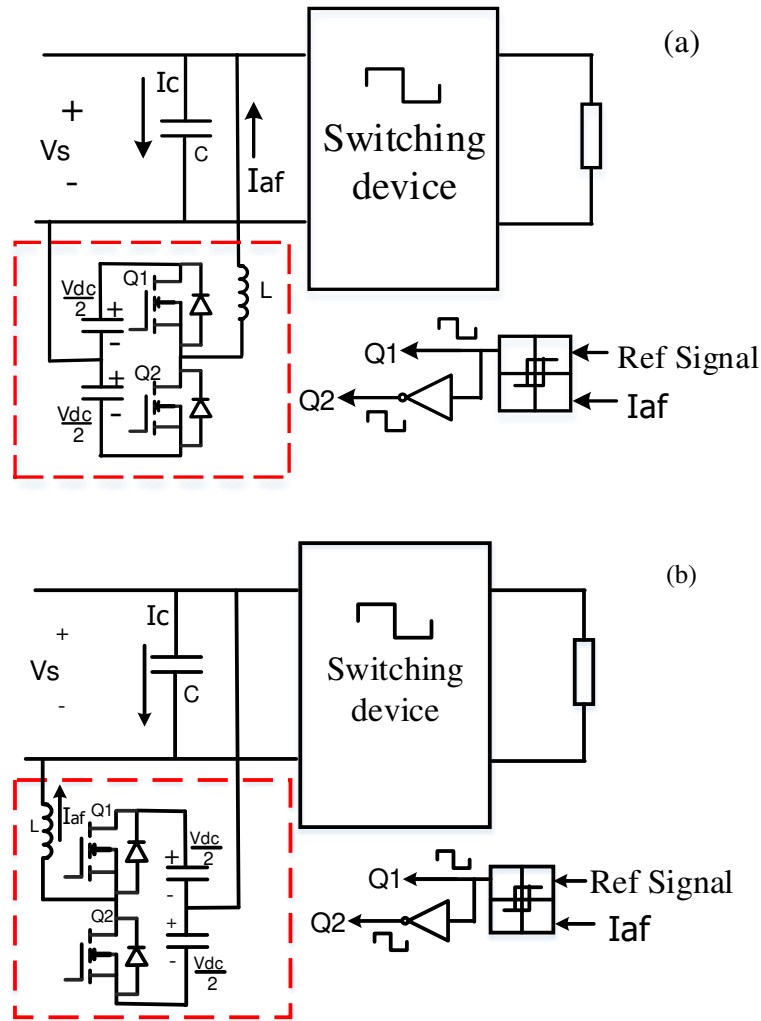
Fig. 5.5 . Shunt avtive current filter principle (a) Topology I; (b) Topology II.

Fig. 5.6 shows the V_{dc} and I_{af+}, which are the shunt active filter voltage and current when L is the inverter inductance. It is important to note that the amplitude of the dc voltage source of the active filter should be higher than the maximum amplitude of the input dc voltage, Vs.
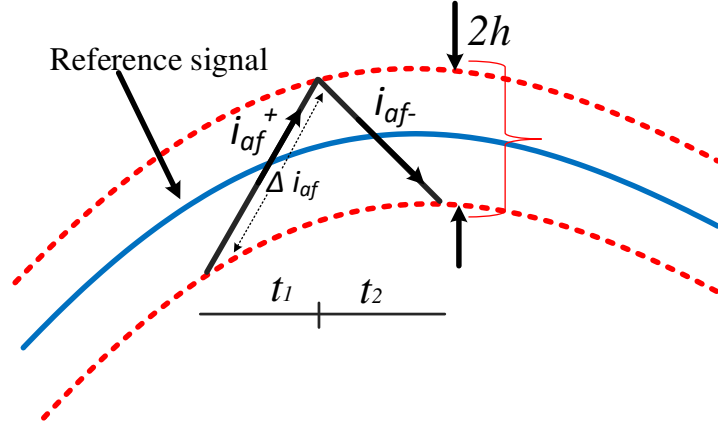
Fig. 5.6. Inverter current with hysteresis control

In this case, when Q1 is ON, the inductor current of the active filter will increase (positive ramp),

$$i_{af^+}(t_1) = \frac{0.5V_{dc} \quad V_s}{L} t_1 + i_{af}(t_0) \tag{5.6}$$

Similarly, when the positive ramp of the inductor current reaches the upper limit of the hysteresis band, Q1 is turned off and Q2 is turned on, and the active filter inductor current will decrease (negative ramp),

$$i_{af}(t_2) = \frac{0.5V_{dc} \quad V_s}{L} t_2 + i_{af^+}(t_1) \tag{5.7}$$

Therefore the height of the active filter ripple current is,

$$i_{af}(t) = \left| \frac{0.5V_{dc} \quad V_s}{L} t_1 \right| = \left| \frac{0.5V_{dc} \quad V_s}{L} t_2 \right| \tag{5.8}$$

To achieve an increased performance, the slew rate needs to be high enough to be able to

follow the reference signal. The formula for calculating the slew rate is shown in (5.9). The appropriate value of inductance needs to be determined from (5.9).

$$\frac{di_{af}(t)}{dt} = \left| \frac{\pm |0.5V_{dc}| \quad V_s}{L} \right|$$

(5.9)

The operation of the active filter can then be summarized as follows: when the inverter current crosses the lower limit of the hysteresis band, the upper switch of the active filter, Q1, will be turned "ON" and when the active filter current crosses the lower switch, Q2, will be turned "ON". The turning of the switches is mutually exclusive. The hysteresis controller sends the switching signal to the switches of the shunt active filter accordingly, and the hysteresis band can be a fixed band or a variable band. The upper and lower limits of the hysteresis band have to be defined for better response. A very narrow hysteresis band will make the active filter current track the reference current more accurately, but the switching frequency will be very high. On the other hand, a wide hysteresis band will make the switching frequency lower, but it will reduce the waveform quality and increase the tracking error. The hysteresis band is *(2h)* chosen as 1% of the average value of the reference signal as shown in Fig. 5.6.
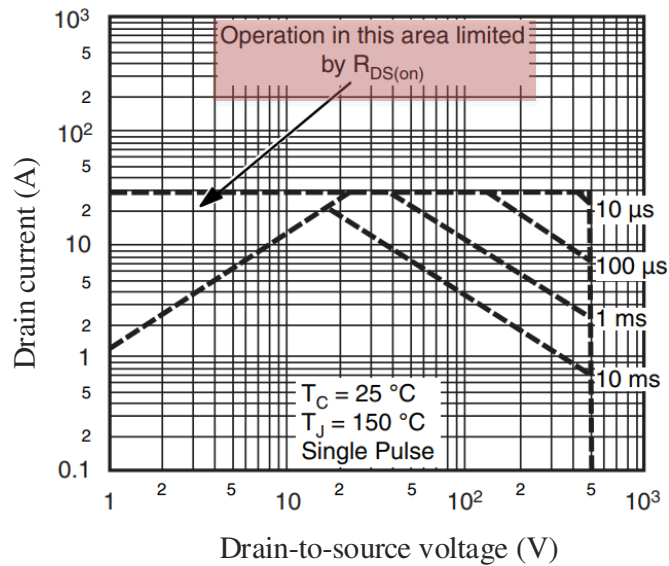
Fig. 5.7. Safe operating area (SOA) for Vishay Siliconix IRF840LC [99]

Since, the current and voltage rating is small for the proposed filter and the required switching frequency can be very high, the power MOSFET has been chosen for this application. For every power MOSFET, there is a safe operating area (SOA) which can be found in the manufacturer data sheet. The safe operating area is a function of drain-to-source voltage, drain current and drain current frequency. Therefore, the MOSFET switching frequency is important for determining the SOA. Fig.5.7 shows the SOA for the chosen Vishay Siliconix IRF840LC MOSFET.

The rate of change or the slope for the rising and falling active filter output current, I_{af+} and I_{af-} respectively can be expressed as (5.10). The ($^\bullet$) operator over any variable denotes its first derivative.

$$\begin{bmatrix} \dot{i}_{af^+} & \dot{i}_{af^-} \end{bmatrix} = \frac{1}{L}\begin{bmatrix} (0.5V_{dc} - V_s) & -(0.5V_{dc} - V_s) \end{bmatrix} \tag{5.10}$$

For the switching interval between t_1 and t_2, and hysteresis band of h,

$$\begin{bmatrix} \dot{i}_{af^+} - \dot{i}_{af^*} \\ \dot{i}_{af^-} - \dot{i}_{af^*} \end{bmatrix}^T \begin{bmatrix} t_1 & 0 \\ 0 & t_2 \end{bmatrix} = [h]\begin{bmatrix} 2 & -2 \end{bmatrix} \tag{5.11}$$

$$t_1 + t_2 = T_s = \frac{1}{f_s} \tag{5.12}$$

Where, fs is the active filter switching frequency that needs to be calculated.

Manipulating (5.10)–(5.12), (5.13) can be obtained, from which t_1 and t_2 can be obtained in (5.14):

$$\begin{bmatrix} \dot{i}_{af^+} & \dot{i}_{af^-} \end{bmatrix}\begin{bmatrix} t_1 \\ t_2 \end{bmatrix} = \frac{1}{f_s}\begin{bmatrix} \dot{i}_{af^*} \end{bmatrix} \tag{5.13}$$

$$\begin{bmatrix} t_1 \\ t_2 \end{bmatrix} = \begin{bmatrix} \overset{\bullet}{i}_{af^+} & \overset{\bullet}{i}_{af^-} \end{bmatrix}^{-1} \frac{1}{f_s} [\overset{\bullet}{i}_{af^*}]$$

$$= \begin{bmatrix} (0.5V_{dc} - V_s) & -(0.5V_{dc} - V_s) \end{bmatrix}^{-1} \frac{1}{Lf_s} [\overset{\bullet}{i}_{af^*}]$$

(5.14)

From (5.11),

$$\left\{ \begin{bmatrix} \overset{\bullet}{i}_{af^+} & \overset{\bullet}{i}_{af^-} \end{bmatrix} \begin{bmatrix} 1 & 0 \\ 0 & -1 \end{bmatrix} - [\overset{\bullet}{i}_{af^*}][1 \quad -1] \right\} \begin{bmatrix} t_1 \\ t_2 \end{bmatrix} = 4[h]$$

(5.15)

From (5.14) and (5.15), the switching frequency of the MOSFET can be determined in (5.16):

$$\left\{ \begin{bmatrix} (0.5V_{dc} - V_s) & -(0.5V_{dc} - V_s) \end{bmatrix} \begin{bmatrix} 1 & 0 \\ 0 & -1 \end{bmatrix} - [\overset{\bullet}{i}_{af^*}][1 \quad -1] \right\}$$

$$\begin{bmatrix} (0.5V_{dc} - V_s) & -(0.5V_{dc} - V_s) \end{bmatrix}^{-1} [\overset{\bullet}{i}_{af^*}] = f_s[h]$$

(5.16)

5.5. Verification of the Proposed Filter Technique and Discussions

The proposed use of the shunt active filter to reduce the magnitude of the current ripple in the electrolytic capacitor in the dc link described in Section III will be validated in this section using simulations using the Matlab/Simulink simulation software.

5.5.1. Operating condition:

In section 5.4, the MOSFET switching frequency has been derived for a specific hysteresis band. For a higher switching frequency, the hysteresis band will be smaller. However, the reliability of the MOSFET used in the active filter needs to be ensured. To protect the power electronic switches from early failure, the MOSFET always needs to be operated in the safe operating zone as provided in the data sheet. For a specific drain-to-source voltage and

switching frequency, the safe operating current needs to be determined.
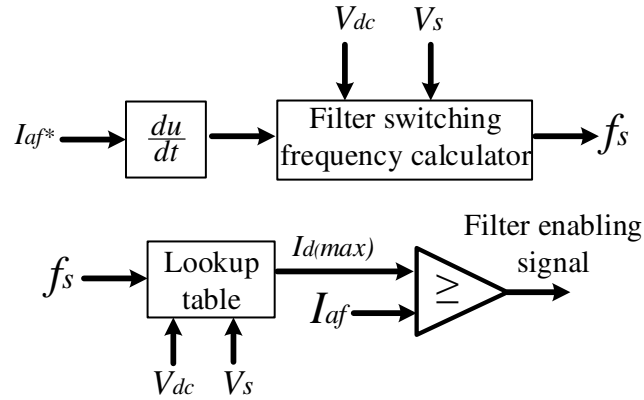
Fig. 5.8 . Enabling signal based on MOSFET safe zone operation look-up table.

If the current is beyond the SOA, the filter will not operate. A lookup table constructed from the manufacturer data sheet can be used to determine the maximum safe operating current. Fig. 5.8 shows how the safe zone operation using a look up table is used to determine whether the filter will be enabled or not depending on the obtained switching frequency from (16).

5.5.2. *Test results of the proposed active filter in Simulink environment:*

Case 1: In this case, a standalone PV system will be considered. The circuit in Fig. 5.9 shows a boost converter supplied by a photovoltaic source. Table 5.1 shows the system parameters of Fig. 5.9.
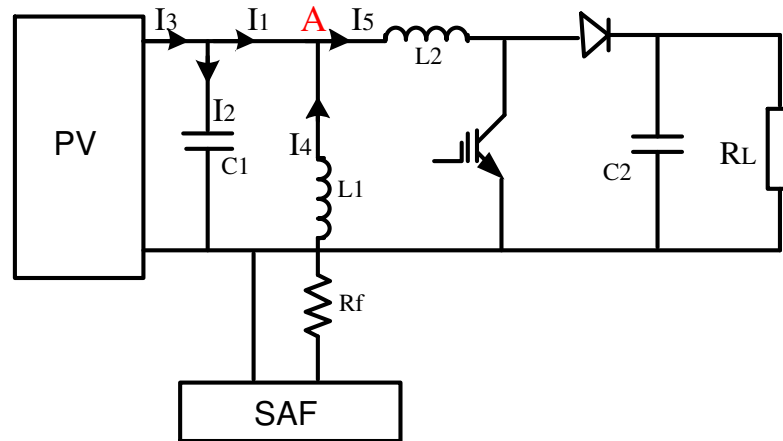
Fig. 5.9. Standalone PV system.

TABLE 5.1

System Parameters (case 1)

Symbol	Parameter	Value	Unit
L_1	SAF coil inductance	2	mH
L_2	Boost coil inductance,	1	mH
R_f	SAF resistance,	0.007	Ω
C_1	Source side capacitance,	33	μF
C_2	Load side capacitance,	47	μF
R_L	Load Resistance,	10	Ω

At any instance of time, the current from the PV source is assumed to contain no ripple; whereas without the shunt active filter, the inductor current of the boost converter, I_5, which is the same as I_1, contains significant ripple due to switching of the MOSFET to obtain a good dc power output. The capacitor current, I_2, which is the subtraction of the PV current, I_3, and the inductor current of the boost converter, I_1, will therefore contains a significant ripple, caused by the ripple in I_1. The Topology I in Section III will be used in this case to minimize the capacitor ripple current. The control algorithm for the shunt active filter of Topology I in the form of a current source inverter (CSI) is shown in Fig. 5.10.
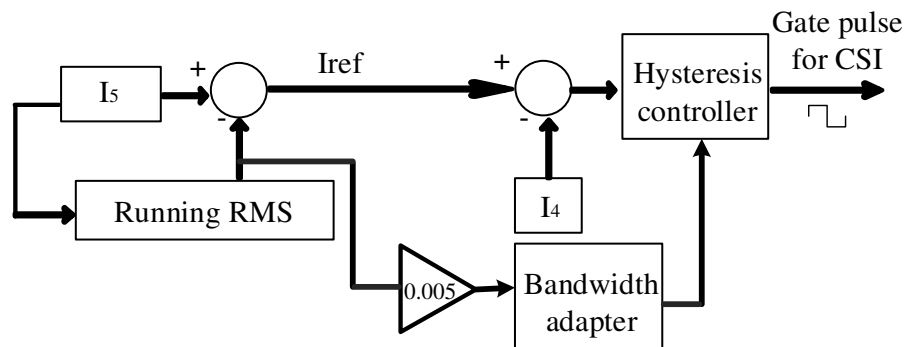
Fig. 5.10. CSI control algorithm for topology 1.

The dc current I_5 is subtracted from its dc component using the 'running RMS' function in Simulink and used as the reference current for the shunt active filter. At any instant of time, the current in I_4 is compared with the reference current using the hysteresis controller, from

which the gate signals of the two MOSFETS are determined. The hysteresis band is *(2h)* chosen as 1% of the average value of the boost converter current as shown in Fig. 6.
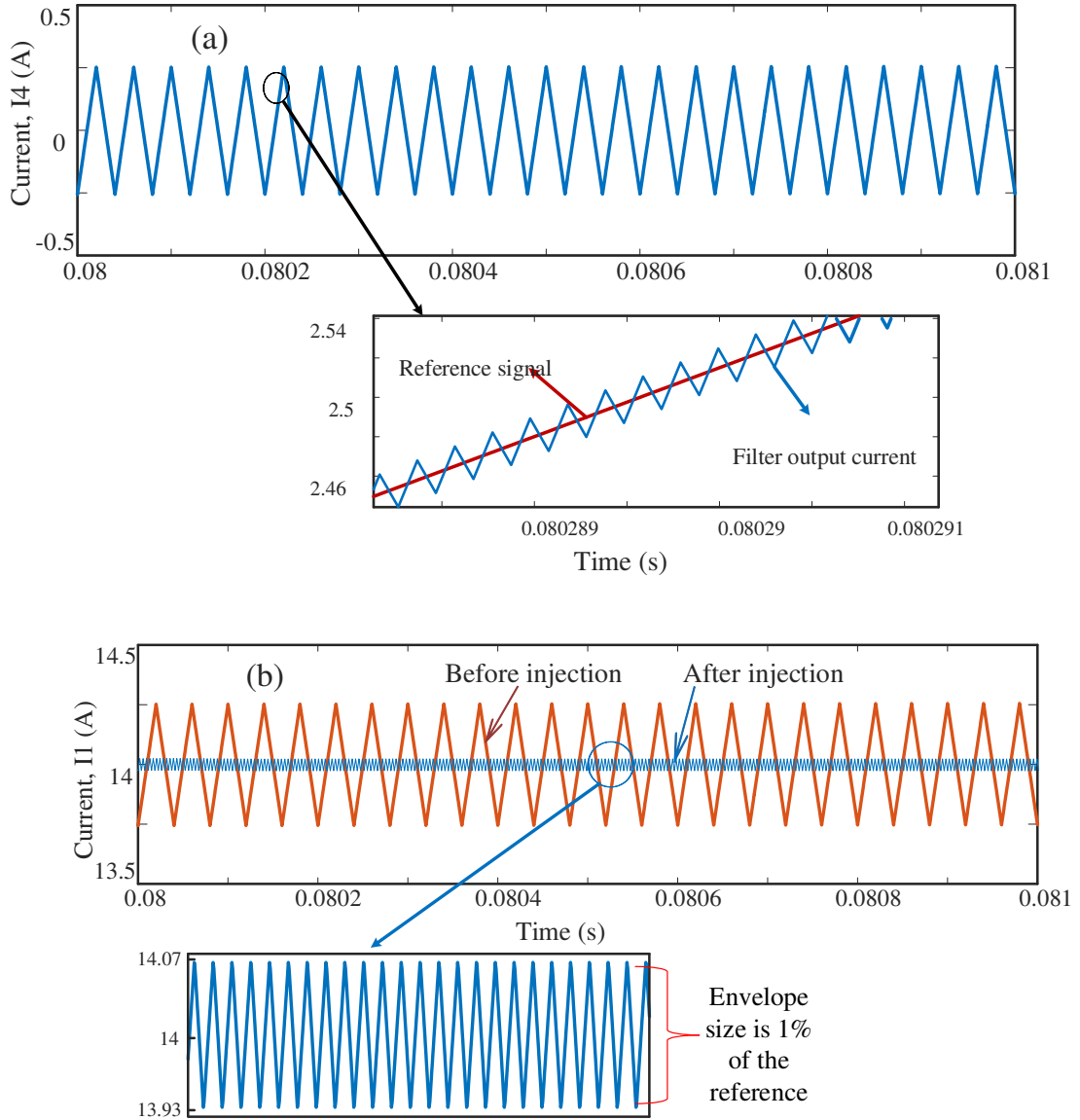
Fig. 5.11. (a) Active filter output current, I_4; (b) Boost inductor current, I_1

Fig. 5.11(a) shows the shunt active filter output current, I_4 which follows the reference current. Fig. 5.11 (b) shows the current, I_1 before and after the current, I_4 injection. The injection of I_4 current makes the I_1 almost dc with a small high frequency component due to the chosen hysteresis band, which is chosen to be equal to 1% of the average value of I_5 as shown in the zoomed window of Fig. 5.11(b).
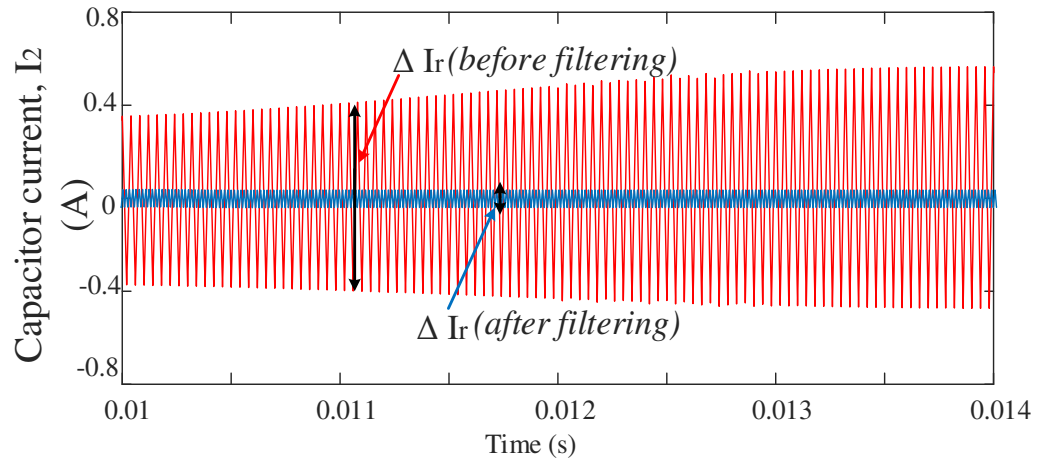
Fig. 5.12. Capacitor Current, I_2

Now, since the current I1 and I3 are both almost dc, the capacitor current, I2 will be almost DC as well. Fig. 5.12 shows the improved capacitor ripple current, I2 before and after filtering.

Case 2: Another simulation has been carried out with the circuit shown in Fig. 5.13 where the capacitor is between a three-phase rectifier and a boost converter. Table 5.2 shows the system parameters of Fig. 5.13.

TABLE 5.2

System Parameters (case 2)

Symbol	Parameter	Value	Unit
L_1	SAF coil inductance	2	mH
L_2	Boost coil inductance,	1	mH
R_f	SAF resistance,	0.007	Ω
C_1	DC-Link capacitance,	47	μF
Ls	Source inductance,	0.0062	μF
R_L	Load Resistance,	100	Ω
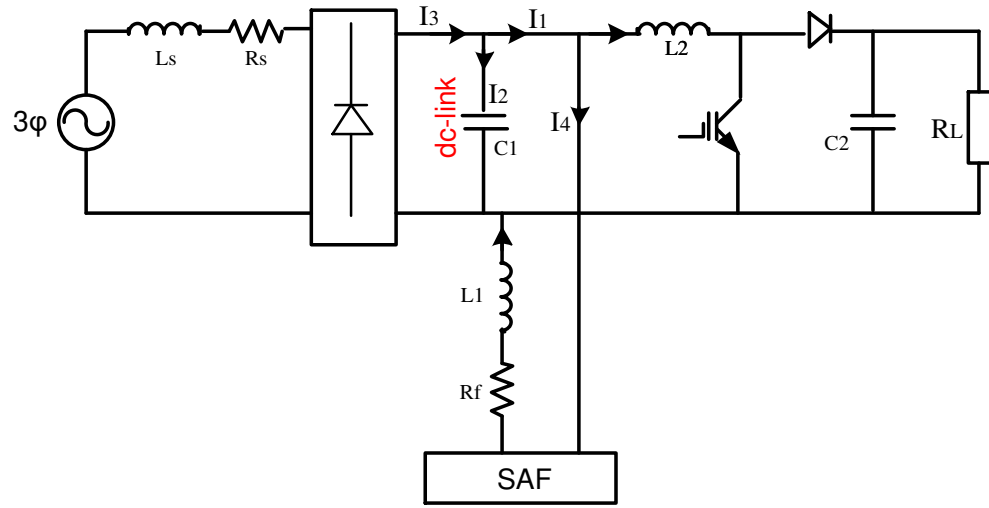
Fig. 5.13. A three phase rectifier interfaced with a boost converter.

The capacitor works here as a dc-link. As discussed earlier, the high magnitude of the capacitor ripple current cause significant stress on the capacitor and degrades the lifetime. To minimize the capacitor ripple current, I_2, the Topology II is utilized in this circuit.
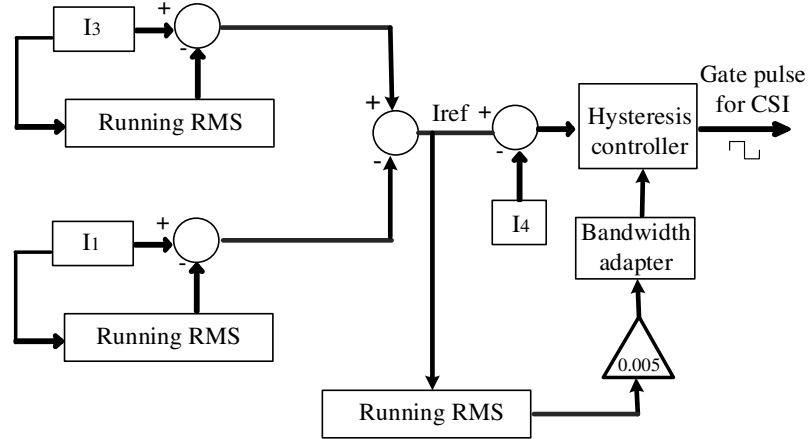
Fig. 5.14. Control algorithm of CSI for topology 2.

The control algorithm for the shunt active filter of Topology II is shown in Fig. 5.14. The ac ripple component of both current I_1 and I_3 are extracted. Then, their difference is fed as the reference current to the hysteresis controller to be followed by the active filter output

current, I_4. The hysteresis band is *(2h)* chosen as 1% of the average value of the reference signal as shown in Fig. 6.

Fig. 5.15(a) shows the current I_1 from the boost converter and Fig. 5.15(b) shows the rectifier ripple current. The capacitor current, I_2 is the difference between I_3 and I_1. According to Topology II, the injected current, I_4 has to be the difference of the ripple components of I_1 and I_3 as shown in Fig. 5.16, so that the capacitor current, I_2 contains only the dc component which is the difference of the dc components of I_1 and I_3. The result in Fig. 5.17 shows that the capacitor ripple current is significantly improved. The slight ripple is due to the hysteresis band which is very small.
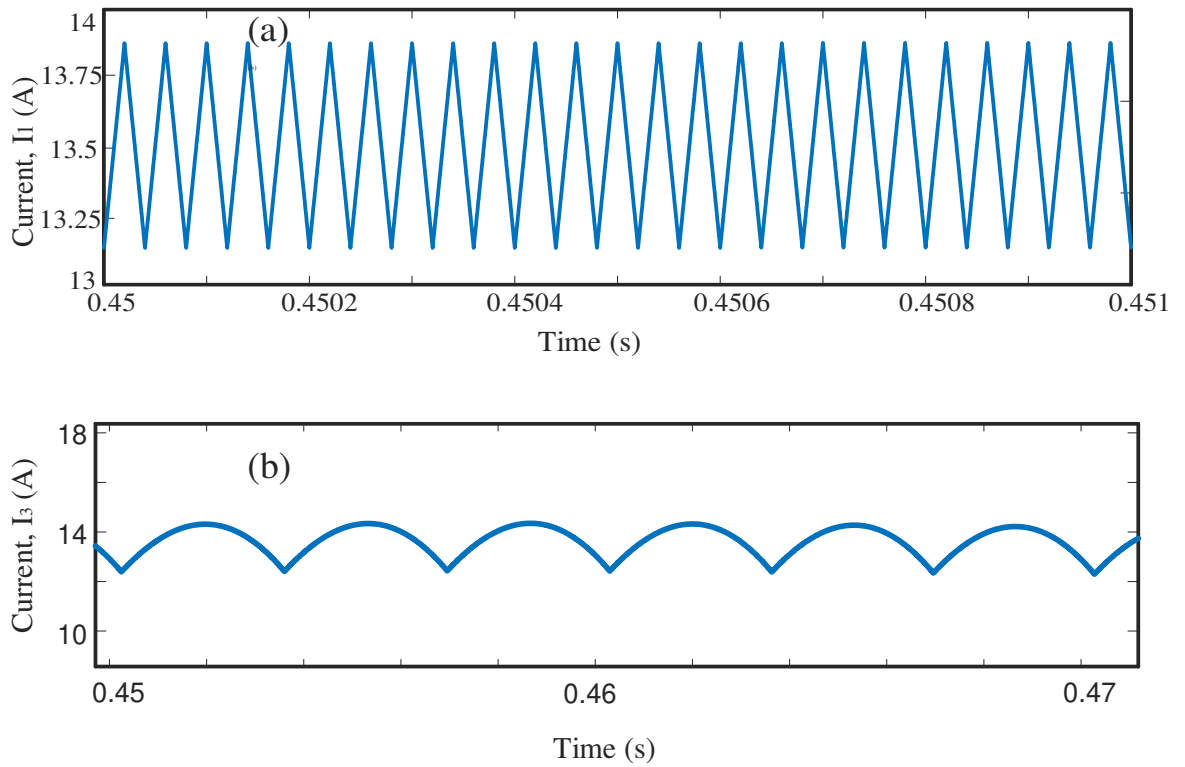
Fig. 5.15. (a) Boost inductor current, I_1; (b) 3 phase rectifier ripple current, I_3.
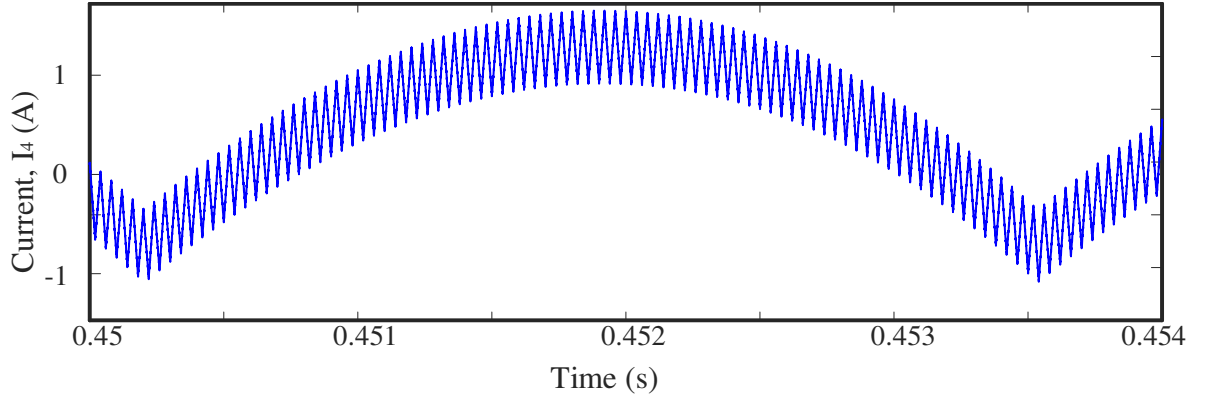
Fig. 5.16. Active filter output current, I4 ($I_4 = I_3{}^{ac} - I_1{}^{ac}$)
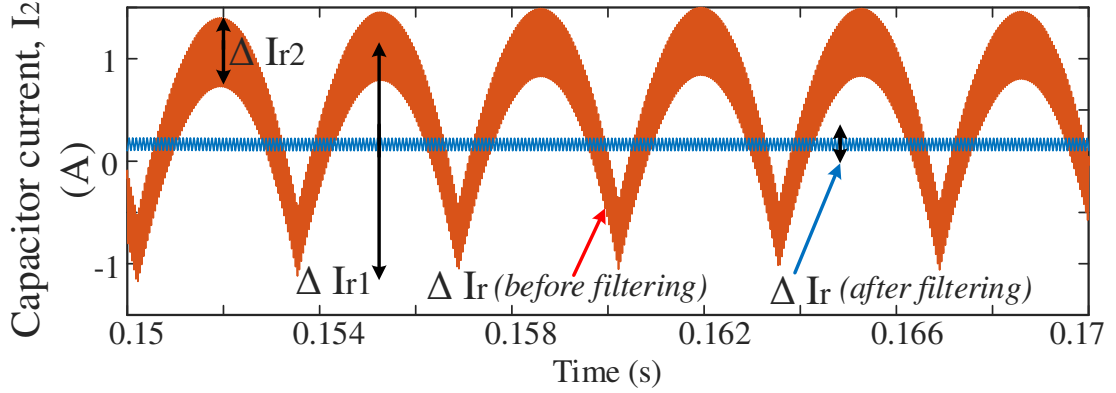
Fig. 5.17. dc-link capacitor current, I_2 (before and after filtering)

The proposed shunt active filter technique proves to be very effective in reducing the magnitude of the ripple current of the electrolytic capacitor in the dc link. As discussed earlier in section II, the reduction of the magnitude of the ripple current will significantly improve the lifetime of the electrolytic capacitor.

The proposed shunt active filter technique proves to be very effective in reducing the magnitude of the ripple current of the electrolytic capacitor in the dc link.

For *case I*, as it is seen from Fig. 12, the ripple magnitude, ΔI_r has decreased from 0.8A (p-p) to 0.14A (p-p). Which, as a result, reduces the core loss more than 32 times according to (3). For *case II*, Fig. 17 shows that the capacitor ripple current has ripples from two frequency spectrum. The low frequency component, ΔI_{r1} comes from the rectifier and the high frequency component, ΔI_{r2} comes from the boost converter inductor current ripple. The proposed technique mitigates both the low and high frequency components. Therefore, the

core loss improvement in this case is more significant since the low frequency components are more damaging. From (2), it is evident that the ESR is higher for low frequency ripple and higher ESR causes higher core loss. Since, the low frequency component of higher magnitude from the rectifier is totally removed, the major core loss is mitigated. Only a very low magnitude high frequency ripple is present in the capacitor current which is due to the hysteresis band and its switching. However, in both cases, not only the ripple magnitude is minimized but also the ripple is replaced by a very small magnitude of a very high frequency ripple caused by hysteresis switching. Therefore, as discussed earlier in section II, the reduction of the magnitude of the ripple current will significantly improve the lifetime of the electrolytic capacitor.

5.6. Experimental Validation of The proposed Approach

The proposed technique is validated in this section for *case I* using Topology I. The circuit diagram in Fig. 9 is used for the experiment. However, instead of the PV module, two sets of 12V battery packs are connected in series to make it 24V source. The boost converter is implemented with SEMITEACH IGBT module. The boost converter pulse has a fixed duty cycle of 0.5 throughout the experiment. The current source inverter for the shunt active dc filter is implemented with one C2M0080120D SiC MOSFET module from CREE. This module has voltage rating of 1.2 kV and current rating of 50A. This module can withstand very high switching frequency. For boost converter switching dSpace 1103 module has been used to provide a PWM pulse with a fixed duty cycle whereas, for SiC MOSFET switching and data reading DSP (TMS320F28335 Microcontroller) has been used. The data are processed in MATLAB/Simulink. The full experimental setup is demonstrated in Fig. 18. Fig. 18(a) shows the schematic of the experiment and Fig. 18(b) shows the full setup.
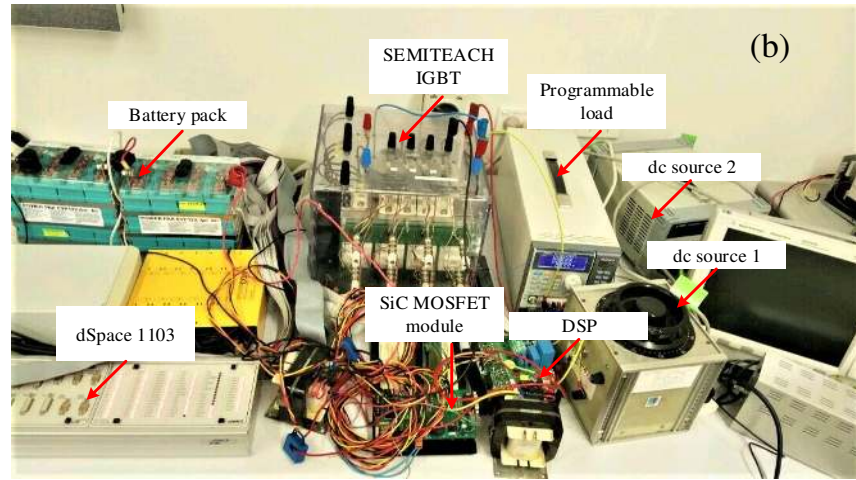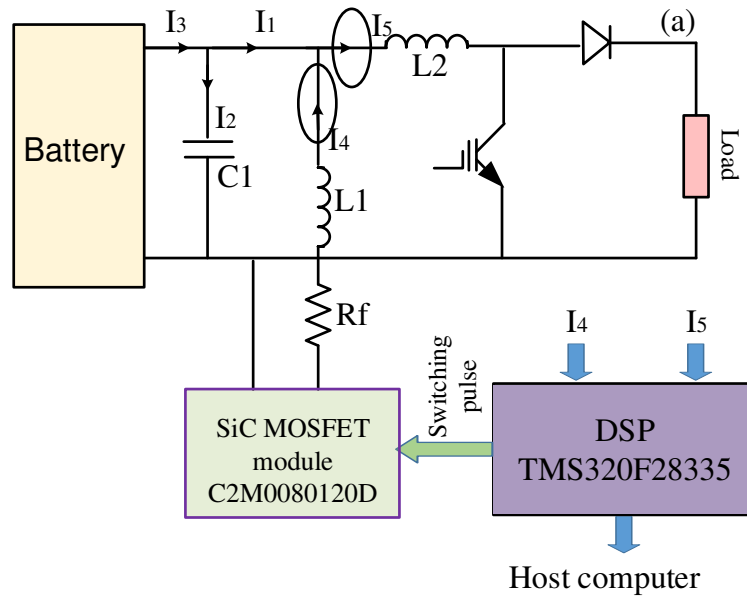
Fig. 18. Experimental setup for validation of the proposed technique.

Fig. 19(a) shows the ripple in capacitor branch before filtering. Since, the input is already a pure dc, the ripple in capacitor branch is resulted from the boost converter ripple current in inductor. The DSP reads the filter output current, I_4 and boost converter current, I_5 which is fed into the host computer. The controller in the host computer sends the switching command to the DSP based on the readings. The controller used in this experiment is same as Fig. 10. The DSP then sends the switching signal to SiC MOSFET module which works here as a CSI. After filtering the ripple current is improved significantly as seen from Fig. 19(b). The CSI injects the current in the capacitor node which improves the ripple. The slight ripple that

is being seen in Fig. 19(b) is due to the switching and hysteresis band of the CSI controller. The current waveforms are collected from the KEYSIGHT DSOX4024A oscilloscope using Agilent N2779A current probe.
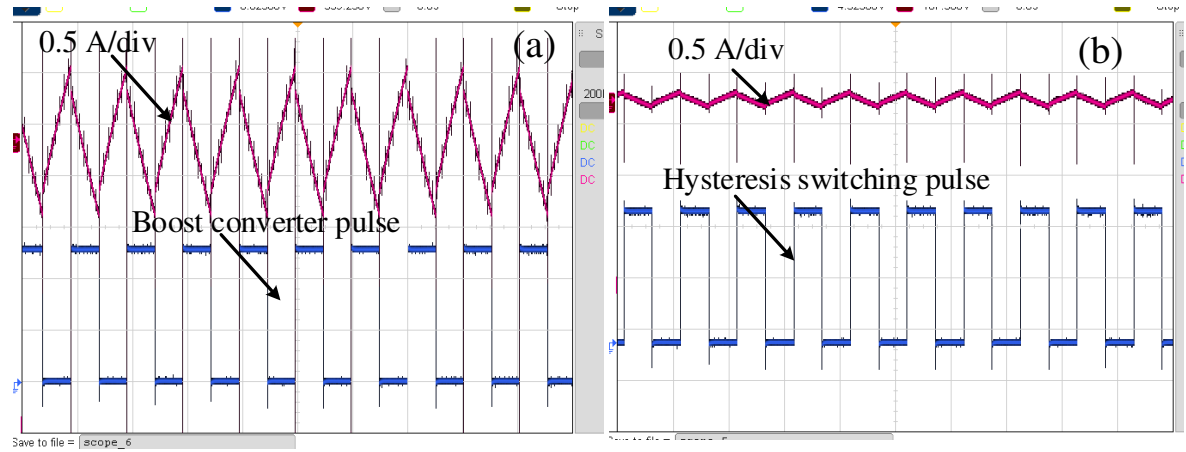
Fig. 19. (a) The capacitor current ripple before filtering; (b) after filtering.

5.7. Summary

The mechanism that causes the dc current ripple that results in an increased thermal stress in the electrolytic capacitor in a power electronic converter has been analyzed in this paper. Also, a novel strategy using a shunt active current filter has been proposed to reduce the capacitor current ripple. This filter has been utilized to deliberately inject the necessary ripple current at the node connected to the capacitor to compensate for the ripple current in the electrolytic capacitor. A comprehensive analysis of the design and the operating principle of the proposed novel active filter has also been presented. The proposed strategy has been verified using simulations based on the MATLAB/Simulink simulation software and laboratory experiments. The results show a significant reduction in the magnitude of the capacitor ripple current that can reduce the thermal stress and prolong the life expectancy of the electrolytic capacitor.

Chapter 6

Conclusions and Future Work

6.1. Conclusions

The remote and rural areas can facilitate the renewable energy sources for power generation by providing the necessary geographical space resulting in minimal negative impacts on the daily livelihood. But the most common challenge of the renewable energy resources is their intermittent nature, which can reduce the overall system reliability. Also, the control of the RAPS system is complex, because the RAPS system are prone to the network disturbances, unlike in the large utility grid. The RAPS system needs to supply the demand on its own and cannot depend on the grid. Therefore, it is expected that each component of the RAPS system participates in supporting the network events. Renewable energy systems are connected to the RAPS system by power electronic converters. This decreases the total system inertia. If the penetration of the renewable energy sources increases, the system reliability will decrease even further.

The reliability of the system components is also important. The energy conversion system of the renewable energy resource consists of several components that are often prone to failure. The lack of reliability of any of those components can lead to overall low system reliability. These issues need to be solved to improve the RAPS reliability.

After going through all the technical challenges associated with a RAPS system, the outcome of this thesis provides a solid contribution towards improved control and reliability of RAPS system. The improvements that have been achieved are:

(1) Frequency regulation improvement:

A frequency response control strategy has been proposed for a permanent magnet synchronous generator based wind energy conversion system. An artificial inertia controller was used to release the kinetic energy to support sudden frequency dip, by using a suboptimal power point tracking strategy for PMSG based WECS to ensure a power reserve for frequency response. It also prevented a secondary frequency event due to sudden operating point shift.

(2) Frequency regulation improvement by SMES:

A frequency regulation strategy has also been proposed using the SMES. Since the artificial inertia controller causes a high torque stress on the drive train, a power support from external energy storage is required. The SMES has a very fast response time and its power density is very high. The result shows that the SMES has much better performance in the frequency regulation than the artificial inertia controller or even the use of the super-capacitor. The system frequency nadir is 49.4 Hz for the super-capacitor whereas, the system frequency nadir is 49.8 Hz during sudden load increase. Also, the RoCoF becomes less than the allowable maximum limit of 0.5 Hz/s. These results demonstrate clear improvement of the dynamic frequency response of the RAPS system with the integration of SMES.

(3) Thermal Stress Relief for Power electronic converter:

A strategy to minimize the thermal stress on the rotor side converter has been proposed for the DFIG based WECS. The simulation results show that when the DFIG is operated in low slip, it has caused significant thermal stress on the semiconductor junctions of the rotor side converter. The temperature cycling has been quantified. Also, a coordinated strategy with the switching frequency and the reactive current control has been proposed to reduce the thermal stress. A technique has been proposed to ensure that the usual performance and power quality of the DFIG is not compromised. The results show that the proposed technique reduces the thermal fluctuations by 8 $^{\circ}$C which in result, exponentially increases the lifetime. In the example shown in this thesis, the lifetime is improved my 19 times.

(4) Stress minimization of the electrolytic capacitor:

The aluminum electrolytic capacitor is commonly used in a power electronic converter based system. Due to high ripple current in the converter, the thermal loss in the capacitor can be very high and can often cause failure of the capacitor. The main cause of this is the electrolytic volume reduction below a certain limit. A stress analysis has been carried out in this thesis to investigate the mechanism of the core loss. Also, a harmonic spectrum analysis has been carried out to investigate the effect of different values of slips on the harmonic generated ripple for the dc-link capacitor in a DFIG based WECS. An active filter was proposed to minimize the capacitor loss in this thesis. Two topologies have been proposed to minimize the ripple current. The shunt active filter effectively removes the ripple from the capacitor current. Although, since, hysteresis controller has been used here, a small ripple due to hysteresis band (2% of the reference dc-component) is observed in the capacitor current. The simulation results of the proposed strategy validate the proposed strategy which significantly increases the capacitor lifetime.

All of those aspects have been verified through detailed simulation models constructed in Simulink/MATLAB. All the parameters have been chosen according to real case scenarios.

6.2. Future Work

In this thesis, the several proposed strategies have been verified in a small network of renewable energy and energy storage based hybrid RAPS system. It includes the system with and without the natural inertia to showcase the challenges and the effectiveness of the proposed solutions. However, these strategies can be verified in a RAPS system with a large network.

The RAPS systems investigated in this thesis are (i) a PMSG-based WECS and a diesel generator, (ii) a PMSG-based WECS, a diesel generator and an SMES, (iii) a DFIG-based WECS and a diesel generator. The RAPS system with more variations of renewable sources or different types of energy storages can be used to verify those techniques. A 100% renewable energy based RAPS system with storage is being developed by a number of power utilities. The strategies proposed in this thesis need to be adapted to be effective in a 100% renewable energy based RAPS system.

In this thesis, the performance of RAPS systems are investigated in balanced conditions. But in practical, the system may be unbalanced. In unbalanced condition, network parameter control is really challenging. The control strategies proposed in this thesis are suitable only for balanced condition. The strategies should be extended to be useful for unbalanced condition as well so that the RAPS system becomes robust in cases of faults.

The RAPS system networks analyzed in this thesis, are considered only for standalone operation. However, with the grid expansion, the RAPS systems may very well come under utility grid. The control strategies should be fine-tuned to be effective for grid-interactive RAPS systems as well. Hence, the reliability of the RAPS system will be ensured regardless of its grid connected or standalone operation.

In this thesis, a strategy has been proposed for the frequency regulation using the SMES. The charging/discharging algorithm has been developed. However, to reduce the stress on the energy storage during sudden power fluctuation, a machine learning based algorithm can be developed in future work to use the historical data in order to predict the fluctuation at a given time period so that enough power can be reserved in the storage.

In Chapter 5, a shunt active filter was proposed to minimize the ripple current of the capacitor in a dc-link due to the use of power electronic converter in the load side. The control strategy of this filter can be extended to filter out the ripple current from the source side.

Finally, the proposed strategies in this thesis are verified through simulation. However, proper prototype can be developed to verify the proposed strategies experimentally. Also, the cost-benefit analysis can be performed to compare the economic benefits from the proposed strategies and the expenses to adopt those techniques.

Bibliography

[1] Global Carbon Budget 2018, Earth Syst. Sci. Data, 10, 2141-2194, 2018.

[2] M. Islam, Y. Guo & J. Zhu, "A review of offshore wind turbine nacelle: Technical challenges, and research and developmental trends," *Renew, and Sustain. Energy. Rev.*, vol. 33, pp. 161-176, 2014.

[3] M. G. Kanabar, C. V. Dobariya, and S. A. Khaparde, "Rotor speed stability analysis of constant speed wind turbine generators", In: Proceedings of the *power electronics drives and energy systems conference*; 2006. P. 1–5.

[4] D. Jingya, X. Dewei, and W. Bin, "A novel control system for current source converter based variable speed PM wind power generators", In: Proceedings of the *IEEE power electronics specialists conference*; 2007. P. 1852–57.

[5] A. Boyette and S. Saadate, "Permanent power generating wind turbine with doubly fed asynchronous generator and storage unit, modelling and simulation", In: Proceedings of *the power electronics and motion control conference*; 2006. P. 1552–56.

[6] Anca D. Hansen, "Generators and power electronics for wind turbines", In: *Wind power in power systems*, John Wiley & Sons Ltd; 2005.

[7] L. L. Lai, and T. F. Chan. Distributed generation, IEEE press, John Wiley & Sons Ltd; 2007.

[8] Y. Tan, L. Meegahapola, and K. M. Muttaqi, "A review of technical challenges in planning and operation of remote area power supply systems," *Renew. Sustain. Energy Rev.*, vol. 38, no. 0, pp. 876-889, 2014.

[9] J. Morren, S. W. H. de Haan, W. L. Kling, and J. A. Ferreira, "Wind turbines emulating inertia and supporting primary frequency control," *IEEE Trans. Power Syst.,* vol. 21, no. 1, pp. 433-434, 2006.

[10] J. M. Mauricio, A. Marano, A. Gomez-Exposito, and J. L. Martinez Ramos, "Frequency regulation contribution through variable-speed wind energy conversion systems," *IEEE Trans. Power Syst.*, vol. 24, no. 1, pp. 173-180, 2009.

[11] O. D. Mipoung, L. A. Lopes, and P. Pillay, "Frequency support from a fixed-pitch type-2 wind turbine in a diesel hybrid mini-grid," *IEEE Trans. Sustain. Energy*, vol. 5, no. 1, pp. 110-118, 2014.

[12] G. Ramtharan, J. B. Ekanayake, and N. Jenkins, "Frequency support from doubly fed induction generator wind turbines," *IET Renew. Power Gen.*, vol. 1, no. 1, pp. 3-9, 2007.

[13] N. R. Ullah, T. Thiringer, and D. Karlsson, "Temporary primary frequency control support by variable speed wind turbines: Potential and applications," *IEEE Trans. Power Syst.*, vol. 23, no. 2, pp. 601-612, 2008.

[14] Y. Tan & K. M. Muttaqi, "Enhanced Frequency Response Strategy for PMSG based Wind Energy Conversion System using Ultracapacitor in Remote Area Power Supply Systems," In: Proc. of the *IEEE Industry Applications Society Annual Meeting*, 2015, pp. 1-8.

[15] Y. Tan, L.Meeghapola & K. M. Muttaqi, "Suboptimal Power-Point-Tracking based Primary Frequency Response for DFIGs in Hybrid RAPS," *IEEE Trans. on Ener. Conv.,* vol. 31, pp. 93-105, 2016.

[16] Miguel Rodriguez, Gonzalo Abad, Izaskun Sarasola, Alex Gilabert, "Crowbar Control Algorithms for Doubly Fed Induction Generator During Voltage Dips," In: Proc. of the *Europian Conference on Power Electronics and Applications*, 2006

[17] Ling Peng, Bruno Francois, Yongdong Li, "Improved Crowbar Control Strategy of DFIG Based Wind Turbines for Grid Fault Ride-Through*",* In: Proc. of the *Applied Power Electronics Conference and Exposition*, 2009.

[18] A. M. Haidar, M. T. Hagh & K. M. Muttaqi, "Improving low voltage ride-through using super capacitor at the DC link of doubly-fed induction generator based wind turbine," In: proc. of the *50th International Universities Power Engineering Conference (UPEC)*, 2015, pp. 1-6

[19] M. Noroozi and S. Farhangi, "Voltage and frequency Stability for Control of Stand-alone DFIG-based Wind Turbine using Direct Voltage Control Method," In Proc. of the *14th International Conference on Environment and Electrical Engineering (EEEIC),* 2014, pp. 85-90.

[20] H. El-Helw and S. B. Tennakoon, "Vector Control of a Doubly Fed Induction Generator for Standalone Wind Energy Application", In Proc. of the *1st Seminar on Wind Power to the Grid – EPE Wind Energy Chapter*, 2008, pp 1-6, March 2008.

[21] M. R. Agha Kashkooli, Seyed M. Madani, Ramtin Sadeghi, "Improved Direct Torque Control of DFIG with Reduced Torque and Flux Ripples at Constant Switching Frequency", In: Proc. of the *Power Electronics and Drive Systems Technologies Conference (PEDSTC)*, 2016.

[22] R. Cardenas, and R. Pena, "Sensorless vector control of induction machines for variable speed wind energy applications," *IEEE Trans. Energy. Conv.,* vol. 19, no. 1, pp. 196-205, Mar. 2004.

[23] Swagat Pati, Swati Samantray, "Decoupled Control of Active and Reactive Power in A DFIG Based Wind Energy Conversion System with Conventional P-I Controllers", In Proc. of the *International Conference on Circuit, Power and Computing Technologies [ICCPCT]*, 2014

[24] Jiahu Guo, Xu Cai and Youming Gong, "Decoupled Control of Active and Reactive Power for a Grid-connected Doubly-fed Induction Generator", In Proc. of the *International Conference on Electric Utility Deregulation and Restructuring and Power Technologies*, 2008.

[25] T. Monai, I. Takano, H. Nishikawa, and Y. Sawada, "A collaborative operation method between new energy-type dispersed power supply and EDLC," *IEEE Trans. Energy Convers.*, vol. 19, no. 3, pp. 590–598, Sep. 2004.

[26] T. Kinjo, T. Senjyu, N. Urasaki, and H. Fujita, "Output levelling of renewable energy by electric double-layer capacitor applied for energy storage system," *IEEE Trans. Energy Convers*., vol. 21, no. 1, pp. 221–227, Mar. 2006.

[27] N. Kakimoto, H. Satoh, S. Takayama, and K. Nakamura, "Ramp-Rate control of photovoltaic generator with electric double-layer capacitor," *IEEE Trans. Energy Convers*., vol. 24, no. 2, pp. 465–473, Jun. 2009.

[28] M. J. E. Alam, K. M. Muttaqi, D. Sutanto, "A Novel Approach for Ramp-Rate Control of Solar PV Using Energy Storage to Mitigate Output Fluctuations Caused by Cloud Passing", *IEEE Trans. On Energy Conv.,* Vol. 29, No. 2, June 2014, pp. 507-518

[29] P. Mitra, L. Zhang, L. Harnefors, "Offshore Wind Integration to a Weak Grid by VSC-HVDC Links Using Power-Synchronization Control: A Case Study*," IEEE Trans. on Power Delivery*, Vol. 29, No. 1, February 2014, pp. 453-461.

[30] The MathWorks, "MATLAB SIMULINK SimPower Block Help", Incorporating SIMULINK Version 7.1, SimPower Version 4.6, USA: The MathWorks, January 2008

[31] G. Yuan, J. Chai and Y. Li, "Vector Control and Synchronisation of Doubly Fed Induction Wind Generator System", In proc. of the *The 4th International Power Electronics and Motion Control Conference, (IPEMC 2004),* vol. 2, pp. 886-890, August 2004.

[32] S. Z. Chen, N. Cheung, K. C. Wong, J. Wu," Grid Synchronization of Doubly-fed Induction Generator Using Integral Variable Structure Control," *IEEE Trans. Energy Convers.,* Vol. 24, No. 4, December 2009, pp. 875-883.

[33] G. Tapia, G. Santamaria, M. Telleria "Methodology for Smooth Connection of Doubly Fed Induction Generators to the Grid," *IEEE Trans. Energy Convers.*, Vol. 24, No. 4, December 2009, pp. 959-971

[34] S. Z. Chen, N. C. Cheung,Y. Z., M. Zhang, X. M. Tang, "Improved Grid Synchronization Control of Doubly Fed Induction Generator Under Unbalanced Grid Voltage," *IEEE Trans. Energy Convers.,* Vol. 26, No. 3, September 2011, pp. 799-810.

[35] K. M. Muttaqi, M.T. Hagh, "Enhanced Frequency Response Strategy for PMSG based Wind Energy Conversion System using Ultracapacitor in Remote Area Power Supply Systems," In Proc. of the *Industry Applications Society Annual Meeting*, 2017 IEEE, 2017

[36] M. Aktarujjaman, K. A. Kashem, M. Negnevitsky & G. Ledwich, "Black start with DFIG based distributed generation after major emergencies," In proc. of the *IEEE International Conference on Power Electronics, Drives and Energy Systems (PEDES 2006)*, 2006, pp. 1-6.

[37] T. Lei, M. Barnes, and A. C. Smith, "Thermal cycling evaluation for DFIG wind turbine power converter based on joint modelling," in Proc. *Energy Conversion Congress and Exposition (ECCE)*, 2013, pp. 3845-3851.

[38] D. Zhou, F. Blaabjerg, M. Lau, and M. Tonnes, "Thermal cycling overview of multi-megawatt two-level wind power converter at full grid code operation," *IEEE trans. Ind. Appl.,* vol. 2, no. 4, pp. 173-182, 2013

[39] M. Z. Sujod, I. Erlich, and S. Engelhardt, "Improving the reactive power capability of the DFIG -based wind turbine during operation around the synchronous speed," *IEEE Trans. Energy Convers.*, vol. 28, no. 3, pp. 736-745, 2013

[40] M. Z. Sujod and I. Erlich, "Reactive power capability of DFIG based wind turbine around synchronous operating point with two-level and three-level npc converter," in Proc. of the *PowerTech (POWERTECH)*, 2013, pp. 1-6

[41] M. Bartram, J. v. Bloh, and R. W. D. Doncker, "Doubly-fed-machines in wind-turbine systems: Is this application limiting the lifetime of igbt frequency-converters,'" in Proc. of the *IEEE 35th Annual Power Electronics Specialists Conference*, 2004, pp. 2583-2587.

[42] L. Wei, J. McGuire, and R. A. Lukaszewski, "Analysis of PWM frequency control to improve the lifetime of PWM inverter," *IEEE Trans. Ind. Appl.,* vol. 47, no. 2, pp. 922-929, 2011

[43] T. Lei, M. Barnes, S. Smith, H. Sung-ho, A. Stock, and W. E. Leithead, "Using improved power electronics modeling and turbine control to improve wind turbine reliability," *IEEE Trans. Energy Convers.,* vol. 30, no. 3, pp. 1043-1051, 2015

[44] D. Xiang, C. Wang and Y. Liu, "Switching Frequency Dynamic Control for DFIG Wind Turbine Performance Improvement Around Synchronous Speed," *IEEE Trans. Power Electron.*, vol. 32, no. 9, pp. 7271-7283, Sept. 2017.

[45] Y. Tan, K. M. Muttaqi, L. Meegahapola & P. Ciufo, "Deadband control of doubly-fed induction generator around synchronous speed," *IEEE Trans. on Energy Convers.*, vol. 31, (4) pp. 1610-1621, 2016

[46] D. C. Lee, K. J. Lee, J. K. Seok, and J. W. Choi, "Online capacitance estimation of dc-link electrolytic capacitors for three-phase ac-dc-ac PWM converters using recursive least squares method," In Proc. *IEEE Electr. Power Appl.*, vol. 152, no. 6, pp. 1503–1508, Nov. 2005.

[47] K. Lee, T. Jahns, G. Venkataramanan, and W. Berkopec, "DC-bus electrolytic capacitor stress in adjustable-speed drives under input voltage unbalance and sag conditions," *IEEE Trans. Ind. Appl.*, vol. 43, no. 2, pp. 495–504, Mar./Apr. 2007.

[48] A. Amaral and A. Cardoso, "An economic offline technique for estimating the equivalent circuit of aluminum electrolytic capacitors," *IEEE Trans. Instrum. Meas.,* vol. 57, no. 12, pp. 2697–2710, Dec. 2008.

[49] K. W. Lee, M. Kim, J. Yoon, S. B. Lee, and J. Y. Yoo, "Condition monitoring of dc-link electrolytic capacitors in adjustable-speed drives," *IEEE Trans. Ind. Appl.,* vol. 44, no. 5, pp. 1606–1613, Sep./Oct. 2008.

[50] K. Tsang and W. Chan, "Low-cost sensing of equivalent series resistance for electrolytic capacitors," *IET Power Electron.,* vol. 2, no. 5, pp. 555– 562, Sep. 2009.

[51] A. Amaral and A. Cardoso, "A simple offline technique for evaluating the condition of aluminum-electrolytic-capacitors," *IEEE Trans. Ind. Electron.*, vol. 56, no. 8, pp. 3230–3237, Aug. 2009.

[52] B.-G. Gu and K. Nam, "A DC-link capacitor minimization method through direct capacitor current control," *IEEE Trans. Ind. Appl.*, vol. 42, no. 2, pp. 573–581, Mar./Apr. 2006.

[53] R. Maheshwari, S. Munk-Nielsen, and K. Lu, "An active damping technique for small DC-Link capacitor based drive system," *IEEE Trans. Ind. Informat*., vol. 9, no. 2, pp. 848–858, May 2013.

[54] J. Jung, S. Lim, and K. Nam, "A feedback linearizing control scheme for a PWM converter-inverter having a very small DC-link capacitor," *IEEE Trans. Ind. Appl*., vol. 35, no. 5, pp. 1124–1131, Sep./Oct.1999.

[55] H.-S. Jung, S.-J. Chee, S.-K. Sul, Y.-J. Park, H.-S. Park, and W.-K. Kim, "Control of three-phase inverter for AC motor drive with small DC-link capacitor fed by single-phase AC source," *IEEE Trans. Ind. Appl.*, vol. 50, no. 2, pp. 1074–1081, Mar./Apr. 2014.

[56] L. Shen, S. Bozhko, C. I. Hill and P. Wheeler, "DC-Link Capacitor Second Carrier Band Switching Harmonic Current Reduction in Two-Level Back-to-Back Converters," *IEEE Trans. on Power Electron.*, vol. 33, no. 4, pp. 3567-3574, April 2018.

[57] T. D. Nguyen, N. Patin, and G. Friedrich, "Extended double carrier PWM strategy dedicated to RMS current reduction in DC link capacitors of three phase inverters," *IEEE Trans. Power Electron.,* vol. 29, no. 1, pp. 396–406, Jan. 2014

[58] G.-J. Su and L. Tang, "A segmented traction drive system with a small dc bus capacitor," in Proc. of the *IEEE Energy Convers. Congr. Expo.,* Sep. 15–20, 2012, pp. 2847–2853.

[59] M. Gasperi, "Life prediction modeling of bus capacitors in ac variable frequency drives," *IEEE Trans. Ind. Appl.,* vol. 41, no. 6, pp. 1430–1435, Nov./Dec. 2005.

[60] K. Tsang and W. Chan, "Low-cost sensing of equivalent series resistance for electrolytic capacitors," *IET Power Electron*., vol. 2, no. 5, pp. 555–562, Sep. 2009.

[61] K. Zhao, P. Ciufo and S. Perera, "Rectifier Capacitor Filter Stress Analysis When Subject to Regular Voltage Fluctuations," *IEEE Trans.s Power Electron.*, vol. 28, no. 7, pp. 3627-3635, July 2013.

[62] Y. M. Chen, H. C. Wu, M. W. Chou, and K. Y. Lee, "Online failure prediction of the electrolytic capacitor for LC filter of switching-mode power converters," *IEEE Trans. Ind. Electron.,* vol. 55, no. 1, pp. 400–406, Jan. 2008

[63] A. Amaral and A. Cardoso, "On-line fault detection of aluminium electrolytic capacitors, in step-down dc-dc converters, using input current and output voltage ripple," *IET Power Electron.,* vol. 5, no. 3, pp. 315–322, Mar. 2012

[64] Lin, J., Keogh, E., Lonardi, S. & Chiu, B. (2003) "A Symbolic Representation of Time Series, with Implications for Streaming Algorithms". In proc. of the *8th ACM SIGMOD Workshop on Research Issues in Data Mining and Knowledge Discovery*, San Diego, CA. June 13

[65] E. Keogh, J. Lin and A. Fu (2005), "HOT SAX: Efficiently Finding the Most Unusual Time Series Subsequence," In Proc. of the *5th IEEE International Conference on Data Mining (ICDM 2005),* pp. 226 - 233., Houston, Texas, Nov 27-30, 2005

[66] J. E. Alam, K. M. Muttaqi & D. Sutanto, "A SAX-based advanced computational tool for assessment of clustered rooftop solar PV impacts on LV and MV networks in smart grid," *IEEE Trans. Smart Grid,* vol. 4, (1) pp. 577-585, 2013.

[67] M. J. E. Alam, K. M. Muttaqi and D. Sutanto, "A Novel Approach for Ramp-Rate Control of Solar PV Using Energy Storage to Mitigate Output Fluctuations Caused by Cloud Passing," *IEEE Trans. Energy Convers.,* vol. 29, no. 2, pp. 507-518, June 2014.

[68] Y. Tan, L. Meegahapola, and K. M. Muttaqi, "A review of technical challenges in planning and operation of remote area power supply systems," *Renew. Sustain. Energy Rev.*, vol. 38, no. 0, pp. 876–889, Oct. 2014.

[69] M. E. Haque, M. Negnevitsky, and K. M. Muttaqi, "A novel control strategy for a variable-sped wind turbine with a permanent-magnet synchronous generator," *IEEE Trans. Ind. Appl.*, vol. 46, no. 1, pp. 331–339, Feb. 2010.

[70] A. Mullane and M. O'Malley, "The inertial response of induction machine-based wind turbines," *IEEE Trans. Power Syst.*, vol. 20, no. 3, pp. 1496–1503, Aug. 2005.

[71] C.-C. Le-Ren, L. Wei-Ting, and Y. Yao-Ching, "Enhancing frequency response control by DFIGs in the high wind penetrated power systems," *IEEE Trans. Power Syst.*, vol. 26, no. 2, pp. 710–718, May 2011.

[72] Z. Deng et al., "A high-temperature superconducting maglev ring test line developed in chengdu, China," *IEEE Trans. Appl. Supercond.*, vol. 26, no. 6, p. 3602408, Sept. 2016

[73] Z. Deng et al., "Performance advances of HTS maglev vehicle system in three essential aspects," *IEEE Trans. Appl. Supercond.*, vol. 19, no. 3, pp. 2137–2141, Jun. 2009.

[74] M. E. Elshiekh, D. E. A. Mansour, and A. M. Azmy, "Improving fault ride-through capability of DFIG-based wind turbine using superconducting fault current limiter," *IEEE Trans. Appl. Supercond.*, vol. 23, no. 3, p. 5601204, Jun. 2013.

[75] W. Guo, L. Xiao and S. Dai, "Enhancing low-voltage ride-through capability and smoothing output power of DFIG with a superconducting fault-current limiter–magnetic energy storage system," *IEEE Trans. Ener. Conv.*, vol. 27, no. 2, pp. 277–295, Jun. 2012.

[76] M. Farhadi and O. Mohammed, "Energy storage technologies for high-power applications," *IEEE Trans. Ind. App.*, vol. 52, no. 3, pp. 1953-1961, May–Jun. 2016.

[77] S. Pasko et al., "Comparison of SMES and ScES based power conditioning systems," in Proc. of the *European Conf. Power Electron. Appl.,* 11–14 Sept. 2005, Dresden, Germany, pp. 1–10.

[78] J. X. Jian and X. Y. Chen, "Study on the SMES application solutions for smart grid," *Physics Procedia*. vol. 36. pp. 902–907, 2012.

[79] X. Zhou, X. Y. Chen, and J. X. Jin, "Development of SMES technology and its applications in power grid," in Proc. *2011 Int. Conf. Appl. Supercond. Electromag. Dev.*, 14–16 Dec. 2011, NSW, Australia, pp. 260–269.

[80] Yi. Wang, J. Meng, X. Zhang, and Lie Xu, "Control of PMSG-based wind turbines for system inertial response and power oscillation damping," *IEEE Trans. Sustain. Energy,* vol. 6, no. 2, pp. 565–574, Apr. 2015.

[81] M. R. Islam, Y. G. Guo, and J. G. Zhu, "Power converters for wind turbines: current and future development," in: *Materials and Processes for Energy: Communicating Current Research and Technological Developments,* A. Mendez-Vilas, Ed., pp. 559–571, Aug. 2013

[82] J. F. Conroy and R. Watson, "Frequency response capability of full converter wind turbine generators in comparison to conventional generation," *IEEE Trans. Power Syst.*, vol. 23, no. 2, pp. 649–656, May 2008.

[83] A. Wintrich, U. Nicolai, W. Tursky, and T. Reimann, "*Application manual power semiconductors*," S. I. GmbH, Ed., 2nd ed. Nuremberg, Germany: ISLE Verlag, 2015.

[84] Calculating power losses in an IGBT module [Online]. Available: https://www.dynexsemi.com/assets/downloads/DNX_AN6156.pdf.

[85] SEMIKRON. SKiiP 2013 GB172-4DW V3 [Online]. Available: https://www.semikron.com/products/product-classes/ipm/detail/skiip2013-gb172-4dw-v3-20451248.html

[86] S. Engelhardt, I. Erlich, C. Feltes, J. Kretschmann, and F. Shewarega, "Reactive Power Capability of Wind Turbines Based on Doubly Fed Induction Generators", *IEEE Trans. on Energy Convers.*, vol. 26, (1) pp. 364-372, 2011.

[87] L. Wei, J. McGuire, and R. Lukaszewski, "Analysis of PWM frequency control to improve the lifetime of PWM inverter," *IEEE Trans. Ind. Appl.*, vol. 47, no. 2, pp. 922–929, Mar./Apr. 2011.

[88] D. Murdock, J. Torres, J. Connors, and R. Lorenz, "Active thermal control of power electronic modules," *IEEE Trans. Ind. Appl.*, vol. 42, no. 2, pp. 552–558, Mar./Apr. 2006.

[89] L. Wei, R. J. Kerkman, R. A. Lukaszewski, H. Lu and Z. Yuan, "Analysis of IGBT power cycling capabilities used in doubly fed induction generator wind power system," in *IEEE Trans. Ind. Appl.*, vol. 47, no. 4, pp. 1794-1801, July-Aug. 2011.

[90] A. Bryant, P. Mawby, P. Palmer, E. Santi, and J. Hudgins, "Exploration of power device reliability using compact device models and fast electrothermal simulation," *IEEE Trans. Ind. Appl.*, vol. 44, no. 3, pp. 894–903, May/Jun. 2008.

[91] P. Ghimire, A. R. de Vega, S. Beczkowski, B. Rannestad, S. Munk-Nielsen, and P. Thogersen, "Improving power converter reliability: Online monitoring of high-power IGBT modules," *IEEE Trans. Ind. Electron*. Mag., vol. 8, no. 3, pp. 40–50, Sep. 2014

[92] D. Zhou, F. Blaabjerg, T. Franke, M. Tønnes, and M. Lau, "Comparison of wind power converter reliability with low-speed and medium-speed permanent-magnet synchronous generators," *IEEE Trans. Ind. Electron.*, vol. 62, no. 10, pp. 6575–6584, Oct. 2014

[93] D. C. Lee, K. J. Lee, J. K. Seok, and J. W. Choi, "Online capacitance estimation of dc-link electrolytic capacitors for three-phase ac-dc-ac PWM converters using recursive least squares method*," IEE Proc.—Electr. Power Appl*., vol. 152, no. 6, pp. 1503–1508, Nov. 2005.

[94] L. A. Cleary-Balderas and A. Medina-Rios, "Selective harmonic current mitigation with a Shunt Active Power Filter," In: Proc. of the *2012 North American Power Symposium (NAPS), Champaign*, IL, 2012, pp. 1-5.

[95] Y. M. Chen, H. C. Wu, M. W. Chou, and K. Y. Lee, "Online failure prediction of the electrolytic capacitor for LC filter of switching-mode power converters," *IEEE Trans. Ind. Electron.*, vol. 55, no. 1, pp. 400–406, Jan. 2008

[96] T. Lei, M. Barnes, S. Smith, H. Sung-ho, A. Stock, and W. E. Leithead, "Using improved power electronics modeling and turbine control to improve wind turbine reliability," *IEEE Trans. Energy Convers*., vol. 30, no. 3, pp. 1043-1051, 2015.

[97] B. P. McGrath and D. G. Holmes, "A general analytical method for calculating inverter DC-link current harmonics," *IEEE Trans. Ind. Appl.*, vol. 45, no. 5, pp. 1851–1859, Sep./Oct. 2009

[98] L. Shen, S. Bozhko, C. I. Hill and P. Wheeler, "DC-Link Capacitor Second Carrier Band Switching Harmonic Current Reduction in Two-Level Back-to-Back Converters," in *IEEE Transactions on Power Electronics*, vol. 33, no. 4, pp. 3567-3574, April 2018.

[99] Vishay Siliconix IRF840LC data sheet [online], available: https://www.vishay.com/docs/91067/91067.pdf

[100] https://www.aemo.com.au/media/Files/Electricity/NEM/Security_and_Reliability/Reports/2016/FPSS---International-Review-of-Frequency-Control.pdf

[101] http://www.soni.ltd.uk/media/documents/Operations/June%202017%20RoCoF%20Report.pdf

[102] https://www.utas.edu.au/__data/assets/pdf_file/0008/778607/IPS-Connect-2015-Chris-Smith.pdf